



University of Pennsylvania  
**ScholarlyCommons**

---

Publicly Accessible Penn Dissertations


---

2022

## Simons Observatory Large Aperture Telescope Receiver

Ningfeng Zhu  
*University of Pennsylvania*

Follow this and additional works at: <https://repository.upenn.edu/edissertations>

 Part of the [Astrophysics and Astronomy Commons](#)

---

### Recommended Citation

Zhu, Ningfeng, "Simons Observatory Large Aperture Telescope Receiver" (2022). *Publicly Accessible Penn Dissertations*. 5581.

<https://repository.upenn.edu/edissertations/5581>

This paper is posted at ScholarlyCommons. <https://repository.upenn.edu/edissertations/5581>  
For more information, please contact [repository@pobox.upenn.edu](mailto:repository@pobox.upenn.edu).

---

# Simons Observatory Large Aperture Telescope Receiver

## Abstract

In the past three decades, cosmic microwave background (CMB) has provided a wealth of information on the origin and the history of the universe. From motivating the theory of the Big Bang, to providing tests for the standard model of cosmology; from measuring the Hubble constant, to constraining the mass of the neutrino; from testing the matter composition of the universe, to shedding light on the cluster evolution, CMB has truly become one of the most critical subjects of modern cosmology. However, to fully realize its potential and to achieve a level of accuracy that none has achieved before, large observatories equipped with ten times the detectors as the current generation experiments are needed. Such is the time that Simons Observatory (SO) collaboration came together, and proposed a Large Aperture Telescope (LAT) and an array of Small Aperture Telescopes (SATs) that met such criteria. Built upon the expertise from the current generation ground-based telescopes such as the Atacama Cosmology Telescope (ACT) and the South Pole Telescope (SPT), SO will initially deploy a total of 60,000 detectors, split about evenly between the LAT and SATs, with the potential to double the detector count in the LAT. Naturally, it is no easy undertaking to build a receiver capable of such feat for the LAT. In this thesis, I will recount the science cases put forth by SO, and walk through our journey in the designing, making, and testing of the Large Aperture Telescope Receiver (LATR).

## Degree Type

Dissertation

## Degree Name

Doctor of Philosophy (PhD)

## Graduate Group

Physics & Astronomy

## First Advisor

Mark Devlin

## Keywords

CMB, Cryogenic Instrument, Ground-based Telescope

## Subject Categories

Astrophysics and Astronomy

# **Simons Observatory Large Aperture Telescope Receiver**

Ningfeng Zhu

A DISSERTATION

in

Physics and Astronomy

Presented to the Faculties of the University of Pennsylvania

in Partial Fulfillment of the Requirements for the degree of Doctor of Philosophy

2022

## **Supervisor of Dissertation**

---

Mark J. Devlin, Reese W. Flower Professor of Astronomy and Astrophysics

## **Graduate Group Chairperson**

---

Ravi K. Sheth, Professor of Physics and Astronomy

## **Dissertation Committee:**

Robert Thornton, Professor of Physics

James Aguirre, Associate Professor of Physics and Astronomy

Cullen Blake, Associate Professor of Physics and Astronomy

Christopher Mauger, Associate Professor of Physics

# Acknowledgements

I have always been fascinated by the subject of history. One person can only experience so much within one's limited life time, yet by reading history, they can expand their horizon by exploring the past and living through moments that spanned hundreds and thousands of years. For the same reason, I am even more captivated when I encountered the subject of cosmology. Historians study the past few thousand years, yet cosmologists are set out to study the past 13.8 billion years, tracing the root all the way back to the origin of the universe. Comparing to the history of universe, any individual life, society and nation, or even the entire human existence appear so minuscule. Consequently, studying cosmology has been a truly humbling experience, and it is such an honor to be able to work with world-class experts throughout the journey of studying this grand subject.

I cannot get to where I am today without my advisor Mark Devlin at University of Pennsylvania, to whom I am deeply grateful for. He holds his students to high standards, and can often appear quite demanding, but at the same time, he always try to make himself available to advise and to lead no matter how busy he is. He is a person that leads with actions, not just with words, and would attack problems relentlessly until they are solved. Throughout the past five years, I have come to appreciate the family of sort he sets up in the lab, where he sincerely wishes every one of his students to grow, to excel, and to succeed in work and in life. I feel privileged to be his student, to help with the Atacama Cosmology Telescope, and to be entrusted to lead the design of Simons Observatory Large Aperture Telescope Receiver, a truly once-in-a-lifetime project. The lab will not be complete without Robert Thornton, Jeffrey Klein, Simon Dicker, Michele Limon, Federico Nati, Elio

Angile, Nicholas Galitzki, Marius Lungu, Nate Lourie, Zhilei Xu, Gabriele Coppi, Ian Lowe, Jeffrey Iuliano, John Orłowski-Scherer, Anna Kofman, Tanay Bhandarkar, Karen Perez Sarmiento, Saianeesh Haridas, Harold Borders, Jeff Hancock, Brooke DiGia, Alexander Manduca, and many others that have provided kind and generous assistance on various projects and helped shape who I am as a research scientist. Thank you truly for your companionship along the journey.

Thinking back to my life as an undergraduate student at University of Chicago, I want to thank John Carlstrom, Stephan Meyer, and Bradford Benson for introducing me to the world of observational cosmology by allowing me to work on the South Pole Telescope. They, together with Lindsey Bleem, Ritoban Basu Thakur, Zhaodi Pan, Tyler Natoli, Daniel Dutcher, Joshua Sobrin and Amy Tang have provided ample guidance and support when I felt lost in lab or in life. Without them, I would not be able to make it to the graduate school in the first place.

Finally, I wish to thank my family, my grandparents who constantly encourage me to step out of my comfort zone and take on new adventures, and my parents who inspired my curiosity in science and always firmly stood behind me no matter the direction I chose to take on. I would like to especially thank my wife Siwei:

*Ever since we met in 2008,  
you have always stood by me, rain or shine.  
You lit my path during my darkest time,  
and made even the valley of my life sublime.  
No matter how small or inconsequential we are in this spacetime,  
whenever I hold your hand,  
I know I am not alone,  
and I feel so fortunate that our waveforms are intertwined.*

# ABSTRACT

Simons Observatory Large Aperture Telescope Receiver

Ningfeng Zhu

Mark J. Devlin

In the past three decades, cosmic microwave background (CMB) has provided a wealth of information on the origin and the history of the universe. From motivating the theory of the Big Bang, to providing tests for the standard model of cosmology; from measuring the Hubble constant, to constraining the mass of the neutrino; from testing the matter composition of the universe, to shedding light on the cluster evolution, CMB has truly become one of the most critical subjects of modern cosmology. However, to fully realize its potential and to achieve a level of accuracy that none has achieved before, large observatories equipped with ten times the detectors as the current generation experiments are needed. Such is the time that Simons Observatory (SO) collaboration came together, and proposed a Large Aperture Telescope (LAT) and an array of Small Aperture Telescopes (SATs) that met such criteria. Built upon the expertise from the current generation ground-based telescopes such as the Atacama Cosmology Telescope (ACT) and the South Pole Telescope (SPT), SO will initially deploy a total of 60,000 detectors, split about evenly between the LAT and SATs, with the potential to double the detector count in the LAT. Naturally, it is no easy undertaking to build a receiver capable of such feat for the LAT. In this thesis, I will recount the science cases put forth by SO, and walk through our journey in the designing, making, and testing of the Large Aperture Telescope Receiver (LATR).

# Contents

<b>Acknowledgements</b>	<b>ii</b>
<b>Abstract</b>	<b>iv</b>
<b>List of Tables</b>	<b>vii</b>
<b>List of Figures</b>	<b>viii</b>
<b>1 The Ever Expanding Universe</b>	<b>1</b>
1.1 The Making of the CMB . . . . .	1
1.1.1 The Metric of the Universe . . . . .	4
1.1.2 The Scattering Particles . . . . .	10
1.1.3 Big Bang Nucleosynthesis . . . . .	16
1.1.4 The Epoch of Recombination . . . . .	19
1.2 Decoding the CMB . . . . .	20
1.2.1 The Theory of Inflation . . . . .	21
1.2.2 Anisotropies in the CMB . . . . .	23
1.3 Next Generation CMB Observation . . . . .	28
1.3.1 Progress Made So Far . . . . .	28
1.3.2 SO Science Goals . . . . .	30
<b>2 SO LATR Design</b>	<b>34</b>
2.1 SO LATR Design and Operation Guideline . . . . .	34
2.1.1 Detector Count and Operating Temperature . . . . .	34
2.1.2 Scanning Strategy . . . . .	37
2.2 LATR Mechanical Design . . . . .	39
2.2.1 LATR G-10 Tab Design . . . . .	42
2.2.2 300 K Stage (Vacuum Shell) . . . . .	44
2.2.3 80 K Stage . . . . .	47
2.2.4 40 K Stage . . . . .	49
2.2.5 4 K Stage . . . . .	51

2.2.6	Optics Tubes . . . . .	53
2.2.7	1K and 100mK Stages . . . . .	60
2.3	LATR Cryogenic Design . . . . .	63
2.3.1	Cryo-cooler Integration . . . . .	63
2.3.2	Thermal Modeling . . . . .	67
2.3.3	Cooldown Calculation and Heat Switches . . . . .	73
2.4	Readout Interface Design . . . . .	77
2.4.1	Cold Detector Readout Interface . . . . .	78
2.4.2	Warm Detector Readout Interface . . . . .	81
2.4.3	Housekeeping Readout Interface . . . . .	82
2.5	Telescope Interface Design . . . . .	84
2.5.1	LATR Co-rotator . . . . .	84
2.5.2	LATR Lifter . . . . .	86
<b>3</b>	<b>SO LATR Validation Testing</b>	<b>88</b>
3.1	Mechanical Test . . . . .	89
3.1.1	Cryostat Mechanical Validation . . . . .	89
3.1.2	Optics Tube Mechanical Validation . . . . .	93
3.2	Cryogenic Test . . . . .	95
3.2.1	Cooler Calibration . . . . .	95
3.2.2	Cooldown and Pump Down Time . . . . .	98
3.2.3	Cryogenic Performance Validation . . . . .	101
<b>4</b>	<b>Future Work</b>	<b>113</b>
4.1	LATR Potential Upgrade . . . . .	113
4.1.1	Additional Cooling Power Consideration . . . . .	113
4.1.2	Additional Thermal Strap Consideration . . . . .	115
<b>5</b>	<b>Conclusion</b>	<b>117</b>
	<b>Appendix A: List of Acronyms</b>	<b>119</b>
	<b>Bibliography</b>	<b>122</b>



# List of Tables

1.1	Simons Observatory Key Science goals . . . . .	31
2.1	The SO LAT Survey Specifications . . . . .	37
2.2	G10 Tab Specifications . . . . .	43
2.3	LATR Thermal Loading Estimates . . . . .	69
2.4	Optical Thermal Loading Table . . . . .	70
2.5	Filter Stack Table . . . . .	71
3.1	LATR Front Plate Metrology Results - Under Vacuum . . . . .	89
3.2	LATR 4K Plate Metrology Results . . . . .	92
3.3	Example of LATR Optics Tube Metrology Results . . . . .	95
3.4	LATR Cooldown Time . . . . .	100
3.5	80 K Stage Thermal Performance . . . . .	103
3.6	40 K/4 K Stage Thermal Performance . . . . .	105

# List of Figures

1.1	Temperature of the Universe . . . . .	2
1.2	Brief History of the Universe . . . . .	3
1.3	Temperature Anisotropy Measured by Planck . . . . .	27
1.4	CMB Measurement Thus Far . . . . .	30
2.1	LATR in the LAT . . . . .	35
2.2	LATR External View . . . . .	39
2.3	LATR Cut-out View . . . . .	40
2.4	G-10 Tab Example . . . . .	43
2.5	300 K Shell Exploded View . . . . .	44
2.6	LATR Front Plate FEA Result . . . . .	46
2.7	LATR 80 K Stage Exploded View . . . . .	47
2.8	LATR 80 K Stage Picture . . . . .	48
2.9	LATR 40 K Stage Exploded View . . . . .	49
2.10	LATR 40 K Stage Picture . . . . .	50
2.11	LATR 4 K Stage Exploded View . . . . .	51
2.12	LATR 4 K Stage Picture . . . . .	52
2.13	Optics Tube Cutaway Rendering . . . . .	53
2.14	Optics Tube Readout Components . . . . .	58
2.15	Thermal BUS Exploded View Rendering . . . . .	60
2.16	Thermal BUS Installed Picture . . . . .	61
2.17	40 K Stage Modification . . . . .	65
2.18	40 K Strap . . . . .	66
2.19	LATR Optics Tube Geometry . . . . .	70
2.20	80K Stage Thermal Simulation . . . . .	73
2.21	LATR Cool Down Simulation . . . . .	74
2.22	DR Heat Pipe . . . . .	76
2.23	LATR Heat Switch . . . . .	77
2.24	LATR URH Picture . . . . .	78
2.25	4K Cavity and Coaxial Cables . . . . .	79
2.26	Cryocard Crate Rendering . . . . .	81

2.27	LATR Thermometry Plan . . . . .	82
2.28	Single Thermometer Picture . . . . .	84
2.29	LATR Co-rotator . . . . .	85
2.30	LATR Lifter . . . . .	87
3.1	FARO Measurement in Progress . . . . .	90
3.2	Dummy Optics Tubes Installed . . . . .	93
3.3	Pulse Tube 1 Capacity Map . . . . .	96
3.4	Pulse Tube 2 Capacity Map . . . . .	97
3.5	Cooldown Curves . . . . .	99
3.6	80 K Filter Installation . . . . .	102
3.7	Seven Optics Tube Installed . . . . .	110
3.8	Temperature Stability Overnight . . . . .	111
4.1	LATR PT Upgrade . . . . .	114

# Chapter 1

## The Ever Expanding Universe

Much of the material covered in Chapter 1 is summarized from textbooks *Modern Cosmology* [24], *Introduction to Modern Cosmology* [51], and *Physical Foundations of Cosmology* [57], in combination with cutting-edge results from various research groups.

### 1.1 The Making of the CMB

13.7 billion years ago, our universe started out with a "bang", commonly known as the Big Bang. It is hard to deduce its exact state before the singularity came into existence, as the laws of physics may very well break down with its extremely high energy concentration. But we do have some theories about what comes after.

$10^{-32}$  seconds after the rapid inflation started, the universe had grown to over  $10^{25}$  times in size while rapidly cooling down. After  $10^{-12}$  seconds, the condition is still dense enough that elementary particles, including quarks, leptons, bosons, and their antimatter counterparts were kept in a dynamic thermal equilibrium without a stable

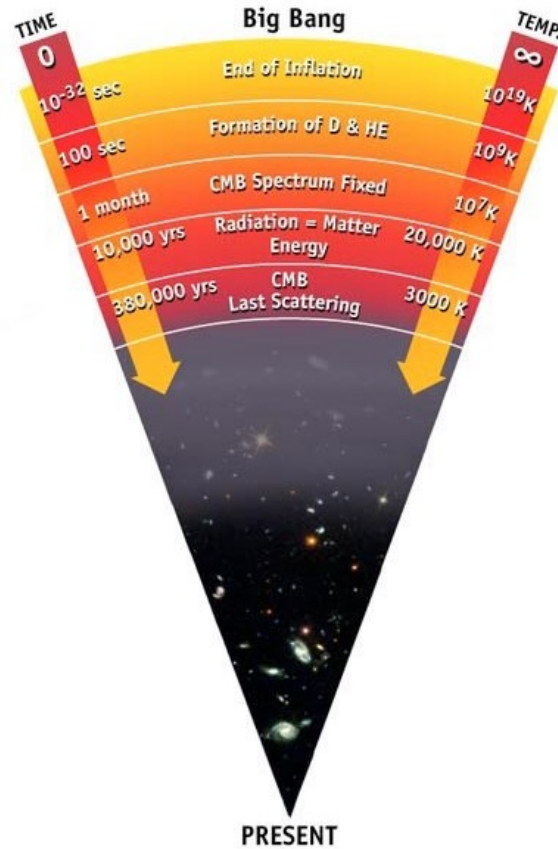


Figure 1.1: The temperature of the universe as it expands, and some significant milestones along the process. Figure credits: NASA.

form. The matter-antimatter pairs were spontaneously created from energy, and then immediately destroyed by annihilation. Within  $10^{-6}$  seconds, matter-antimatter annihilation slowed down significantly and the temperature is cool enough that quarks started to bind with each other by strong force. At the end of one second after the creation of the universe, universe has grown to a few light-years large. Seconds later, electrons started to freeze-out, and then atomic nuclei started to form as the universe cooled to below  $10^9$  K. The relation between the temperature of the universe and time is summarized in Figure 1.1 <sup>1</sup>.

<sup>1</sup>Figure is taken from: [https://wmap.gsfc.nasa.gov/universe/bb\\_tests\\_cmb.html](https://wmap.gsfc.nasa.gov/universe/bb_tests_cmb.html)

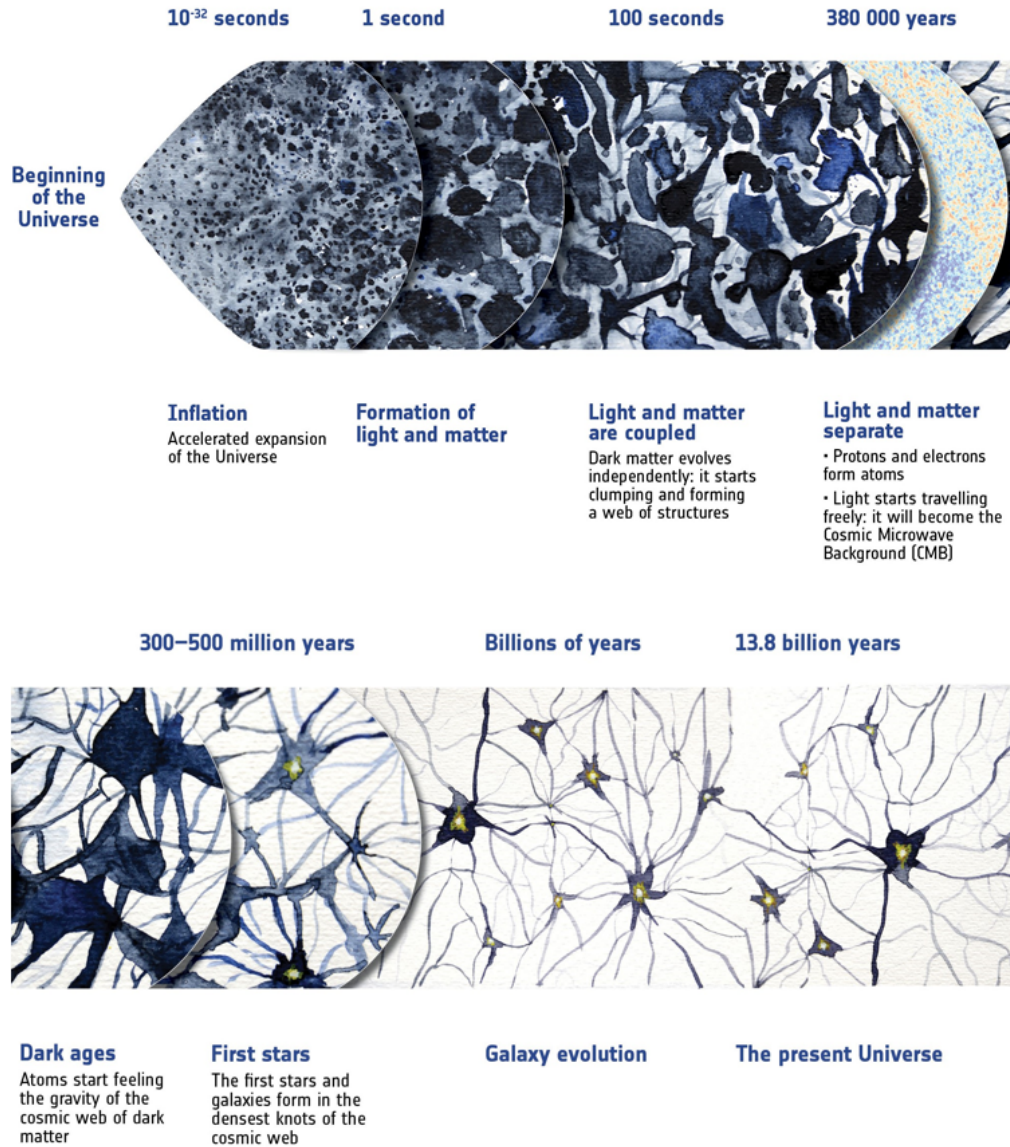


Figure 1.2: This figure shows the brief history of the universe as we know it today, including the beginning of the universe from a singularity, cosmic inflation that happened before  $t = 10^{-32}$  seconds, and the Recombination era at  $t = 380,000$  years. Figure credits: European Space Agency.

For the next 380,000 years, the universe continued to cool down while gradually expanding, as shown in Figure 1.2<sup>2</sup>. During this period, the universe is often portrayed as a dense "plasma soup", as the mean free path of the photon is very short due to

<sup>2</sup>Figure is taken from: <https://sci.esa.int/web/planck/-/55392-the-history-of-the-universe>

efficient Compton scattering. However, as the universe dropped below  $\sim 3,000$  K, free electrons started to rapidly bond with protons, forming hydrogen and helium while rendering the Compton scattering inefficient. This sets the photons free, allowing them to travel in a straight line, and leaving a permanent imprint in space with embedded message of where all the matter was in that short period. This imprint is the cosmic microwave background (CMB) that generations of scientists have been trying to study and decipher.

The process described above is not only aesthetically pleasing, but motivated by observation and backed by experimental results. Nevertheless, in order to fully appreciate these scientific evidence, one needs to start from the fundamentals. A good starting point is to look at the metrics that defined the "ruler" of the universe.

### 1.1.1 The Metric of the Universe

In the familiar three-dimensional space, a location can be defined by a three-component vector, written as  $(x, y, z)$  in Cartesian coordinates. In this case, a distance squared can be defined as the following summation

$$dl^2 = \sum_{i,j=1}^3 g_{ij} dx^i dx^j \quad (1.1)$$

where  $x^1 = x$ ,  $x^2 = y$ , and  $x^3 = z$ , and the metric  $g_{ij}$  is the identity matrix

$$g_{ij} = \begin{pmatrix} 1 & 0 & 0 \\ 0 & 1 & 0 \\ 0 & 0 & 1 \end{pmatrix} \quad (1.2)$$

In order to better capture the spacetime curvature, it is useful to include a fourth component, time, in the coordinates. In this case, the squared distance becomes

$$ds^2 = \sum_{\mu, \nu=0}^3 g_{\mu\nu} dx^\mu dx^\nu \quad (1.3)$$

where  $i$  and  $j$  are replaced by  $\mu$  and  $\nu$ , and the summation captures all four components. Now if we want to describe a universe that is expanding (to which there are numerous observational proofs) instead of standing still, the metrics needs to be modified to include a scale factor  $a(t)$ , which evolves with time. The metrics then becomes

$$g_{\mu\nu} = \begin{pmatrix} -1 & 0 & 0 & 0 \\ 0 & a^2(t) & 0 & 0 \\ 0 & 0 & a^2(t) & 0 \\ 0 & 0 & 0 & a^2(t) \end{pmatrix} \quad (1.4)$$

which is also known as the Friedmann-Lemaitre-Robertson-Walker (FLRW) metric.

Armed with the metric, we can now set out to find an alternative expression (based on FLRW metric) to Einstein's equation

$$G_{\mu\nu} + \Lambda g_{\mu\nu} = 8\pi G T_{\mu\nu} \quad (1.5)$$

where  $G_{\mu\nu}$  is the Einstein tensor defined as:

$$G_{\mu\nu} \equiv R_{\mu\nu} - \frac{1}{2} g_{\mu\nu} R \quad (1.6)$$

In the equations above,  $\Lambda$  is the cosmological constant,  $G$  is the Newton's constant,



$T_{\mu\nu}$  is the energy-momentum tensor,  $R_{\mu\nu}$  is the Ricci tensor, and  $R$  is the Ricci scalar. By looking at the components, we can see that the left hand side of Equation 1.5 describes the metrics of the universe, while its right hand side contains information about the energy of the content of the universe. The beauty of this equation is that it relates the two.

To make the Einstein's equation more explicit, it is useful to expand the Ricci tensor with Christoffel symbols

$$R_{\mu\nu} = \Gamma_{\mu\nu,\alpha}^{\alpha} - \Gamma_{\mu\alpha,\nu}^{\alpha} + \Gamma_{\beta\alpha}^{\alpha}\Gamma_{\mu\nu}^{\beta} - \Gamma_{\beta\nu}^{\alpha}\Gamma_{\mu\alpha}^{\beta} \quad (1.7)$$

where the partial derivatives are defined as

$$\Gamma_{\mu\nu,\alpha}^{\alpha} \equiv \frac{\partial \Gamma_{\mu\nu}^{\alpha}}{\partial x^{\alpha}} \quad (1.8)$$

Further, the Christoffel symbol itself can be written as

$$\Gamma_{\mu\nu}^{\alpha} = \frac{1}{2}g^{\alpha\beta}[g_{\mu\beta,\nu} + g_{\nu\beta,\mu} - g_{\mu\nu,\beta}] \quad (1.9)$$

where the partial derivatives is similarly defined as

$$g_{\mu\beta,\nu} = \frac{\partial g_{\mu\beta}}{\partial x^{\nu}} \quad (1.10)$$

This expression makes it apparent that the Ricci tensor is only dependent on the choice of metrics, and since we have chosen the FLRW metrics in Equation 1.4, we can explicitly solve for  $R_{\mu\nu}$ . As it turns out, all other components in the Ricci

tensor are zero for the FLRW metrics, except for the four diagonal components  $R_{00}$ ,  $R_{11}$ ,  $R_{22}$ , and  $R_{33}$ . It is therefore convenient to group the four resulting linear equations into time-time ( $R_{00}$ ) and space-space ( $R_{11}$ ,  $R_{22}$ , and  $R_{33}$ ) parts. Solving for time-time part yields

$$\left(\frac{\dot{a}}{a}\right)^2 = \frac{8\pi G}{3}\rho \quad (1.11)$$

and solving for the space-space part yields

$$\frac{\ddot{a}}{a} = -\frac{4\pi G}{3}[\rho + 3\mathcal{P}] \quad (1.12)$$

Here  $\rho$  is the energy density, and  $\mathcal{P}$  is the total pressure. Since we start off with the cosmological constant  $\Lambda$  included in Equation 1.5, the energy density here includes matter, radiation, and  $\rho_\Lambda$ , the dark energy. Equation 1.11 and Equation 1.12 combined are known as the Friedmann equations.

Recall that  $a(t)$  is the scale factor introduced in Equation 1.4, where it captures the ratio between comoving distance and physical distance, and how it evolves with time. To further study the relationship between scale factor and energy density, it is useful to introduce the definition of Hubble rate

$$H(t) \equiv \frac{\dot{a}}{a} \quad (1.13)$$

at the same time, we will define the Hubble constant as the Hubble rate of today

$$H_0 \equiv H(t_0) \quad (1.14)$$

where  $t_0$  is the current time. Taking  $H(t)$  into Equation 1.11, and dividing both sides by  $H_0$ , we arrive at

$$\frac{H^2(t)}{H_0^2} = \frac{\rho}{\frac{3H_0^2}{8\pi G}} \quad (1.15)$$

If we introduce another constant, the critical density today,

$$\rho_{cr} \equiv \frac{3H_0^2}{8\pi G} \quad (1.16)$$

as well as the density parameters,

$$\Omega_s \equiv \frac{\rho_s(t_0)}{\rho_{cr}} \quad (1.17)$$

where  $s$  represents the components of the universe, e.g. matter, radiation, or dark energy, then the energy density of component  $s$  can be written as

$$\frac{\rho_s(a)}{\rho_{cr}} = \Omega_s a^{-3(1+\omega_s)} \quad (1.18)$$

where  $\omega_s$  is the equation of state. Taking Equation 1.17 and Equation 1.18 into Equation 1.15, the first Friedmann equation now becomes

$$\frac{H^2(t)}{H_0^2} = \frac{\rho}{\rho_{cr}} = \sum_{s=r,m,\Lambda} \Omega_s [a(t)]^{-3(1+\omega_s)} \quad (1.19)$$

If we are dealing with a standard Euclidean universe, where  $\Omega_r + \Omega_m + \Omega_\Lambda = 1$ , then Equation 1.19 would be complete. Nevertheless, to include the possible curvature

of the universe in the equation, a fourth parameter is introduced as  $\Omega_\kappa$ , as

$$\Omega_\kappa = 1 - \Omega_r - \Omega_m - \Omega_\Lambda \equiv -\frac{\kappa}{H^2 a^2} \quad (1.20)$$

where  $\kappa$  is a curvature parameter.  $\Omega_\kappa$  is not a real "energy" term, but a form representing a potential difference between the sum of the energy densities and the critical density. Based on the most recent observation from Planck, the universe is very close to flat (or Euclidean), with  $\Omega_\kappa = 0.001 \pm 0.002$  [67]. Taking Equation 1.20 into Equation 1.19, the now completed equation reads

$$H^2(t) = H_0^2 \left\{ \sum_{s=r,m,\Lambda} \Omega_s [a(t)]^{-3(1+\omega_s)} + \Omega_\kappa [a(t)]^{-2} \right\} \quad (1.21)$$

But what is the  $\omega_s$  for each component? The easiest component to solve would be  $\Omega_\Lambda$ , where by definition, it is constant, and as a result does not evolve with time. Therefore we have  $\omega_\Lambda = -1$ .

For  $\Omega_m$ , it is calculated by the total rest mass of the matter times their number density. The number density inversely correlates with the volume of the universe, and the volume of the universe scales as  $a^3$ . Thus it is straightforward that  $\Omega_m$  would scale as  $a^{-3}$ , resulting in  $\omega_m = 0$ .

For  $\Omega_r$ , the wavelength  $\lambda$  of the radiation would scale as  $a$ . Since  $\lambda = c/f$ , the frequency  $f$  would scale as  $a^{-1}$ . Since the black-body radiation scales with the Temperature with  $T^4$ , and the black-body spectrum is dependent of  $f/T$ , we conclude that  $\Omega_r$  would scale as  $T^4 \propto a^{-4}$ , with  $\omega_r = 1/3$ .

With all the equation of state resolved, let us introduce another parameter,

cosmological redshift  $z$

$$z \equiv \frac{1}{a} - 1 \quad (1.22)$$

Replacing  $a$  with  $z$ , and including the derived equation of state, Equation 1.21 can be rewritten in an even more useful format:

$$H^2(t) = H_0^2[\Omega_\Lambda + \Omega_\kappa(1+z)^2 + \Omega_m(1+z)^3 + \Omega_r(1+z)^4] \quad (1.23)$$

## 1.1.2 The Scattering Particles

### The Boltzmann Equation

The macroscopic dynamics of the universe are governed by Equation 1.23, where it accurately describes how energy densities of different components evolve from the early universe to the present time. Nevertheless, in order to study the Big Bang Nucleosynthesis and the formation of CMB, we must tackle the microscopic interactions as well. The best starting point is to study the Boltzmann equation.

In a general form, the Boltzmann equation can be written as

$$\frac{df(\mathbf{x}, \mathbf{p}, t)}{dt} = C[f] \quad (1.24)$$

On the left hand side of the Equation 1.24, we have the distribution function  $f$ , where its time derivative is defined as

$$\frac{d}{dt} = \frac{\partial}{\partial t} + \dot{\mathbf{x}} \cdot \nabla_x + \dot{\mathbf{p}} \cdot \nabla_p \quad (1.25)$$

which consists of a time component, a location component, and a momentum component. On the right hand side of the Equation 1.24, we have the collision term, which describes the particle-particle interactions.

It is straightforward to rewrite the Boltzmann equation with the FLRW metric

$$\frac{\partial f}{\partial t} + \frac{p}{E} \frac{\hat{p}^i}{a} \frac{\partial f}{\partial x^i} - Hp \frac{\partial f}{\partial p} = C[f] \quad (1.26)$$

where  $\hat{p}^i$  is the unit vector for momentum  $p$ ,  $\hat{p}^i = \hat{p}_i$ . It is useful to look at two approximations that we can sometimes apply to the system. One approximation is for relativistic species like photons, where  $p \gg m$ . In this case, the Boltzmann equation can be simplified to

$$\frac{\partial f}{\partial t} + \frac{\hat{p}^i}{a} \frac{\partial f}{\partial x^i} - Hp \frac{\partial f}{\partial p} = C[f] \quad (1.27)$$

On the opposite extreme for massive particles like baryons, where  $p \ll m$ , the Boltzmann equation can be simplified to

$$\frac{\partial f}{\partial t} + \frac{p}{m} \frac{\hat{p}^i}{a} \frac{\partial f}{\partial x^i} - Hp \frac{\partial f}{\partial p} = C[f] \quad (1.28)$$

Let us now introduce two additional parameters to modify the FLRW metric introduced in Equation 1.4,  $\Phi$  and  $\Psi$ . With these two terms added, the metric becomes

$$\begin{aligned} g_{00}(\mathbf{x}, t) &= -1 - 2\Psi(\mathbf{x}, t) \\ g_{0i}(\mathbf{x}, t) &= 0 \\ g_{ij}(\mathbf{x}, t) &= a^2(t)\delta_{ij}[1 + 2\Phi(\mathbf{x}, t)] \end{aligned} \quad (1.29)$$

where  $\Psi$  introduces a Newtonian potential for non-relativistic entities, and  $\Phi$  prescribes a local perturbation to the scale factor  $a$ . Combined, they introduce a small modification ( $\sim \mathcal{O}(10^{-4})$ ) to the metric, and consequently, to the Boltzmann equation. Since the addition is relatively small, we can ignore the higher order term and simply work on the linear order terms.

In this perturb FLRW metric, the four-momentum becomes

$$P^\mu = \left[ E(1 - \Psi), p^i \frac{1 - \Phi}{a} \right] \quad (1.30)$$

where  $p^i$  is defined as

$$p^i = p \hat{p}^i \quad (1.31)$$

With these, the perturbed space component of the Boltzmann equation becomes

$$\frac{dx^i}{dt} = \frac{P^i}{P^0} = \frac{\hat{p}^i p}{a E} (1 - \Phi + \Psi) \quad (1.32)$$

and the perturbed momentum component becomes

$$\frac{dp^i}{dt} = -(H + \dot{\Phi})p^i - \frac{E}{a}\Psi_{,i} - \frac{1}{a}\frac{p^i}{E}p^k\Psi_{,k} + \frac{p^2}{aE}\Psi_{,i} \quad (1.33)$$

If we are interested in the magnitude of the momentum, we can then arrive at

$$\frac{dp}{dt} = -[H + \Phi]p - \frac{E}{a}\hat{p}^i\Psi_{,i} \quad (1.34)$$

Similarly, the direction of the momentum is

$$\frac{d\hat{p}^i}{dt} = \frac{E}{ap} [\delta^{ij} - \hat{p}^i \hat{p}^j] \left( \frac{p^2}{E^2} \Phi - \Psi \right)_{,k} \quad (1.35)$$

Equation 1.34 and Equation 1.35 combined nicely summarize the path of a particle that moves through an expanding universe with a field-like perturbation. There are numerous cosmic events that are observed to follow this pair of equations. For example, the lensing effect is governed by these two equations, which is caused by massive clusters in-between us and the CMB bending the path of CMB photons. In order to study the true form of CMB, we have to remove such effect. This process is called "delensing". On the other hand, measuring the lensing effect in the CMB map can also reveal a range of useful information regarding the cosmic history.

If we just focus on the perturbed equation for photon, where  $E = p$ , then we can combine Equation 1.32 and Equation 1.33 in linear order as

$$\frac{df}{dt} = \frac{\partial f}{\partial t} + \frac{\hat{p}^i}{a} \frac{\partial f}{\partial x^i} - \left[ H + \dot{\Phi} + \frac{\hat{p}^i}{a} \frac{\partial \Psi}{\partial x^i} \right] \frac{p \partial f}{\partial p} \quad (1.36)$$

which ultimately leads to the creation of anisotropies in the CMB observed today. We will tackle this equation again when we look at the inner working of anisotropies.

## Neutrinos

Following Equation 1.23, in the early universe, the energy density is dominated by the radiation term,  $\Omega_r$ . Relativistic particles that were held in thermal equilibrium contributed to the radiation density before they froze out of the plasma. The main



contributors to the radiation energy density are neutrinos and photons. Other particles like baryons had a negligible effect on the total energy due to their much lower density comparing to radiation or photon. Between photons and neutrinos, the contribution to radiation energy can be written as:

$$\rho = \frac{g\pi^2}{30}T_\gamma^4 + \frac{7}{8}\frac{g\pi^2}{30}T_\nu^4 \quad (1.37)$$

where photons behave as Bosons (first term), and neutrinos behave as Fermions (second term). Both terms share a degeneracy factor  $g$ . If we define the contribution from photons as  $\rho_\gamma$ , then Equation 1.37 can be re-written as:

$$\rho = \left[ 1 + \frac{7}{8} \left( \frac{T_\nu}{T_\gamma} \right)^4 N_\nu \right] \rho_\gamma \quad (1.38)$$

Early on when photons and neutrinos were held in thermal equilibrium, they were at the same temperature. As the universe cooled to below  $10^{10}$  K, neutrinos and antineutrinos can no longer be kept in the thermal equilibrium due to the annihilation scattering rate dropping below the expansion rate of the universe. As a result, neutrinos began to decouple from the plasma to form the cosmic neutrino background. Soon after the neutrinos froze out, temperature dropped below the mass of electron, and the electron-positron annihilation reheats the plasma, making the photon background hotter than the neutrino background. Based on entropy conservation, the ratio between the two temperature is:

$$\frac{T_\nu}{T_\gamma} = \left( \frac{g_2}{g_1} \right)^{1/3} \quad (1.39)$$

Where  $g_2$  is the degrees of freedom of all particles in the plasma after the electron-positron annihilation, and  $g_1$  is the same term before annihilation. Post-annihilation, only photons remain in the thermal equilibrium while others have negligible effect due to much smaller number density. Therefore, we have:

$$g_2 = 2 \tag{1.40}$$

As for pre-annihilation, we need to include the spin state from electron and positron in addition to photons, which means:

$$g_1 = 2 + \frac{7}{8} * 2 + \frac{7}{8} * 2 = \frac{11}{2} \tag{1.41}$$

Taking  $g_1$  and  $g_2$  into Equation 1.39, the temperature ratio is now:

$$\frac{T_\nu}{T_\gamma} = \left( \frac{4}{11} \right)^{1/3} \tag{1.42}$$

Where it is assumed that the neutrino decoupling and the electron-positron annihilation were well-separated in time. Taking Equation 1.42 into Equation 1.37, we arrive at:

$$\rho = \left[ 1 + \frac{7}{8} \left( \frac{4}{11} \right)^{4/3} N_\nu \right] \rho_\gamma \tag{1.43}$$

Where  $N_\nu = 3$  assuming the neutrinos are massless, and the decoupling is instantaneous.

Nevertheless, in reality the neutrinos are proven to have a non-zero mass  $\Sigma m_\nu$  [29]. The decoupling process also has an overlap with the electron-positron annihilation

period, allowing the neutrinos to receive entropy from the annihilation (for example, from charged-current processes), slightly increasing the neutrino energy density ( $\sim \mathcal{O}(1\%)$ ). To account for this effect,  $N_{eff}$  is introduced, in the form of:

$$\rho = \left[ 1 + \frac{7}{8} \left( \frac{4}{11} \right)^{4/3} N_{eff} \right] \rho_\gamma \quad (1.44)$$

The latest numerical calculation based on the standard model predict the effective number of neutrinos to be  $N_{eff} = 3.0440$  [28].

### 1.1.3 Big Bang Nucleosynthesis

Following the decoupling of neutrinos, the formation of light elements promptly begins. During this time, electron froze-out, hydrogen (and its isotopes') nuclei were formed, and so did helium (and its isotope's) nuclei. Some other light elements were also created during this time, but since their number density is much lower compared to hydrogen or helium, they will not be included in this discussion.

A slight variation of the Boltzmann equation from Equation 1.36 with the addition of the massive particle and a collision term leads to

$$a^{-3} \frac{d(n_1 a^3)}{dt} = n_1^{(0)} n_2^{(0)} \langle \sigma \nu \rangle \left[ \frac{n_3 n_4}{n_3^{(0)} n_4^{(0)}} - \frac{n_1 n_2}{n_1^{(0)} n_2^{(0)}} \right] \quad (1.45)$$

This is used to describe the number density  $n_1$  for species 1 in a generic reaction



where the mean cross section is shortened as  $\langle \sigma \nu \rangle$ .

Intuitively, when the particle is held in thermal equilibrium via scattering or annihilation, the reaction rate of the particle should be much higher than the expansion rate of the universe. With this in mind, if we look at Equation 1.45, on the left of the equation, we have  $\sim \mathcal{O}(n_1 H)$ , while on the right hand side of the equation, we have  $\sim \mathcal{O}(n_1 n_2 \langle \sigma \nu \rangle)$ . If  $H \ll n_2 \langle \sigma \nu \rangle$ , then we must have

$$\frac{n_1 n_2}{n_1^{(0)} n_2^{(0)}} = \frac{n_3 n_4}{n_3^{(0)} n_4^{(0)}} \quad (1.47)$$

This is also known as the Saha equation, and from our derivation, it holds as long as the system is in the equilibrium state.

Equation 1.47 is very powerful in that it applies to many types of scattering. For example, if we are to look at the weak interactions between protons and neutrons



One can apply Equation 1.45 and arrive at

$$a^{-3} \frac{d(n_n a^3)}{dt} = n_l^{(0)} \langle \sigma \nu \rangle \left[ \frac{n_p n_n^{(0)}}{n_p^{(0)}} - n_n \right] \quad (1.49)$$

where  $n_l$  is the lepton density. If we ignore helium nucleus due to its much lower number density, we can define  $X_n$  as the ratio of neutrons to total nuclei in the form of

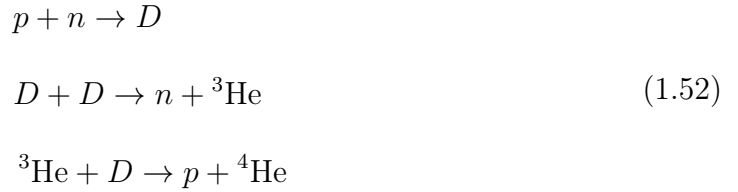
$$X_n \equiv \frac{n_n}{n_n + n_p} \quad (1.50)$$

Then from Equation 1.49, we can derive the rate of change for  $X_n$  as

$$\frac{dX_n}{dt} = n_l^{(0)} \langle \sigma \nu \rangle [(1 - X_n)e^{-(m_n - m_p)/T} - X_n] \quad (1.51)$$

In reality, however, Equation 1.51 only holds when expansion rate is much slower than the reaction rate. As the temperature cools to  $T \sim 1$  MeV and the reaction rate drops below the expansion rate, neutron froze out and cease to follow the analytical value predicted by  $X_n$ . As a result, at the onset of Big Bang Nucleosynthesis ( $T \sim 0.07$  MeV), we have  $X_{n,pre-BBN} \sim 0.11$ , instead of a much smaller amount according to the analytical result.

During the main synthesis event, the majority of the neutron went into helium nucleus via the reaction



Therefore, the  ${}^4\text{He}$  abundance  $Y_p$  is

$$Y_p = 2X_{n,pre-BBN} \quad (1.53)$$

which provides  $Y_p \sim 0.22$  based on a rough estimation. A more detailed numerical integration calculation performed in 2018 can be found in [66], which provides the value

$$Y_p = 0.24705 \pm 0.00019 \quad (1.54)$$

This is consistent with the latest measurement from Planck [67] that shows

$$Y_p^{Planck} = 0.24714 \pm 0.00049 \quad (1.55)$$

### 1.1.4 The Epoch of Recombination

The universe remains ionized for the next 380,000 years as the temperature continues to decrease to  $\sim 1 \text{ eV}$ . During this time, as soon as any neutral hydrogen is formed, it is immediately re-ionized by energetic photons. Eventually, expansion of the universe cooled the photon enough such that they can no longer overcome the hydrogen binding energy. Thus began the recombination era.

In short, the recombination is about the reaction



From the Saha equation (Equation 1.47), we have

$$\frac{n_e n_p}{n_H} = \frac{n_e^{(0)} n_p^{(0)}}{n_H^{(0)}} \quad (1.57)$$

when the system is in equilibrium. In reality, neutral helium also formed at a slightly earlier time, but due to helium's much lower number density, we will only focus on hydrogen in this section. Similar to  $X_n$ , we define the free electron fraction  $X_e$  as

$$X_e \equiv \frac{n_e}{n_e + n_H} \quad (1.58)$$

Then from Equation 1.45 we have

$$\frac{dX_e}{dt} = [(1 - X_e) \langle \sigma\nu \rangle \left(\frac{m_e T}{2\pi}\right)^{\frac{3}{2}} e^{-\epsilon_0/T} - X_e^2 (n_e + n_H) \langle \sigma\nu \rangle] \quad (1.59)$$

where  $\epsilon_0$  is the hydrogen binding energy at 13.6 eV.

From Equation 1.59, it is natural to define the recombination rate as

$$\omega_r \equiv \langle \sigma\nu \rangle \quad (1.60)$$

which scales rapidly as the temperature drops below 1 eV. With the acceleration of recombination, photons that were efficiently scattered by free electrons started to decouple. Most of them scattered for one last time<sup>3</sup>, and then started traveling in straight lines, going through eons until they finally reached Earth today. Thus was born the CMB.

## 1.2 Decoding the CMB

As stated above, the photon imprints produced at the last scattering surface essentially preserved the energy distribution of the universe at that moment until present day. Therefore, by observing the CMB, one can gain much insight into the matter composition, density distribution, and particle interactions before the recombination. These information are encoded in the CMB temperature and polarization maps, and are usually extracted by calculating the power spectrum of these maps and fitting for the corresponding parameters given a model of the universe.

---

<sup>3</sup>A small portion of them do scatter again later due to some other effects. One example would be via Sunyaev-Zeldovich (SZ) effect.

### 1.2.1 The Theory of Inflation

To first order, the CMB observed today is a very smooth black-body radiation curve with a temperature of  $T_0 = 2.7260 \pm 0.0013$  K, as measured by the Far InfraRed Absolute Spectrophotometer (FIRAS) on-board the Cosmic Background Explorer (COBE) satellite [27]. The smoothness ( $< 0.1\%$  variation) of CMB led to a basic assumption that our universe is isotropic and homogeneous. This gives rise to an issue - the horizon problem. If we consider the comoving horizon defined as

$$\eta(a) \equiv \int_0^a \frac{d\ln(a')}{a'H(a')} \quad (1.61)$$

which represents a patch size that could be in casual contact at scale factor  $a$ . Since  $\eta$  is monotonically increasing, it can also be used to track the age of the universe, and is known as the "conformal time". During recombination,  $\eta_{reco} \sim 2.8 \times 10^2 h^{-1}$  Mpc. However, at present day,  $\eta_0$  has grown to  $\sim 1.4 \times 10^4 h^{-1}$  Mpc. This means that any two patches that are more than  $\sim 1.2^\circ$  apart on today's sky cannot be in casual contact during recombination. Why would the end result be this smooth if these patches have no way of communicating with each other?

Another issue that arises is the flatness problem. The  $\Omega_\kappa$  introduced in Equation 1.20 is measured to be  $\sim 0.001$  [67], which suggests that the universe is very flat. However, as the definition suggests, the curvature would grow rapidly as the universe evolve. In fact, the curvature measured today means that the universe has to have a density  $|\rho - \rho_{cr}|/\rho < 10^{-55}$  at the early stage, based on Alan Guth's original derivation [37]. Why would the universe be this flat to begin with?

Both problems can be solved by the theory of inflation. This theory includes a



tiny starting point, an exponential expansion, and a short duration, as qualitatively described in Section 1.1. The small starting point reduces the comoving Hubble radius dramatically, resulting in everything in casual contact with each other at early times. The exponential expansion ensures that the curvature were driven to near zero as  $\Omega_\kappa \propto (aH)^{-2}$ . The short duration means that it ended quickly, as we do not see rapid expansion all the way to today.

There are many theories as to what drives the inflation. The simplest among them prescribes a potential energy of a scalar field with a negative pressure. In this model, the field  $\phi$  slowly rolls down the potential  $V(\phi)$  until it reached its minimum. As  $\phi$  changes slowly, so will  $H$ . We can thus define a small parameter  $\epsilon_\phi$  such that

$$\epsilon_\phi \equiv \frac{d}{dt} \left( \frac{1}{H} \right) = - \frac{dH/d\eta}{aH^2} \quad (1.62)$$

One famous prediction from inflation is that it will produce both scalar and tensor perturbations in the CMB, and some of them are observable today, long after inflation and recombination.

In short, the magnitude of tensor mode perturbation is

$$P_T(k) = \frac{32\pi GH^2}{k^3} \Big|_{\text{horizon crossing}} \quad (1.63)$$

and the magnitude of scalar mode perturbation is

$$P_S(k) = \frac{2\pi GH^2}{k^3 \epsilon_\phi} \Big|_{\text{horizon crossing}} \quad (1.64)$$

Both equations are written in the Fourier  $k$ -space, and are evaluated when mode  $k$

crosses the horizon. From Equation 1.63 and Equation 1.64, we can define their ratio as

$$r(k) \equiv \frac{P_T(k)}{P_S(k)} = 16\epsilon_\phi \Big|_{\text{horizon crossing}} \quad (1.65)$$

which, remarkably, can be measured from the CMB. Since this tensor-to-scalar ratio  $r$  provides a unique probe for the inflation model and its driver  $\phi$ , it is a vital measurement that the CMB science community is striving to improve upon.

### 1.2.2 Anisotropies in the CMB

Even though the CMB temperature is very smooth, tiny anisotropies are discovered in it. Countless research and astounding results spring from studying the shape and form of these anisotropies. In order to understand how they are observed, it is useful to introduce a fractional temperature fluctuation term  $\Theta$  as

$$T(\mathbf{x}, \hat{\mathbf{p}}, t) = T(t)[1 + \Theta(\mathbf{x}, \hat{\mathbf{p}}, t)] \quad (1.66)$$

where  $x$  is the location of the observer,  $\hat{p}$  is the direction of momentum of the observed photons. Since we only have one sky and can only make observation at current time  $t_0$ , the real variable in Equation 1.66 is  $\hat{p}$ , where we record  $\Theta$  in terms of locations of the photon on the sky. Since the sky-shaped temperature map can be viewed as a sphere, it is convenient to expand it in the basis of spherical harmonics  $Y_{lm}$

$$\Theta(\mathbf{x}, \hat{\mathbf{p}}, t) = \sum_{l=1}^{\infty} \sum_{m=-l}^l a_{lm}(\mathbf{x}, t) Y_{lm}(\hat{\mathbf{p}}) \quad (1.67)$$

where  $l$  is the multipole moment of the spherical harmonics, and  $m$  is its azimuthal degree of freedom. From Equation 1.67, we can invert the relationship and write  $a_{lm}$  in terms of  $\Theta$  in Fourier  $k$ -space

$$a_{lm}(\mathbf{x}, t) = \int \frac{d^3k}{(2\pi)^3} e^{i\mathbf{k}\cdot\mathbf{x}} \int d\Omega Y_{lm}^*(\hat{\mathbf{p}}) \Theta(\mathbf{k}, \hat{\mathbf{p}}, t) \quad (1.68)$$

When observed at current time on Earth, Equation 1.68 can be simplified to

$$a_{lm} = (-i)^l \int \frac{d^3k}{(2\pi)^3} Y_{lm}^*(\hat{\mathbf{p}}) \Theta(\mathbf{k}, \hat{\mathbf{p}}) \quad (1.69)$$

where the variance  $C(l)$  of  $a_{lm}$  can be calculated by

$$C(l) \delta_{ll'} \delta_{mm'} = \langle a_{lm} a_{l'm'}^* \rangle \quad (1.70)$$

But what constitutes the theoretical value for  $\Theta$ ? In essence, we can acquire an analytic understanding of it by solving the evolution of a perturbed Boltzmann equation for photon. If we continue along Equation 1.36, and attempt to solve the Boltzmann equation explicitly, we can expand  $f(\mathbf{x}, \hat{\mathbf{p}}, t)$  to first order in  $\Theta$  as

$$f(\mathbf{x}, \hat{\mathbf{p}}, t) \approx f^{(0)} - \Theta(\mathbf{x}, \hat{\mathbf{p}}, t) \frac{p \partial f^{(0)}}{\partial p} \quad (1.71)$$

where  $f^{(0)}$  is defined as

$$f^{(0)} \equiv [e^{p/T} - 1]^{-1} \quad (1.72)$$

where (0) means the distribution function for zero chemical potential case.

Now we can calculate  $df/dt$  as

$$\begin{aligned}\frac{df}{dt} &= \frac{df^{(0)}}{dt} - \frac{d}{dt}\Theta(\mathbf{x}, \hat{\mathbf{p}}, t)\frac{p\partial f^{(0)}}{\partial p} \\ &= -\frac{p\partial f^{(0)}}{\partial p} \left[ \dot{\Theta} + \dot{\Phi} + \frac{\hat{p}^i}{a} \left( \frac{\partial \Psi}{\partial x^i} + \frac{\partial \Theta}{\partial x^i} \right) \right]\end{aligned}\quad (1.73)$$

where  $\Phi$  and  $\Psi$  are the same metric perturbation introduced in Equation 1.29. Recall from Equation 1.24 that to solve for  $\Theta$ , we still need the collision term  $C[f]$ , which has a text book expression given by [24]:

$$C[f] = -\frac{p\partial f^{(0)}}{\partial p}(n_e\sigma_T)[\Theta_0 - \Theta(\hat{\mathbf{p}}) + \hat{\mathbf{p}} \cdot \mathbf{u}_e] \quad (1.74)$$

where  $\mathbf{u}_e$  is the bulk velocity of electron-proton-photon plasma, and  $\Theta_l$  is the  $l$ th multipole moment of  $\Theta$  defined as

$$\Theta_l \equiv \frac{1}{(-i)^l} \int_{-1}^1 \frac{d(\hat{\mathbf{p}} \cdot \hat{\mathbf{k}})}{2} P_l(\hat{\mathbf{p}} \cdot \hat{\mathbf{k}}) \Theta(\mathbf{k}, \hat{\mathbf{p}}, t) \quad (1.75)$$

Here  $P_l$  is the Legendre polynomials. Combining Equation 1.73 and Equation 1.74 as  $df/dt = C[f]$ , we finally arrive at the complete Boltzmann equation for photon

$$\left[ \dot{\Theta} + \dot{\Phi} + \frac{\hat{p}^i}{a} \left( \frac{\partial \Psi}{\partial x^i} + \frac{\partial \Theta}{\partial x^i} \right) \right] = (n_e\sigma_T)[\Theta_0 - \Theta(\hat{\mathbf{p}}) + \hat{\mathbf{p}} \cdot \mathbf{u}_e] \quad (1.76)$$

The left hand side of Equation 1.76 represents the evolution of the distribution function, while the right hand side expresses the photon-electron scattering interaction. This equation relates the two.

Although Equation 1.76 is very powerful, solving it proves to be no easy task.

Fortunately, there is no need to solve  $\Theta_l$  for all multipole moments, since the temperature anisotropies are dominated by the monopole moment  $\Theta_0$  and dipole moment  $\Theta_1$ . If we make the approximation by dropping the higher multipole moment, we can consider the tightly coupled plasma to obey fluid dynamics similar to a forced harmonic oscillator. With this analogy in mind, we can define the sound speed of the fluid as

$$c_s(\eta) \equiv \sqrt{\frac{1}{3(1 + \frac{3\rho_b(\eta)}{4\rho_\gamma(\eta)})}} \quad (1.77)$$

where we use the conformal time  $\eta$  defined in Equation 1.61 to replace conventional time  $t$ , and  $\rho_b$ ,  $\rho_\gamma$  to represent the baryon density and photon density respectively. Following this, the sound horizon of the fluid can be defined as

$$r_s(\eta) \equiv \int_0^\eta d\eta' c_s(\eta') \quad (1.78)$$

Even with the fluid approximation, writing down the exact form for  $\Theta_l$  is quite complicated. Here we will abbreviate the form of  $\Theta_0$  and  $\Theta_1$  as presented in the original derivation by Wayne Hu and Naoshi Sugiyama [44]:

$$\begin{aligned} \Theta_0 &= [A\cos(kr_s) + B\sin(kr_s)]D(\eta, k) \\ \Theta_1 &= \frac{1}{\sqrt{3}}[A\sin(kr_s) - B\cos(kr_s)]D(\eta, k) \end{aligned} \quad (1.79)$$

where  $A$  and  $B$  are constants based on the photon-baryon density ratio and the perturbation scale  $\Phi$  and  $\Psi$ . The term  $D(\eta, k)$  represents the diffusion damping term defined as

$$D(\eta, k) = e^{-(k/k_D)^2} \quad (1.80)$$

where  $k_D$  is the damping scale. The damping happens due to the finiteness of photon scattering. Consider the scattering rate in Equation 1.76 ( $n_e\sigma_T$ ), if this rate is infinite, there would be no damping. However, during a course of a Hubble time  $1/H$ , photon would on average only scatter  $(n_e\sigma_T)/H$  times, traveling on average a comoving distance  $1/\sqrt{(n_e\sigma_T)a^2H}$ . Over this distance, the difference between hot and cold spots will be smeared by photons, and thus the anisotropies damped. A whole range of small scale CMB science depends on the accurate measurement of the damping scale  $k_D$ .

There is yet another piece to the puzzle. After recombination, photons still have a long way to travel before reaching the detector on Earth. During this period, it is affected by the evolution of potentials. Such effect is called the integrated Sachs-Wolfe (ISW) effect, which is mainly due to the contribution from radiation energy at early time, and from dark energy at late time.

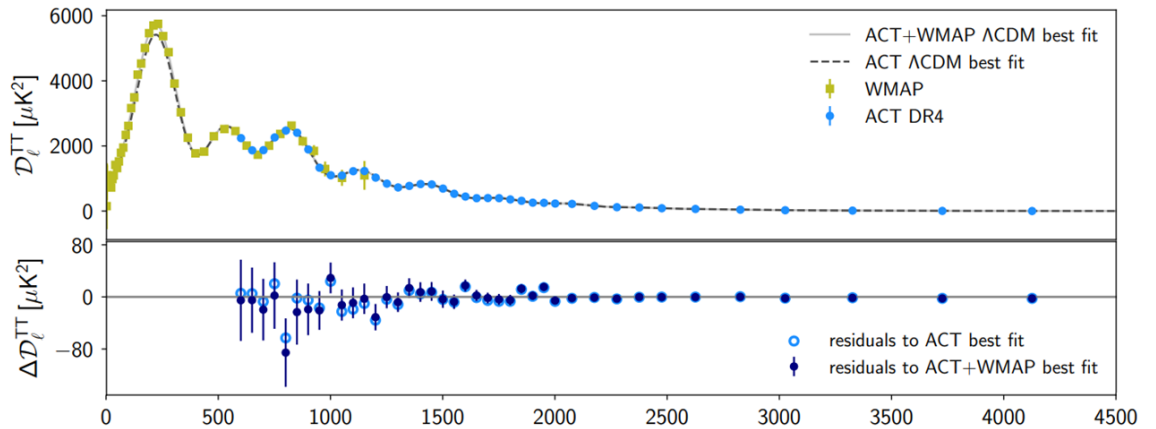


Figure 1.3: This plot shows the latest temperature anisotropy measurement presented by Atacama Cosmology Telescope (ACT) collaboration in combination with Wilkinson Microwave Anisotropy Probe (WMAP) data, ranging from  $l = 0$  to  $l = 4500$ . The upper panel shows the measurements, while the lower panel shows the deviation from measured points to theoretical prediction. Figure credit: ACT DR4 maps and cosmological parameters.

Finally, a linear combination of  $\Theta_0$  and  $\Theta_1$  from Equation 1.79, and the addition of ISW effect constitutes the bulk of the temperature anisotropies  $\Theta$  that we observe today, in the form of

$$\Theta_l(k) \approx J_1[\Theta_0(k) + \Psi(k)] + J_2 3\Theta_1(k) + J_{ISW} \quad (1.81)$$

Here  $J_1$ ,  $J_2$ , and  $J_{ISW}$  are composed of a series of  $l$  dependent spherical Bessel functions. One of the latest measurement of such anisotropies presented by ACT collaboration [7] is shown in Figure 1.3. The y-axis value  $D_l$  is defined as

$$D_l \equiv \frac{l(l+1)}{2\pi} C(l) T_{CMB}^2 \quad (1.82)$$

where  $C_l$  is the variance defined in Equation 1.70. The peaks and troughs in this figure are directly related to the peaks and troughs from  $\Theta_0$  and  $\Theta_1$ , amplified or attenuated by ISW effect. One can also observe the effect of diffusion damping at high  $l$ .

## 1.3 Next Generation CMB Observation

### 1.3.1 Progress Made So Far

As presented above, observations of the CMB are crucial tools in developing our understanding of the physics of the early universe and testing the standard model of cosmology,  $\Lambda$ CDM [16]. While satellite missions such as the Cosmic Background Explorer (COBE) [74], the Wilkinson Microwave Anisotropy Probe (WMAP) [11; 43],

and the Planck Collaboration [68] have produced full-sky microwave maps, ground-based experiments have extended the satellite measurements towards smaller angular scales and lower noise levels over 40% the sky. High resolution ( $\sim 1'$ ) experiments, such as the Atacama Cosmology Telescope [80] (ACT) and the South Pole Telescope [13; 73] (SPT) have made measurements of both the primordial temperature power spectrum [84] as well as secondary anisotropies such as the thermal and kinematic Sunyaev-Zel'dovich (SZ) effects [42; 76; 77] and gravitational lensing effects [75]. Low resolution experiments ( $\sim 0.5^\circ$ ), such as the Background Imaging of Cosmic Extragalactic Polarization (BICEP) and Keck Arrays [3; 46], the SPIDER [33], the Atacama B-mode Survey (ABS) [49], the POLARBEAR [4; 69], and the Cosmology Large Angular Scale Surveyor (CLASS) [86; 38] aim to improve measurements on B-mode polarization, one of the two components in CMB polarization [45], at larger angular scales ( $\ell \lesssim 200$ ).

The last decade has seen a significant amount of detection and numerous highly accurate measurements. However, there is more science to be gained from the upcoming CMB experiments, among which are the Simons Observatory (SO) and CMB-S4. An in-depth review from the CMB-S4 collaboration [2], with the current CMB temperature, E-mode polarization, and B-mode polarization measurements shown in Figure 1.4. The abundance of science sought by the next generation CMB observatories include better constraints on various cosmological parameters, searching for B-mode polarization due to primordial gravitational waves, measuring the effective number of light relativistic species, detecting the sum of the neutrino masses, providing test on dark energy properties, and testing alternative theories for gravity on large scales.



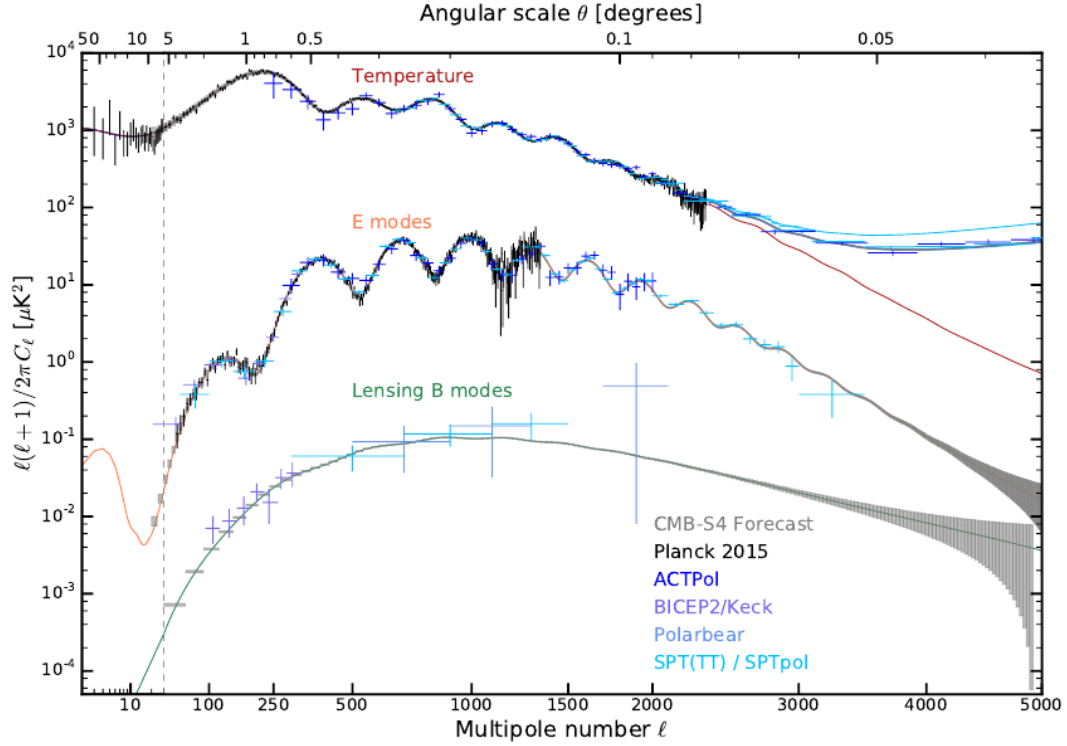


Figure 1.4: The current power spectrum of the CMB in temperature, E-mode polarization, and B-mode polarization. Figure credits: CMB-S4 Science Book.

### 1.3.2 SO Science Goals

The key science goals for SO is summarized in Table 1.1, and discussed in details in SO science and forecast paper [79]. The nominal forecast result is shown in the SO-Baseline column, where the uncertainty was assumed to be at 25% to account for additional systematic errors from the instruments. Below, I present a brief summary of the SO forecast result.

SO aims to improve our understanding on the primordial perturbations by measuring the tensor-to-scalar ratio  $r$  (derived in Equation 1.65), scalar perturbations, and non-Gaussian perturbations. The SO Small Aperture Telescope (SAT) will be

Parameter	SO-Baseline (no syst)	<b>SO-Baseline</b>	SO-Goal	Current
$r$	0.0024	<b>0.003</b>	0.002	0.03
$e^{-2\tau}\mathcal{P}(k = 0.2/\text{Mpc})$	0.4%	<b>0.5%</b>	0.4%	3%
$f_{\text{NL}}^{\text{local}}$	1.8	<b>3</b>	1	5
$N_{\text{eff}}$	0.055	<b>0.07</b>	0.05	0.2
$m_\nu$	0.033	<b>0.04</b>	0.03	0.1
$\sigma_8(z = 1 - 2)$	1.2%	<b>2%</b>	1%	7%
$H_0$ ( $\Lambda$ CDM)	0.3	<b>0.4</b>	0.3	0.5
$\eta_{\text{feedback}}$	2%	<b>3%</b>	2%	50-100%
$p_{\text{nt}}$	6%	<b>8%</b>	5%	50-100%
$\Delta z$	0.4	<b>0.6</b>	0.3	1.4

Table 1.1: Summary of SO key science goals. The SO forecasts assume that SO is combined with Planck data. The forecasts here are presented in three columns. The first column is the baseline noise level with no additional systematic error. The second column represents the nominal forecast, with a 25% additional uncertainties to account for potential instrument systematics. The third column represents the goal forecast, which assumes negligible systematic uncertainties, and rounds to one significant figure.

capable of achieving  $\sigma(r) = 0.003$ , which would confirm or rule out models that prescribe  $r \geq 0.01$ . The SO Large Aperture Telescope (LAT) will use the temperature and E-mode polarization map at small scales to provide constraints on scalar perturbations with 20  $k$  bins between  $k = 0.001 \text{ Mpc}^{-1}$  and  $k = 0.35 \text{ Mpc}^{-1}$ , which will test the almost-scale-invariant prediction of inflation, as discussed in Section 1.2.1. Non-Gaussianity measurement has a baseline forecast at  $\sigma(f_{\text{NL}}^{\text{local}}) = 3$ , which will be obtained from both correlating the LAT-measured kSZ effect and the LAT-measured CMB lensing field with the galaxy distribution from Vera C. Rubin Observatory [14]. Local primordial non-Gaussianity can be used to potentially rule out single field

inflation models described in Section 1.2.1.

For the effective number of relativistic species  $N_{eff}$  (defined in Equation 1.44), SO will be able to measure  $\sigma(N_{eff}) = 0.07$  by fitting for the damping scale  $k_D$ , confirming or ruling out some of the potential light relics beyond the standard model. SO will also be able to measure the total mass of the three neutrino flavors to an accuracy of  $\sigma(\Sigma m_\nu) = 0.04 eV$ , potentially providing a confirmation for a non-zero neutrino mass sum. This will be achieved from CMB lensing, SZ clusters, and thermal SZ distortion measurements.

The amplitude of matter perturbations,  $\sigma_8$ , is defined as the root mean square overdensity in a sphere with radius  $8h^{-1}$  Mpc. It provides crucial insight on structure growth and will be constrained by SO at 2% level between  $z = 1-2$  using SZ clusters and CMB lensing measurements from LAT. In addition, SO aims to reduce the current uncertainty on the Hubble constant  $H_0$  (defined in Equation 1.14) to 0.4 km/s/Mpc with LAT temperature and polarization power spectra, enhancing the significance of the discrepancy with  $H_0$  derived from the CMB and from Hubble diagram at low redshift. Currently, this discrepancy between indirect measurements of  $H_0$  from the early universe cosmology and direct measurements of  $H_0$  from late-time Cepheids stars is not well explained by the standard model, and could come from residual systematics or new physics.

SO will contribute to our understanding of the galaxy evolution by measuring the feedback efficiency,  $\eta_{feedback}$ , to 3% uncertainty. The feedback effect is largely due to the formation of stars and black holes, altering the inter-galactic matter distribution. SO will also measure the degree of non-thermal pressure support,  $p_{nt}$  to 8% uncertainty. Currently, no strong limits exist on these parameters that are

crucial to models of galaxy evolution. Both constraints will come from temperature measurements from LAT.

Finally, SO will measure the duration of reionization,  $\Delta z$ , with an uncertainty of 0.6, less than half of the current best constraint using LAT temperature and polarization maps. This will help constrain models for the ionization process, and provide properties on the first galaxies, quasars, and the intergalactic medium in the reionization epoch.

# Chapter 2

## SO LATR Design

### 2.1 SO LATR Design and Operation Guideline

SO [79; 30] is a next generation CMB experiment consisting of three 0.42 m SATs [9] and one 6 m LAT [65] in the Atacama Desert of Chile. As reviewed by CMB-S4 [2], both large and small telescopes are needed to capture the CMB at small and large scales. All of these instruments are designed and built upon a series of requirements extracted from the science goals outlined in Section 1.3. This thesis will only discuss the LAT considerations. The bulk of the content presented in Chapter 2 and Chapter 3 is also published in [89], of which I was a lead author.

#### 2.1.1 Detector Count and Operating Temperature

The LAT utilizes a crossed-Dragone optical design with a pair of 6 m mirrors [31; 35]. A cross section view of the LAT is shown in Figure 2.1. Inside LAT's receiver cabin, we will install the Large Aperture Telescope Receiver (LATR) [89; 63; 85], which can

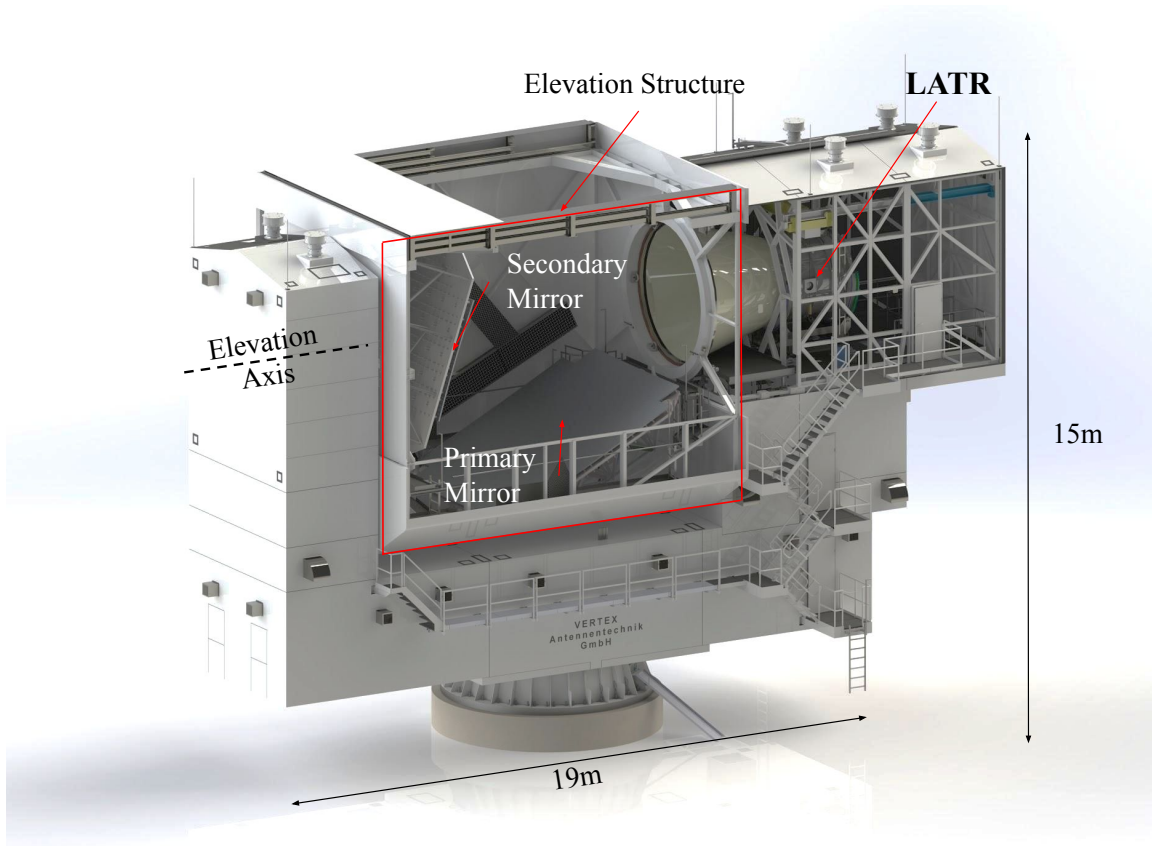


Figure 2.1: The LATR in the LAT. This shows a cutaway rendering of the LAT with the LATR installed in the receiver cabin. The elevation structure is labeled with the 6 m primary and secondary mirrors inside. As the telescope changes observation elevation by rotating the elevation structure, the LATR co-rotates – maintaining a consistent orientation between the LATR and the primary and secondary mirrors. This figure is taken from [89].

contain up to 13 optics tubes and will cover six frequency bands centered around 27, 39, 93, 145, 225, and 280 GHz, grouped into low-frequency (LF) band (27 and 39 GHz), mid-frequency (MF) band (93 and 145 GHz), and ultra-high-frequency (UHF) band (225 and 280 GHz). The optics tube is a self-contained unit including components at 4 K, 1 K, and 100 mK. Its detailed design is discussed in Section 2.2.6. Each optics tube will contain three detector wafers filled with transition edge sensor (TES) bolometers, capable of observing  $\sim 1.3^\circ$  of sky when combined. All wafers will operate at 100 mK and measure a single band group with dichoric pixels that are sub-divided into two linear polarizations. The initial survey will use seven optics tubes in the nominal configuration with the remaining six positions allowing for future upgrades. The band group distribution is included in Table 2.1. The LATR is 2.6 m in length, 2.4 m in diameter, and  $11 \text{ m}^3$  in volume. It is installed on a bore-sight rotation mount to maintain a constant pointing on the secondary mirror and uses a  $6.7^\circ$  field of view out of the  $7.8^\circ$  available.

A detailed design study was performed to optimise the overall sensitivity of the instrument while considering the technical challenges and the timeline of the program. For example, the size of the focal plane on the LAT could accommodate a 19 tube LATR, but this was deemed too technically risky and a 13 optics tube LATR was chosen as the best balance between meeting the near term goals of SO while allowing for significant future upgrade. A 100 mK dilution refrigerator was chosen since it provides continuous operation and increased sensitivity over a 300 mK He-3 adsorption cooled system [60; 1]. Such a system has been successfully operating on ACT since 2011. The sensitivity that SO is capable of achieving is included in Table 2.1. For MF and UHF band group, we choose to couple the TES bolometers to monolithic feedhorn

Frequency (GHz)	FWHM (arcmin)	Baseline noise ( $\mu\text{K-arcmin}$ )	Goal noise ( $\mu\text{K-arcmin}$ )	Bands	Detector Number	Optics Tubes
25	8.4	71	52	LF	222	1
39	5.4	36	27		222	
93	2.0	8.0	5.8	MF	10,320	4
145	1.2	10	6.3		10,320	
225	0.9	22	15	UHF	5,160	2
280	0.8	54	37		5,160	

Table 2.1: The SO LAT projected survey sensitivity with  $f_{sky} = 0.4$ . This represents the nominal configuration for the first deployment, with seven of the 13 optics tubes installed (see Section 2.2.6 for optics tube design). The quoted detector numbers assume three detector wafers per optics tube. With the use of dichroic pixels, the six targeted bands are split into three categories: low-frequency (LF), medium-frequency (MF), and ultra-high-frequency (UHF). The baseline sensitivity includes an additional uncertainty factor to account for approximated instrument systematic noise, while the goal sensitivity assumes the instrument noise is negligible. A detailed explanation of the value here can be found in [79].

arrays that were well-tested in the Advanced ACT receiver [15; 40; 26]. For LF band group, we will couple sinuous antennas with lenslet coupling that were successfully deployed in POLARBEAR [78] and the SPT [64; 70]. To limit the noise level from atmosphere and readout electronics, half-wave plates were initially considered for the LATR, but they were ruled out for the final design. This is due to LATR’s main focus on small-scale science, and the  $1/f$  noise achieved by ACTPol without a half-wave plate [20] is found to be sufficient in the SO science goals and forecast study [79].

### 2.1.2 Scanning Strategy

Over a five year observing period, we plan to use the LAT to survey  $\sim 40\%$  of the sky with arcminute resolution and a map noise level of  $\sim 6 \mu\text{K-arcmin}$  in the 93 and 145 GHz bands (see Table 2.1). While it is possible to have LAT focusing on 10% of the sky and maximizing the overlapping region with SAT for dedicated delensing, it will



sacrifice a large portion of the LAT science goals while achieving similar delensing levels that can be obtained from external maps or the cosmic infrared background [79; 88]. Overlapping with existing and upcoming optical surveys, the SO will be able to measure cross correlations of the SO reconstructed lensing potential with the Vera C. Rubin Observatory [14] identified galaxies, and provide tighter constraints on the neutrino mass by combining SO data with Dark Energy Spectroscopic Instrument (DESI) [21] baryon acoustic oscillation (BAO) information. Additionally, the LAT will detect tens of thousands of clusters using the thermal SZ effect, as well as numerous extra-galactic sources and transient microwave objects [59; 36]. There are even prospects for the LAT to detect Oort clouds around nearby stars [12; 62] or additional planets in our Solar System [10]. Finally, although the nominal plan is to rely on external delensing, observations made with the LAT can be used to cross-check the delensing factor and help reduce the uncertainty on the large scale B-mode signals [5] measured with the SATs.

## 2.2 LATR Mechanical Design

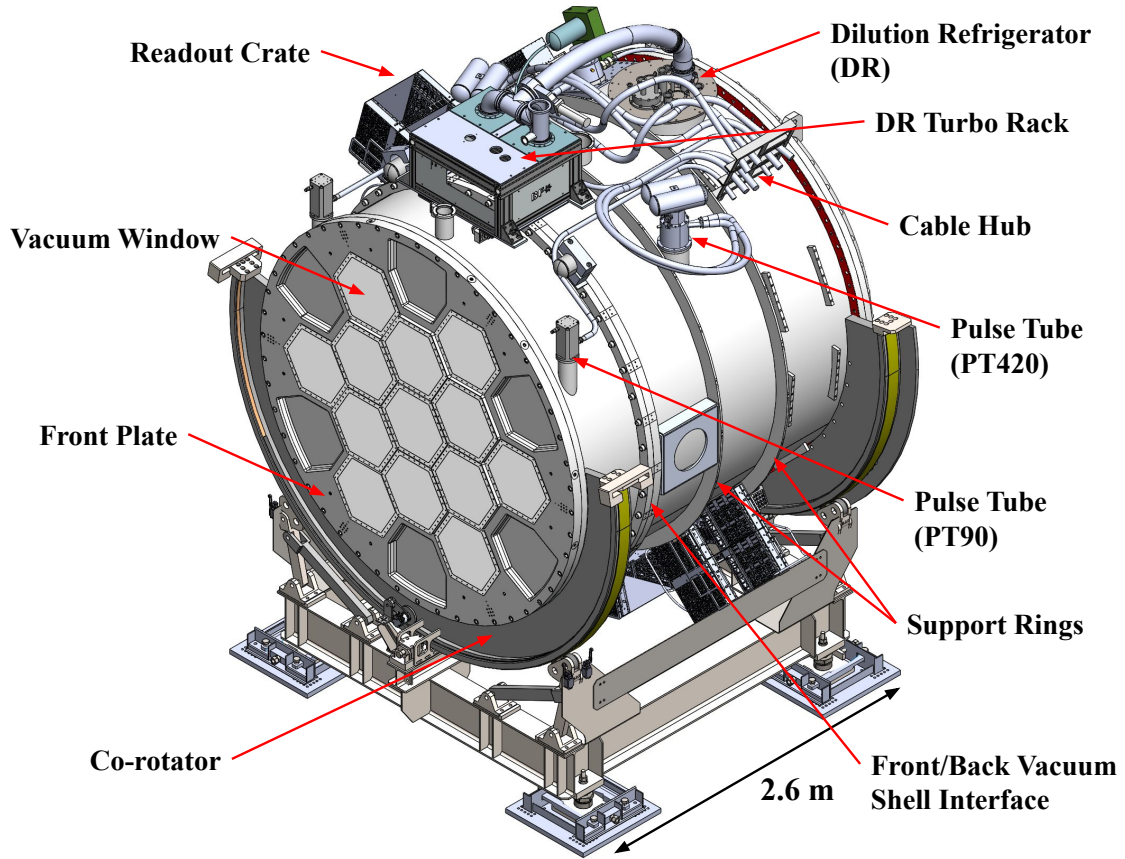


Figure 2.2: LATR external components are shown in this figure. The front plate with 13 hexagonal windows is labeled. The co-rotator at the bottom supports the LATR in the LAT (Figure 2.1), and allows the LATR to maintain its orientation with respect to the LAT mirrors when the telescope changes elevation. Two of the pulse tube coolers on one side are labeled, including a one-stage 80 K cooler (PT90) and a two-stage 40 K/4 K cooler (PT420). The DR at the back of the LATR is labeled. Also labeled is one of the readout crates around the LATR, which house a number of critical electronics for detector data readout. All hoses and cables travel to the central hub (metal frame on the top right) on the cryostat before going to the cable wrap (Figure 2.1).

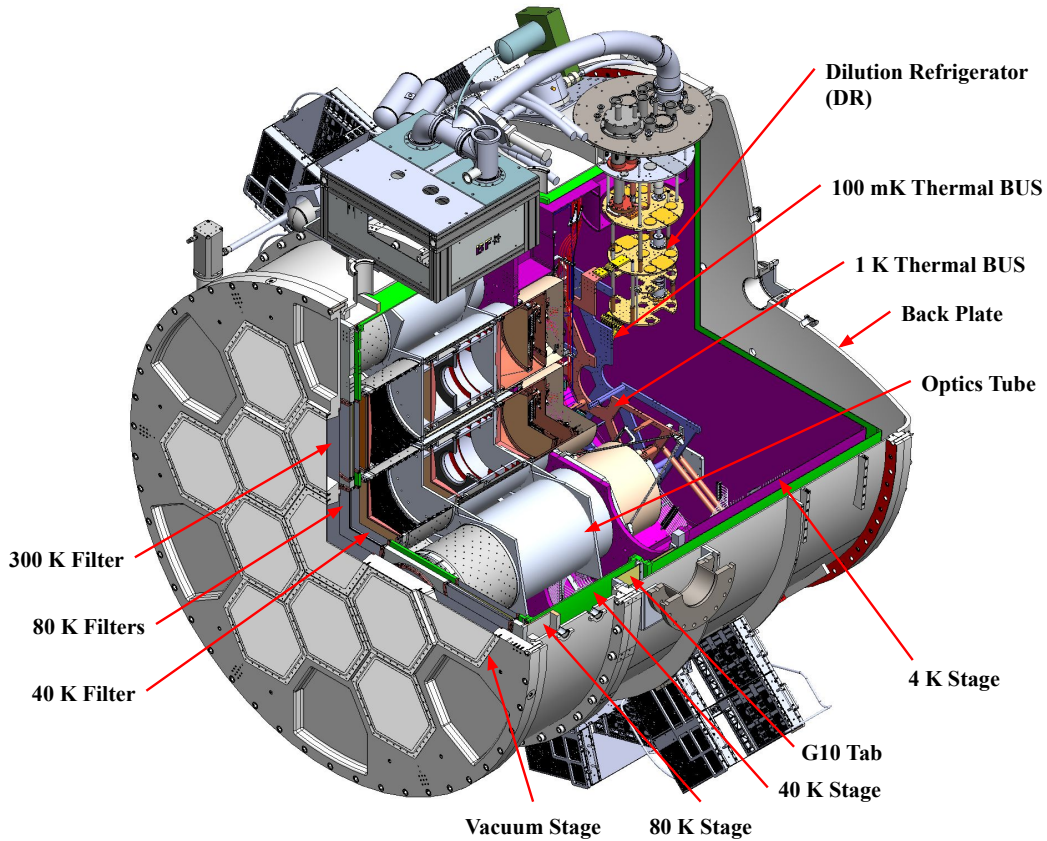


Figure 2.3: The LATR cut-out to display the internal structures. From the front to the back, the LATR consists of the 300 K vacuum stage, 80 K stage (grey), 40 K stage (green), and 4 K stage (purple). The 80 K stage is supported by 12 G-10 tabs from the front of the vacuum shell; the 40 K stage is supported by 24 G-10 tabs from the middle of the vacuum shell. One of the 300-40 K G-10 tabs is visible and labeled. Inside the 4 K cavity, the 1 K and 100 mK stages distribute the cooling power from the dilution refrigerator to individual optics tubes (see Figure 2.25). Infrared filters on the cryostat are shown at the 300 K, 80 K, and 40 K stages in front of the optics tubes. The optics tubes contain the optical components at  $\leq 4$  K and the detector arrays. The optics tube design is discussed in Section 2.2.6 and its internal structure is displayed in Figure 2.13.

The SO LATR has six temperature stages: 300 K, 80 K, 40 K, 4 K, 1 K, and 100 mK. Its mechanical structure is shown in Figure 2.3. The vacuum shell, cold plates, and radiation shields were manufactured by Dynavac<sup>1</sup>. Window and infrared

<sup>1</sup>Dynavac, <https://www.dynavac.com/>

radiation (IR) blocking filters are installed on the 300 K, 80 K, and 40 K plate to absorb most of the optical loading that enters the cryostat, so that the cryo-coolers are not overloaded, and the detectors are not saturated. The detector arrays and the rest of the cold optical components (including lenses and filters) are packaged in optics tubes at  $\leq 4$  K, which are attached directly to the 4 K cold plate with relatively easy access. Mounting the majority of optical components in the optics path within a single optics tube makes it simpler to precisely control the relative position of the optical components. The detailed design of the optics tube is discussed in Section 2.2.6. The modular design also allows one to easily reconfigure the receiver by swapping out any individual optics tube without impacting the other tubes. The interior of each optics tube provides mechanical and thermal isolation for 4 K, 1 K, and 100 mK components. The 1 K and 100 mK stages are cooled via cold fingers and thermal straps by 1 K and 100 mK thermal Back-up Structures (BUSs). The 1 K and 100 mK thermal BUSs are oxygen-free-high-conductivity (OFHC) copper web structures, which efficiently distribute the cooling power from the dilution refrigerator (DR) to the back of the optics tubes (Figure 2.3 and Figure 2.25).

The LATR design also incorporates 12 large radial feedthroughs penetrating the 300 K, 40 K, and 4 K stages to accommodate the pulse tubes, the dilution refrigerator, and cable feedthroughs. The radial feedthroughs are designed to remain thermally coupled to the relevant heat shield while avoiding light leaks and allowing for differential motion between the heat shields and 300K mounting plate. We also paid attention to ensuring the components could be easily installed and removed in keeping with the modular design and future upgrade potential of the 13 optics tube configuration.

### 2.2.1 LATR G-10 Tab Design

The LATR cryogenic stages weigh more than one metric ton. Mechanically supporting this mass with the required stability and optical alignment while minimizing the thermal conductance is a significant challenge. To solve this, we use thin-walled glass epoxy laminate (G-10CR) to mechanically support the 80 K, 40 K, and 4 K stages. Throughout this thesis, G-10 exclusively refers to G-10CR. This design draws on the legacies of both AdvACT [80] and SPIDER [34]. AdvACT used a similar cylindrical G-10 design to mechanically support the 40 K and 4 K stages. However, for the LATR, the diameter of such a cylinder would be nearly 2.4 m. When cooled from 300 K to 40 K, the diameter of such a structure would contract by  $\sim 2.5$  cm, resulting in an unacceptable radial stress on the G-10, and significantly weakening the structure. Inspired by SPIDER, we break up the cylinders by using individual G-10 tabs to support each cryogenic stage. All the G-10 tabs were precisely fabricated at the University of Pennsylvania with assembly jigs. This enabled the precise positioning of each cryogenic stage. As detailed in Table 2.2, the 80 K stage is supported by 12 G-10 tabs from the front of the vacuum shell; the 40 K stage is supported by 24 G-10 tabs from the middle of the vacuum shell; and the 4 K (and colder) stage is supported by another 24 G-10 tabs from the 40 K stage. The 300-40 K G-10 tabs can be seen in Figure 2.3.

The tabs consist of two ‘feet’ connected by a flat sheet of G-10, glued together in a precision jig using Armstrong A-12 epoxy. An example of such tab is shown in Figure 2.4. The tabs can flex radially, allowing them to accommodate the high differential thermal contraction between the cold stages and the vacuum shell during

Stage	Width (mm)	Length (mm)	Number of Tabs	Armstrong A-12 Glue area (cm <sup>2</sup> )
300-80 K	140	180	12	29
300-40 K	160	150	24	36
40-4 K	150	195	24	33

Table 2.2: The geometry and number of tabs. All tabs are 2.4 mm thick with different width and length. The G-10 meets NIST G-10 CR process specification and conforms to MIL-I-247682 Type GEE/CR.

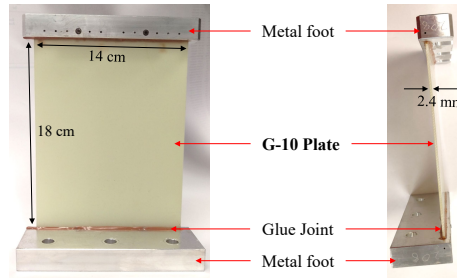


Figure 2.4: An example of 300-80 K G-10 tab is shown from two perspectives. Two aluminum ‘feet’ are glued to G10 plate as mechanical interfaces. Armstrong A-12 was chosen as the glue considering its mechanical and cryogenic performance. Each G-10 tab is serialized as shown in the side-view photo on the right.

cooling. Extensive finite element analysis (FEA) was performed to simulate the structural strength of the G-10 tabs [63], which determined that the factor of safety for the structural components of the tabs is  $> 8$ , excluding the effects of bonding the G-10 tab to the aluminum foot. A pull test of an assembled tab was performed to determine the strength of the glue bond; it failed via de-adhesion from the aluminum surface at 21 kN, implying a glue adhesive strength of 590 MPa. While this force was lower than predicted from the manufacturer listed bond strength, the resulting FoS of 6 still satisfies our requirements. The G-10 was supplied by Professional Plastics.<sup>2</sup>

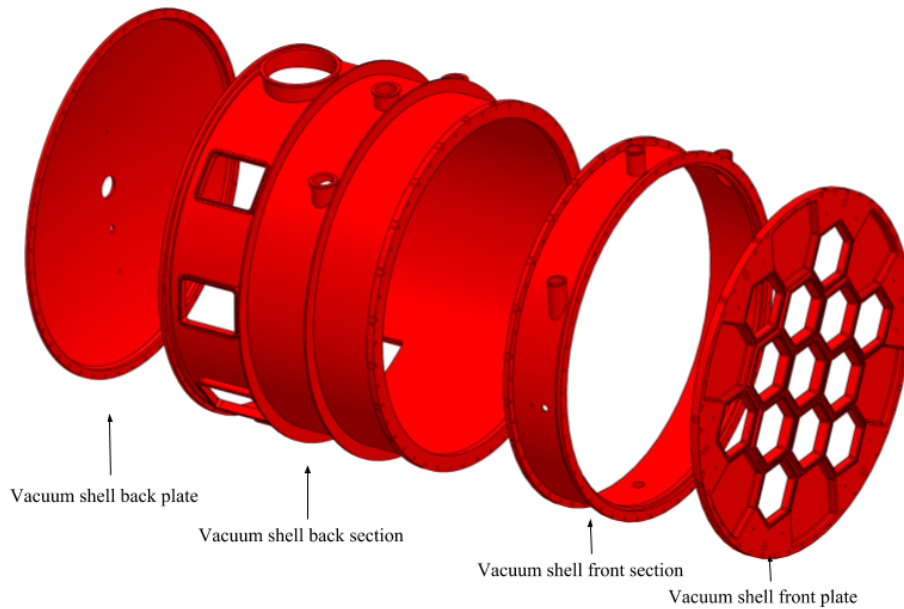


Figure 2.5: Exploded view showing the four major components of the vacuum shell. For scale, the assembled vacuum shell is 2.4 m long and 2.4 m in diameter. The front plate is reinforced where stress concentration is high, and weight-relieved where stress concentration is low. The front section shell is a 1.3 cm thick cylinder and the back section shell is a 0.6 cm thick cylinder. Two aluminum ribs are welded to the back section cylinder for additional strength. They are designed to be as weight efficient as possible to keep the cryostat within the total mass limit.

### 2.2.2 300 K Stage (Vacuum Shell)

The vacuum shell of the cryostat needs to withstand the atmospheric pressure since we need to reach a vacuum of at least  $10^{-7}$  torr to minimize thermal conduction between stages. The model of the vacuum shell is shown in Figure. 2.5. The 300 K vacuum shell consists of the front plate, the front shell, the back shell, and the back plate; all constructed of aluminum 6061-T6. The size of the cryostat was chosen to be 2.4 m in diameter to accommodate 13 optics tubes and allow for mechanical supports and thermal shielding.

---

<sup>2</sup>Professional Plastics, <https://www.professionalplastics.com/>

The front plate is a 6 cm thick flat plate with 13 densely packed hexagonal window cutouts to allow for maximum illumination of the detector arrays. Optimizing the front plate was one of the most challenging aspects of the LATR design. Optical and sensitivity requirements warrant maximizing open apertures via closely spaced windows. However, removing more material drives the plate to be thicker, which eventually leads to a conflict between the diverging optical beam and the window spacing. Ultimately, the optics tube spacing was primarily driven by the optimization of the front plate design. The hexagonal windows are tapered to match the diverging beam, leaving as much material as possible to reduce the bending and stress on the front plate. Alternative designs and materials were considered, including machining the plate with a domed shape, either bowing in or out. These were rejected due to the complexity and expense of machining them. Additionally, doming the front plate would stagger the windows axially; this would require all further optical elements to be axially staggered to maintain consistency of the optical chain, greatly complicating the design of the cold optics.

A key mechanical challenge for the vacuum shell was managing the level of bending of the comparatively narrow struts around the 13 hexagonal optic tube openings in the front plate under atmospheric pressure. After consultation with an external engineering firm (PVEng<sup>3</sup>), we addressed this concern by increasing the thickness of the front vacuum shell wall and adding stiffening ribs. Overall the minimum factor of safety (FoS) on the vacuum shell is  $> 3$  at 1 atmosphere of pressure, with the lowest FoS on the front plate. Figure 2.6 shows the expected deformation of the final front plate design from FEA, magnified by a factor of ten. These results are for sea level

---

<sup>3</sup>Pressure Vessel Engineering Limited, <https://www.pveng.com/>



atmospheric pressure. While the pressure at the high-elevation site in Chile is only  $\sim 0.5$  bar, the integration testing of the LATR is being done at lower elevations.

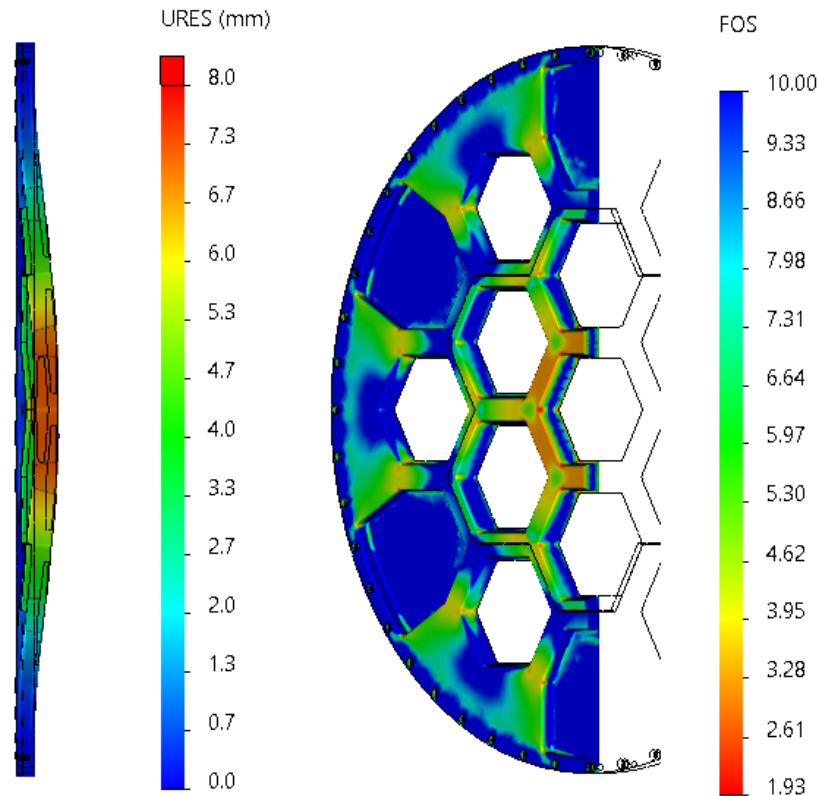


Figure 2.6: Left: Resultant displacement (URES) plot showing the bowing of the front plate under 1 atmosphere of pressure. The displacement scale is exaggerated 10 times. Right: FoS plot for the vacuum shell under 1 atmospheric pressure at sea-level. The minimum FoS is in the corners of the center window and is due to unphysical stress concentrations from the finite size of the mesh. The actual FoS on the surface of the vessel is  $> 3$ .

Sensitivity requirements drive the windows to be as thin as possible, which has to be balanced against the need to withstand atmospheric pressure. The LATR utilizes  $1/8''$  thick hexagonal windows made of anti-reflection (AR) coated ultra-high molecular weight polyethylene. Each hexagonal window has its own O-ring. A single window has been vacuum tested under atmospheric pressure for more than 36 months

with no indication of reduced structural performance or leakage. The LATR has been tested with seven 1/8" thick windows. However, the majority of the in-lab (sea-level) testing has been performed with 1/4" thick windows to remove the risk of a catastrophic failure event that might damage other parts of the receiver. One double-sided IR blocking filter fabricated by Cardiff University ([6]; section 7) is mounted on the back of the front plate behind each window to reduce the optical loading entering the cryostat. The cold optics design is discussed in detail in Section 2.2.6.

### 2.2.3 80 K Stage

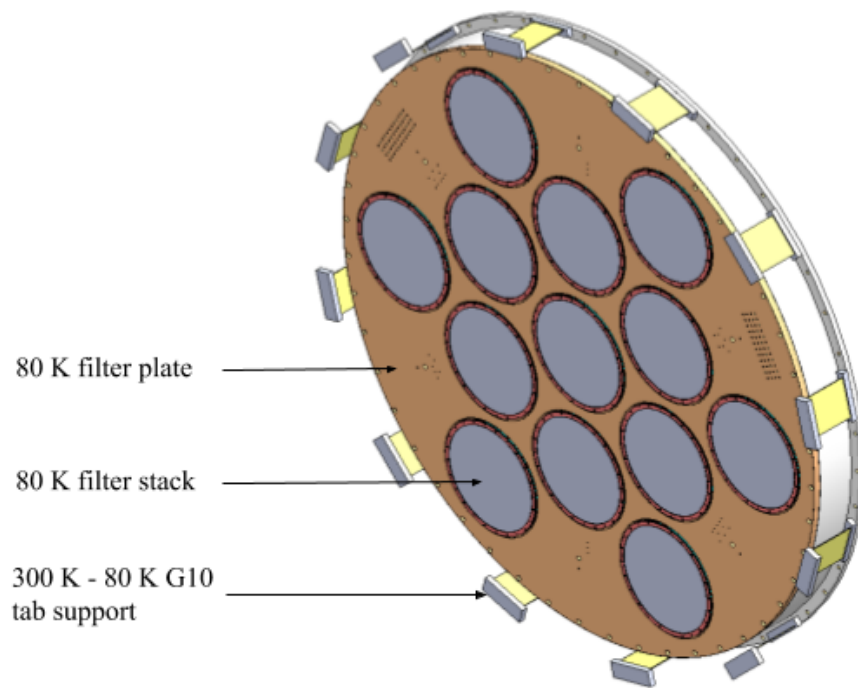


Figure 2.7: Assembled model of the 80 K stage. For scale the 80 K plate is 2.3 m in diameter. The combination of the IR blocking filter and alumina filter in the 80 K filter stack will absorb most of the out-of-band optical power so that the 40 K stage is not overwhelmed with optical loading. The 80 K stage will absorb an estimated total of 100 W from all loadings combined.

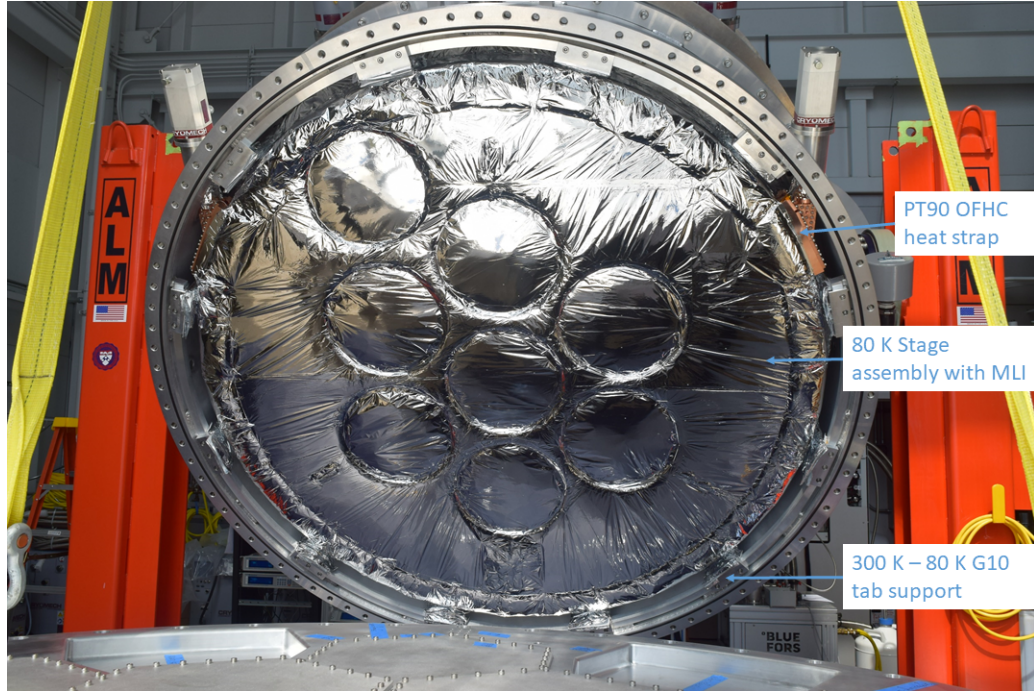


Figure 2.8: This picture shows the 80 K stage installed in the cryostat. The outside of the stage is covered with 30 layers of MLI.

The 80 K stage (as shown in Figure. 2.7) consists of a 2.1 m diameter, 2.54 cm thick circular plate made of aluminum 1100-H14 and a short 80 K shield made of aluminum 6061-T6. It is designed to intercept most of the optical loading entering the cryostat, reducing the load on the 40 K stage. The 1100 series aluminum was used due to its higher thermal conductivity. The 80 K plate contains one double-sided IR blocking filter and one AR coated alumina filter for each optics tube [32]. The alumina filters act as an IR absorber as well as a prism to bend the off-axis beams back parallel to the long axis of the cryostat [22]. The outside of the 80 K stage is covered with 30 layers of multi-layer insulation (MLI)<sup>4</sup> to reduce the blackbody radiative load coming from the 300 K shell, as shown in Figure 2.8. The structural support of the 80 K stage is located at the front of the vacuum shell. Thus, the entire

<sup>4</sup>RUAG Holding AG, <https://www.ruag.com/en/>

80 K stage can be installed or taken out independently from the rest of the cryostat.

## 2.2.4 40 K Stage

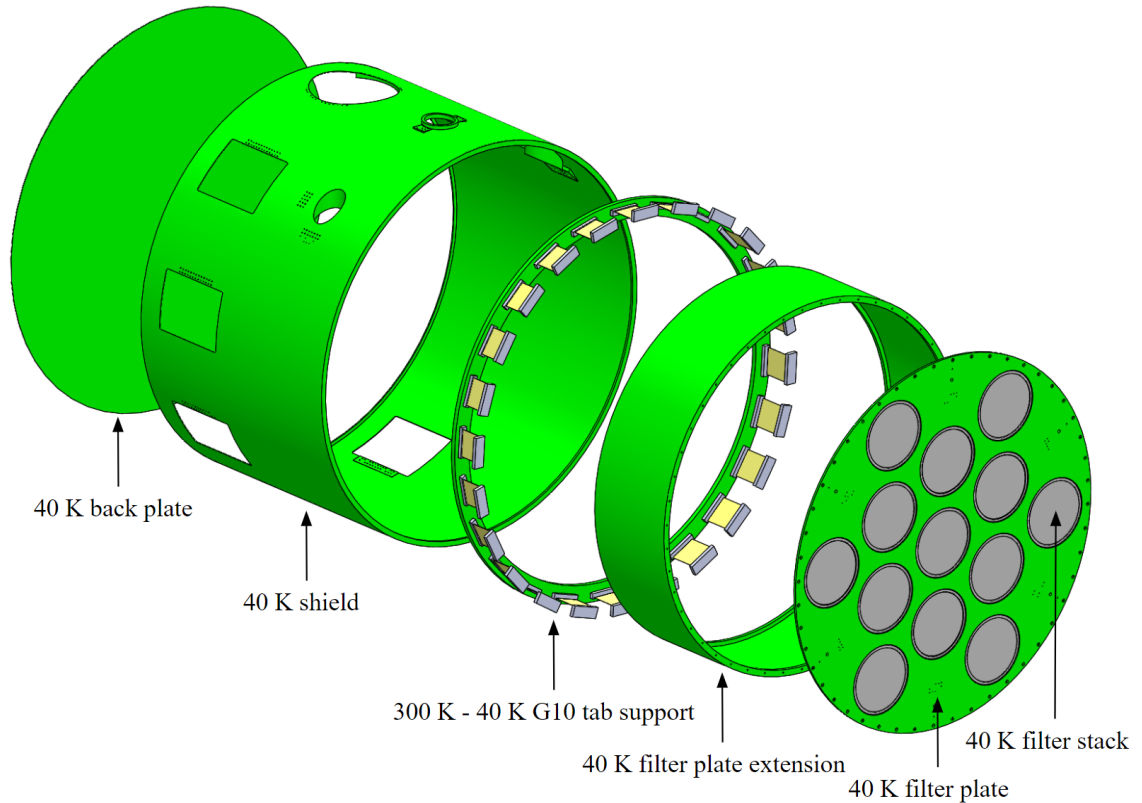


Figure 2.9: The exploded view showing the 40 K stage assembly. For scale, the 40 K stage assembly is 2.1 m in diameter and 2.0 m long. As shown, the light enters from the right and goes through the IR blocking filters mounted on the 40 K filter plate. The entirety of the 40 K stage will be covered by multi-layer insulation (not shown in the model).

The 40 K stage consists of a 2.1 m diameter circular plate, a 40 K radiation shield, a 40 K filter extension tube, and a thin 40 K radiation back plate, as shown in Figure. 2.9. The two cylinders are made of 1100 aluminum and the plates are made of 6061-T6 aluminum. Rather than being suspended from the 80 K stage, it is instead suspended directly from the 300 K vacuum shell back section. This approach greatly reduces



Figure 2.10: This picture shows the 40 K shield assembly sitting on dollies right before getting installed onto the vacuum shell. The 40 K shield is wrapped with 30 layers of MLI. The G-10 tabs attached to the 40 K shield is wrapped with 20 layers of MLI. The black paint inside the 40 K shield is also visible through the radial cutouts.

the structural stress on the 80 K stage G10 tabs, simplifies the assembly process, and adds little conductive load to the 40 K stage compared to the cooling capacity available [63]. Another double-sided IR blocking filter will be mounted on the 40 K filter plate to further reduce the IR power to milliwatt level on lower temperature stages (per optics tube). We covered the entirety of the 40 K assembly with 30 layers of MLI and wrapped each of the G-10 tabs in 20 layers to reduce 300 K radiation loading, as shown in Figure 2.10. The interior of the 40 K shield is painted with Aeroglaze<sup>®</sup> Z306 black paint to absorb stray radiation from 300 K. To vent the inside

of the 40 K cavity, evacuation blocks mounted on the back lid of the 40 K shell were designed to allow air to escape without adding an easy path for light leaks. This also prevents the fragile filters from bursting due to differential pressure.

### 2.2.5 4 K Stage

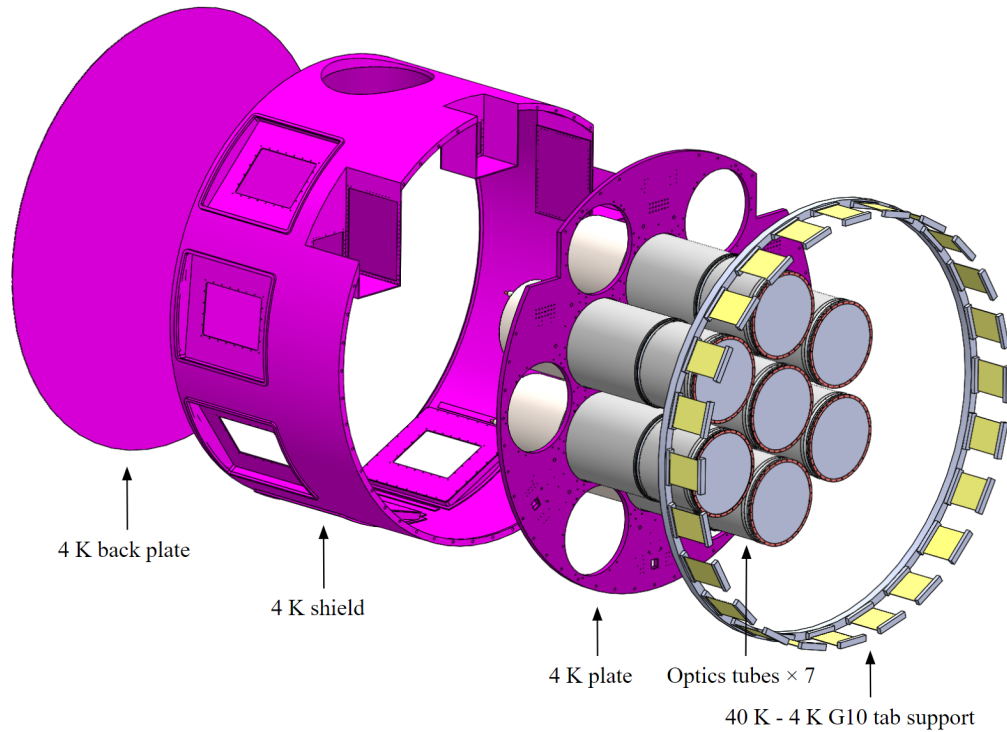


Figure 2.11: An exploded view showing the 4K stage assembly. For scale the 4K plate is 2.1 m in diameter. The optics tubes are mounted on the 4K plate and thus thermally coupled to the 4K stage.

The 4K stage consists of a 2.1 m diameter, 2.5 cm thick circular plate, a 4K radiation shield and a thin 4K back plate, all fabricated from 6061 aluminum, as shown in Figure. 2.11. Similar to the 80K and 40K stages, the 4K stage assembly is also supported by G10 tabs. The main 4K plate is significantly thicker than the plates for the 40K or 80K stages since this structure supports the optics tubes

(Section 2.2.6), the most vital components of the cryostat. The 4 K radiation shield is designed to have recesses for pulse tube refrigerator attachments without penetrating the 4 K cavity, allowing for significant thermal strapping area while minimizing the chance of light leaks into the 4 K cavity, where the 1 K and the 100 mK components reside. The outside of the 4 K shield is wrapped with 20 layers of MLI, and the interior of the 4 K shield is painted with Aeroglaze<sup>®</sup> Z306 black paint, as shown in Figure 2.12.



Figure 2.12: This picture shows the 4 K shield right before it is installed in the cryostat. Although the radiative thermal loading from 40 K to 4 K is low, we still wrapped the 4 K shield with 20 layers of MLI, in case excess amount of stray light from 300 K hits the 4 K shield. The black paint on the interior wall of the 4 K shield is also visible in this picture.

## 2.2.6 Optics Tubes

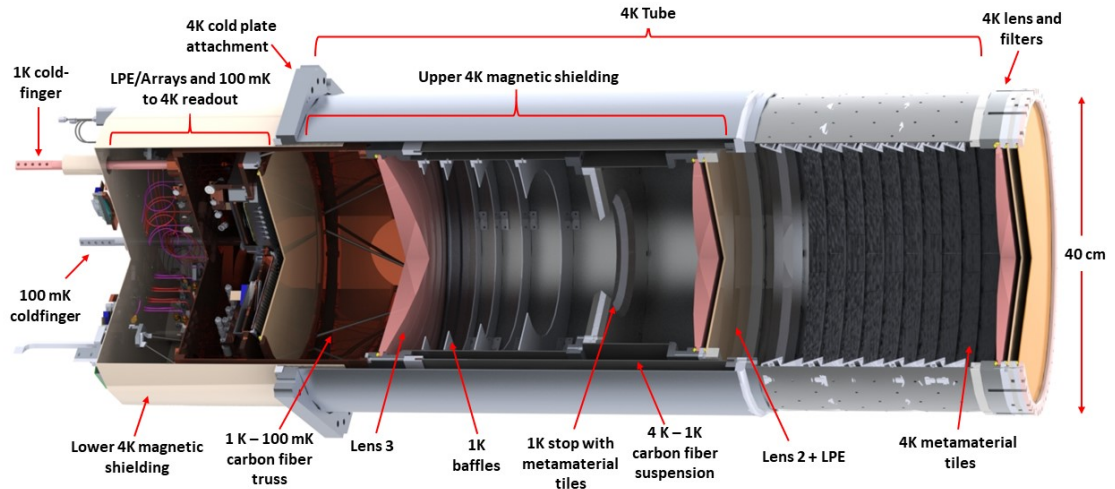


Figure 2.13: A rendering showing the major parts of one optics tube. Light rays enter from the right through the 40 cm diameter 4 K lens and filters. After the metamaterial tile section, light rays are refracted by Lens 2. Then the incoming light rays are truncated by the metamaterial tile covered Lyot stop before going in to the ring baffle section. Finally, the light rays are focused by Lens 3 before reaching the detector arrays. The detector arrays and their supporting components are presented in Figure 2.14 with more details.

The cryostat can accommodate a total of 13 optical chains, each with a dedicated set of detectors (see Table 2.1). Each optical chain consists of elements that are mounted on either the cryostat cold plates (300 K, 80 K, and 40 K) or, for the colder stages, in a large, self-contained optics tube (Figure 2.13) that has components at 4 K, 1 K, and 100 mK. Each tube is roughly 40 cm in diameter and 130 cm long and is designed to be removable as a single unit from the rear of the cryostat. As detailed in Table 2.1, the initial seven optics tubes include 1 in the LF bands, 4 in the MF bands, and 2 in the UHF bands. A cross-section of an MF tube is shown in Figure 2.13. The field of view for each optics tube is  $1.3^\circ$  in diameter, which is partially filled by the three detector wafers.



## Cold Optics

We selected a refractive cold optics design for its compactness. Inside each optics tube, three silicon lenses re-image the telescope focal plane onto a set of three hexagonal detector arrays [22]. Silicon is selected as the lens material due to its low loss and the outstanding performance of developed metamaterial AR coatings [32; 18; 19]. The upper edge of each frequency channel is set by a set of low-pass edge (LPE) filters, which use a capacitive mesh design [6] to set a range of cut-off frequencies (e.g.,  $12.5 \text{ cm}^{-1}$  to  $6.2 \text{ cm}^{-1}$  for MF). The cut-offs are also chosen to suppress out-of-band leaks from other filters. The LPE filters are complemented by IR blocking filters at warmer stages [81] to reduce the thermal loads on the colder stages. The designs implemented for the SO incorporate two metal mesh patterns printed onto each face of a polypropylene substrate to form double-sided IR blockers. The capacitive square copper patterns have a  $15 \mu\text{m}$  period; the polypropylene substrate is thin ( $4 \mu\text{m}$ ) and absorbs very little of the in-band radiation. Thus each device acts as a basic low-pass filter, which is optimized for high reflectivity of near-IR radiation with virtually no attenuation of the science bands. Successive filters are placed between 300 K and 4 K to reflect the IR radiation emitted by these stages and to protect the thermal environment at the 1 K and 0.1 K stages. Combined, the optical elements consist of: a 3.1 mm thick AR coated window and an IR blocking filter at 300 K; an IR blocking filter and alumina absorbing filter at 80 K; an IR blocking filter at 40 K; an IR blocking filter, LPE filter, and the first lens at 4 K; an LPE filter, the second lens, the Lyot stop, and third lens at 1 K; and the final LPE filter and detector arrays at 100 mK. See Figure 2.13 for the relative locations of optical elements inside the optics

tube.

In this optics tube design, it is worth highlighting part of the 80K design that makes it possible. The alumina filter at 80K is wedge-shaped (except for the central optics tube) so that it acts as a prism in addition to acting as an IR blocking filter. This prism allows all optics tubes to be coaxial with the cryostat, which allows for a much more efficient use of space and greatly simplifies the installation/removal of the optics tubes. Each alumina filter has a notch machined into it for setting the proper angular orientation. We are pursuing several parallel AR coating techniques for this element to optimize cost versus performance. The baseline is to use metamaterial coatings on alumina [32].

The close-packed optics tubes prevent the use of traditional light baffling between 4 K filter and Lens 2, since there is little space between the walls of the upper (4 K) optics tube and the incoming beam. Since stray light is a major concern, significant effort was dedicated toward fabricating novel, low-profile metamaterial microwave absorbers [87; 35]. The goal was a design that had maximum absorptivity and minimum reflection, was capable of cooling down to cryogenic temperatures while maintaining mechanical integrity, and was relatively easy to install. The solution was injection-molded, carbon-loaded plastic tiles that create a gradient index AR coating [87]. About 240 holes were laser cut into the upper tube, allowing each tile to be screwed into place. A flat version of the tile was designed to attach to both sides of the 1 K Lyot stop. The region in between the stop and Lens 3 was baffled with standard ring baffles covered with a mixture of Stycast 2850 FT, coarse carbon powder, and fine carbon powder, because it has more radial clearance and is less critical for stray light. The 1 K radiation shield surrounding the detector arrays was

blackened in the same manner.

## Mechanical Support Structures

The windows and all filters are mounted using aluminum clamps (except for the 100 mK LPE filter, which uses a copper clamp). The LPE filter clamps are axially spring-loaded to minimize the possibility of delamination due to the shear forces involved during large (radial) differential thermal contraction ( $\sim 6$  mm) between the aluminum mounts and the polypropylene filters. The spring is a commercial spiral beryllium copper structure.<sup>5</sup> The lens mounts contain both an axial spring and a radial spring. The axial spring ensures firm thermal contact between the lens and mount without risking cracking the brittle silicon. The radial spring ensures the lens is centered at operating temperature by pushing the lens against two opposing hard points.

Each optics tube consists of a large 4 K cylindrical structure containing the 1 K and 100 mK components. A 4 K A4K magnetic shield lines the outside wall of the 4 K tube, extending from the location of the second lens to the rear end of the optics tube. The 4 K and 1 K tubular sections were fabricated from aluminum 1100-H14 sheet to reduce thermal gradients along their lengths, which resulted in a 2 K temperature gradient reduction according to the simulation. The sheets were welded to Al 6061 O-temper flanges. A final machining step is done to attain the assembly specifications. The 1 K components are supported from the 4 K tube by a custom-made carbon fiber tube from Clearwater Composites and Van Dijk<sup>6</sup>. A 1 K radiation shield is

---

<sup>5</sup>SPIRA, <http://www.spira-emi.com/>

<sup>6</sup>Van Dijk Pultrusion Products (DPP BV), <https://www.dpp-pultrusion.com/en/the-company/>

installed around the 100 mK components. Because the shield serves the dual purpose of supporting and cooling readout components, it was fabricated out of OFHC copper. A carbon fiber truss attaches to the rear of the 1 K section and supports all 100 mK components. Mechanical loading tests verified that the carbon fiber structures were able to support at least five times the expected operating loads. Simulations show the lowest resonant frequency of the carbon fiber structure is above 50 Hz, which lies above the 30 Hz requirement based on our past experience with the ACT receiver.

The 100 mK and 1 K cold fingers and readout support structures were all fabricated out of OFHC. The components were also gold plated to prevent future oxidation, which would lead to reduced thermal performance. The focal plane base plates, which support the detector arrays and 100 mK readout components, were also fabricated out of OFHC and gold plated.

## **Detector Arrays and Readout**

The SO uses two types of dual-polarization dual-frequency TES bolometer arrays. For MF and UHF frequencies, the TES bolometers are coupled to the optics with orthomode transducers feeding monolithic feedhorn arrays, based on their well-tested performance in the Advanced ACT receiver [15; 40; 26]. For LF frequencies, sinuous antennas with lenslets couple the bolometers, based on the design successfully used for POLARBEAR [78] and the South Pole Telescope [64; 70]. For both architectures, each TES array is hexagon-shaped and fabricated from Silicon wafers 150 mm in diameter. A detector array, including the light-coupling mechanism, TES bolometers, 100 mK readout architecture, and associated magnetic shielding are packaged into a single universal focal-plane module (UFM) [56]. There are three UFM per optics

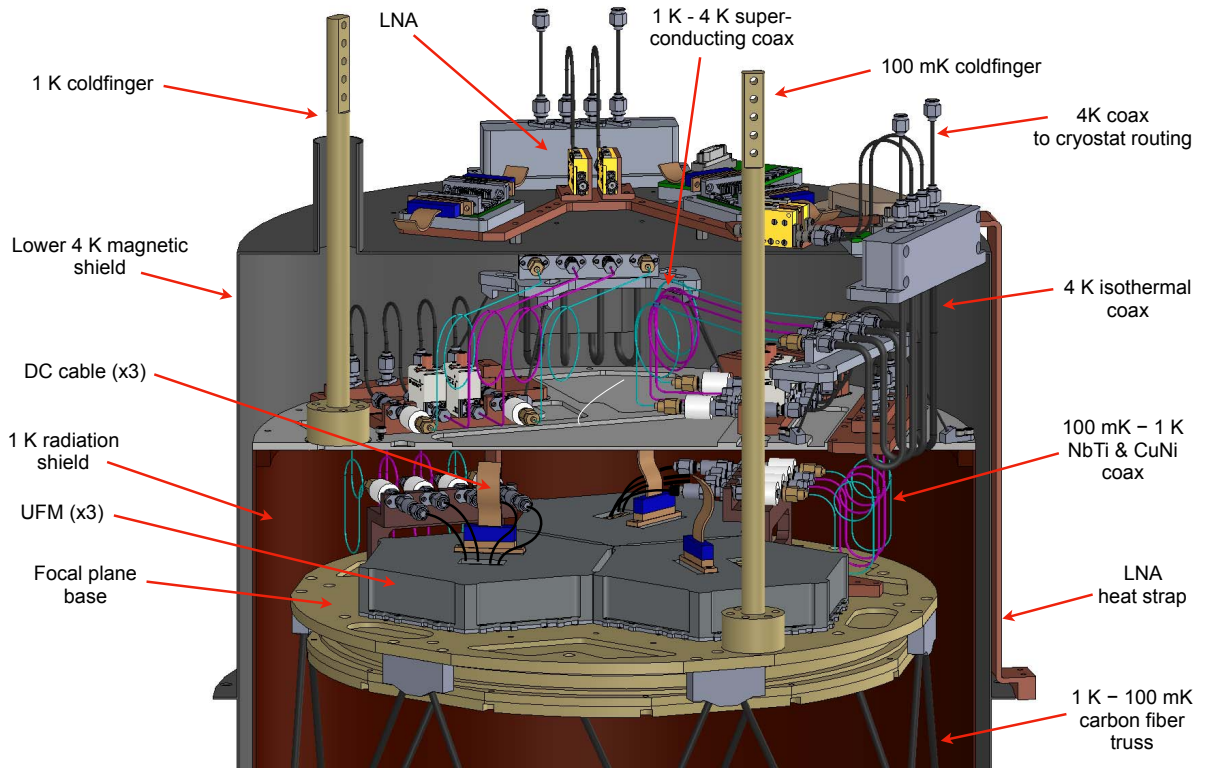


Figure 2.14: Optics tube mechanical and readout components on the 4 K, 1 K, and 100 mK stages. This design shows the cable setup for a multiplexing factor of 1,000, where each UFM is read out by two pairs of RF lines. In addition, one DC ribbon cable per UFM provides the detector biases and flux ramps.

tube. The UHF and MF optics tubes contain a total of 1,290 pixels that couple to 5,160 optically active TESes. An LF tube has 111 pixels that couple to 444 optically active TESes. Details of the UFM design are described in Li et al. [50].

Due to space limitations, one of the most significant challenges of the optics tube design was the routing of the readout cabling from the three UFM at 100 mK to the 4 K components on the back of the optics tube magnetic shielding (Figure 2.14). The SO uses microwave multiplexing technology to read the detectors out [23]. For the target multiplexing factor of 1,000, each optics tube needs 12 radio frequency (RF)

coaxial cables to read out  $\sim 5000$  detectors and 3 direct current (DC) ribbon cables for detector/amplifier biases and flux ramps [54].

To simplify the routing between isothermal components, hand-formable 3.58 mm copper coaxial cables were used.<sup>7</sup> For connecting optics tubes readout components at different temperatures (4 K – 1 K and 1 K – 100 mK), low thermal conductivity semi-rigid cables were employed. CuproNickel (CuNi) cables with 0.86 mm diameter are used for  $\text{RF}_{\text{in}}$  to control the attenuation at each step to a colder temperature stage, as well as limit thermal loading. For the  $\text{RF}_{\text{out}}$  lines, superconducting 1.19 mm Niobium Titanium (NbTi) cables maximize signal-to-noise, yet still have good thermal isolation properties. Both types of semi-rigid cables are bent into loops for strain relief. DC blocks are implemented for additional electrical/thermal isolation. Attenuators on the input lines guarantee that the correct power level is delivered to the resonators, the multiplexing components in the array. Each 4 K RF output line has a LNA mounted on the back of the magnetic shield. To reduce temperature rise due to the power generated by the LNAs ( $\sim 5$  mW each), the LNAs are mounted on a common copper plate that has a copper strap routed down the side of each tube to the 4 K plate. Additional LNAs are installed at 40 K stage to constitute a two-stage cold LNA system. For more details on the RF component chain, see [72].

## Magnetic Shielding

A layer of Cryoperm A4K manufactured by Amuneal<sup>8</sup> covers the back of the optics tube to act as a 4 K magnetic shield, as shown in Figure 2.14. The A4K magnetic shield extends through the optics tube to the Lens 2 mounting location shown in

---

<sup>7</sup>Mini-Circuits <https://www.minicircuits.com/>

<sup>8</sup>Amuneal Manufacturing Corp, <https://www.amuneal.com/>

Figure 2.13. A study has been conducted on the possible UFM magnetic shielding strategies for the microwave SQUID multiplexing readout system [82]. As a result of this study, and in order to provide a higher shielding factor for the detector and readout components, we are also investigating plating the optics tube 1 K radiation shield with a type-I superconductor. The original design calls for plating the interior of the 1 K copper optics tube shield with Tin. But due to concern with Tin pest from such plating, we are investigating an alternative to plate the copper shield with lead-tin alloy instead.

### 2.2.7 1K and 100mK Stages

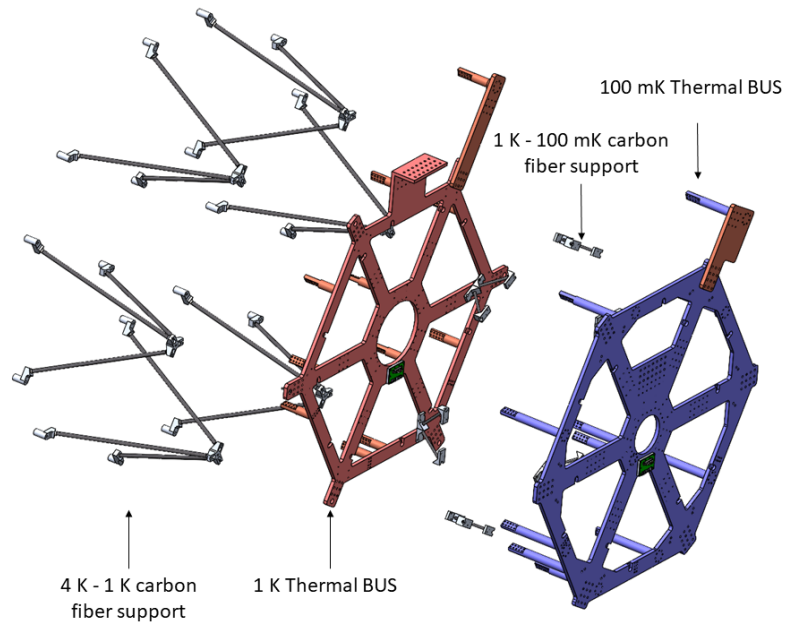


Figure 2.15: An exploded view of the thermal BUS. The thermal BUSes are made of OFHC copper. A set of six carbon fiber tripods support the 1 K thermal BUS from the 4 K plate, and a set of six carbon fiber V-shaped supports suspend the 100 mK thermal BUS from the 1 K thermal BUS. The cold fingers on the 1 K BUS were welded on, while the cold fingers on the 100 mK BUS were bolted on.

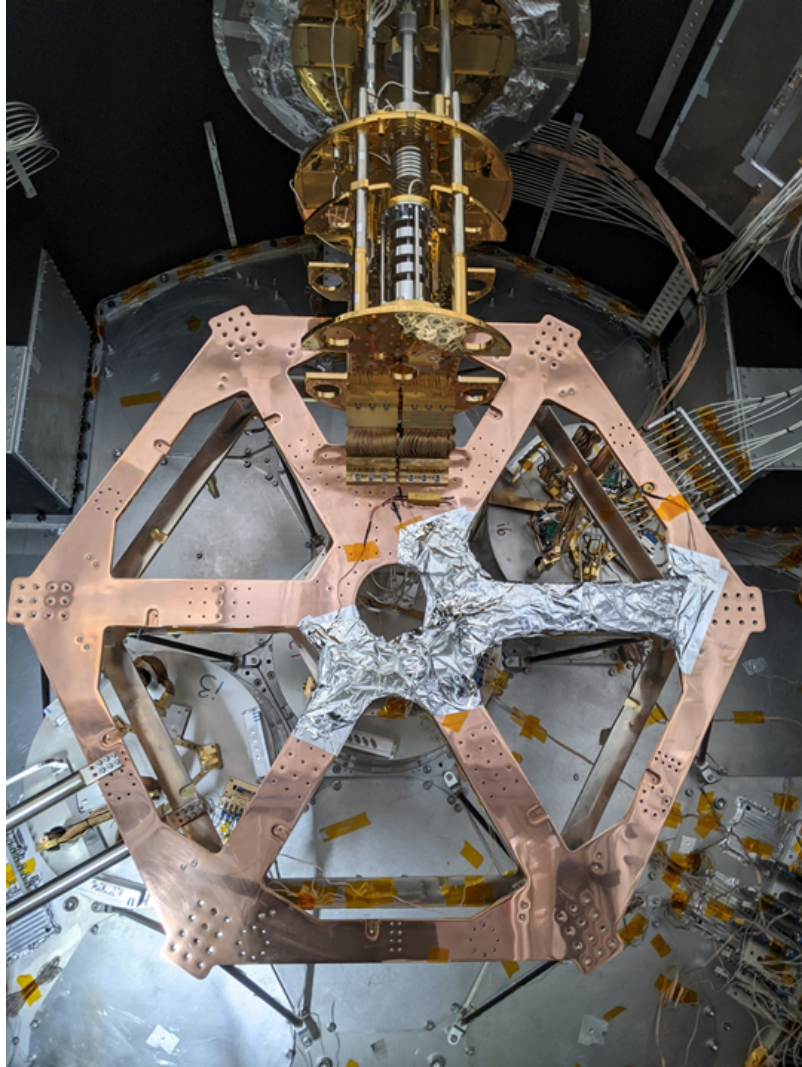


Figure 2.16: A picture of the installed thermal BUS. The 100 mK BUS is closer, and the 1 K BUS is visible in the back. Part of the 100 mK BUS where thermometer lines run is covered with MLI tape to achieve more accurate temperature reading.



To increase the sensitivity of the TES detectors, all detector components and readout chips are cooled to below 100 mK [55] with a Model LD400 DR manufactured by Bluefors.<sup>9</sup> To reduce thermal gradients on the 1 K and 100 mK stages, we implement two thermal BUSES comprised of two wheel-like structures made of OFHC copper (Figure 2.15 and Figure 2.16). The original design has both thermal BUSES gold plated for lower emissivity and smaller contact resistance, but after contacting a few gold plating companies, we decide that gold plating a part this size would be too costly. As such, we simply asked the machine shop to polish the surface of the finished OFHC BUSES. From the thermal BUS cold finger, individual gold-plated copper straps, manufactured by TAI,<sup>10</sup> extend down to attach to the 1 K and 100 mK cold fingers inside each optics tube. The original thought was to weld these cold fingers to the thermal bus to reduce a bolted interface. However, due to the size of the thermal BUS, the welding would require too much heat that it would introduce warpage to the BUS plate. After a few iterations of prototypes, we decide to switch to bolted cold fingers to simplify the machining process. During testing, we found that properly bolted cold finger introduce negligible contact resistance compared to the welded version. The 1 K thermal BUS is supported from the 4 K plate with carbon fiber tripods, while the 100 mK thermal BUS is supported from the 1 K thermal BUS via carbon fiber trusses. We chose the twill-ply carbon fiber tubing for these legs as we find that the unidirectional-ply carbon fiber has a tendency to splinter. The carbon fiber used for these applications was sourced from Clearwater Composites<sup>11</sup>.

Thermal FEA shows that the temperature gradient across both thermal BUSES

---

<sup>9</sup>Bluefors Oy, <https://www.bluefors.com/>

<sup>10</sup>Technology Applications, Inc. (TAI), <https://www.techapps.com/>

<sup>11</sup>Clearwater Composites, <https://www.clearwatercomposites.com/>

should be  $\sim 5$  mK, which satisfies our gradient requirements of  $\lesssim 10$  mK. During cryogenic validation (discussed in detail in Section 3.2), the actual temperature gradient measured on the 100 mK BUS is  $\lesssim 10$  mK, higher than the FEA value but still below the requirement. Based on calculated loading from conduction and measured total loading the inferred radiative load on the 100 mK thermal BUS is  $\ll 1 \mu\text{W}$ .

## 2.3 LATR Cryogenic Design

### 2.3.1 Cryo-cooler Integration

In order to reach the desired detector sensitivity, the LATR cryogenic system must maintain all 62,000 detectors at a stable temperature below 100 mK while minimizing the in-band optical loading onto the detectors. The system must also be mechanically rigid, with required tolerances on optical alignment of the elements that are fractions of a millimeter over the  $2.4 \text{ m} \times 2.6 \text{ m}$  scale of the system. Given the LATR needs to cool 1200 kg of material to 4 K and 200 kg to below 100 mK, it is challenging to design the cryogenic system to cool down the internal structures effectively. The 80 K stage uses two PT90 pulse tubes while the 40 K and 4 K stages are cooled by two PT420 pulse tubes supplied by Cryomech<sup>12</sup>. We also considered Gifford-McMahon (GM) coolers: while they can provide higher cooling capacity at warmer temperatures, specifically 80 K, they cannot reach our required 4 K base temperature, and they also produce far more vibrations than pulse tube coolers, potentially heating the coldest stages via microphonics. Our 1 K and 100 mK stages are cooled with a  $^3\text{He}$ - $^4\text{He}$  DR

---

<sup>12</sup>Cryomech, <https://www.cryomech.com>

manufactured by Bluefors, which is backed by a Cryomech PT420 pulse tube cooler. A DR provides the ability to cool our detector arrays to 100 mK, with approximately 500  $\mu$ W of power available at that temperature. It also provides continuous cooling power, without the need to cycle the system. As a design contingency, the LATR can accommodate an additional PT90 and PT420 pulse tube cooler for the 80 K and 40 K/4 K stages respectively. However, these additional coolers are not required based on our cryogenic validation tests.

Managing and minimizing the thermal loads to meet the cryogenic performance specifications drives almost every aspect of the thermal design. The base temperature of the pulse tube is a function of the total thermal load on the system. Thermal load on each stage includes conductive load from supporting structures, radiative load from the warmer stages and incoming light, conductive load from cables, and cryogenic electrical components. Estimates of all of these were included in thermal models, summarized in Table 2.3.

The large 2.4 m  $\times$  2.6 m scale of the receiver poses its own challenges to the cryogenic design. Reaching the target temperatures at the cold head of the pulse tube coolers or DR is a necessary but not sufficient condition. The thermal design must also include sufficient thermal conductivity within each temperature stage to keep the thermal gradient below the required level. For example, the farthest point on the 40 K filter plate is  $\sim$  2 m from the nearest pulse tube with five mechanical joints in the thermal path (Figure 2.3). If the thermal link is weak, a small amount of power can lead to a large temperature gradient along the path, resulting in an elevated optical filter temperature, without substantively affecting the pulse tube base temperature. During our initial cryogenic testing, we found that the 40 K stage

gradient to be too large due to insufficient conductivity from the 40 K shell. As a result, we have to install additional 5N aluminum plates to improve the conductivity. This process involves grinding the black paint off the interior of the 40 K shield, drilling holes through the shield with a stop so that the drill doesn't go through the 30-layer MLI outside the 40 K shield, and install rivet nuts on the thin shell. We then installed 1/4 in and 3/8 in 5N aluminum plate on the curved shell, using the screw to bend the plate so that they conform to the shield curvature. Figure 2.17 shows the drilling process in action. This lesson implies that more attention should be paid on improving the shell conductance if the shells are designed to distribute cooling power.

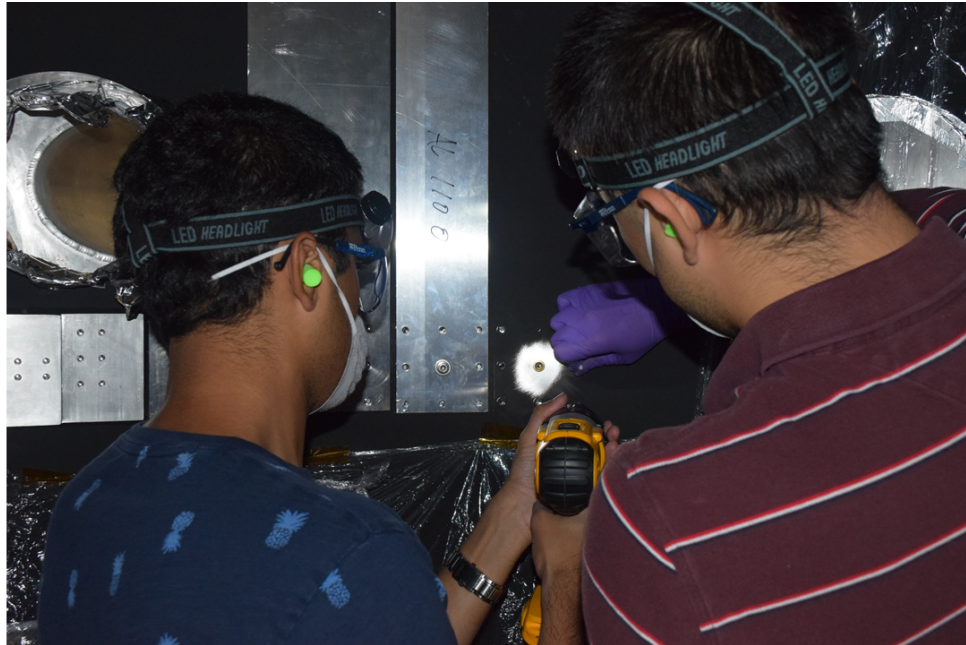


Figure 2.17: The picture shows the process of installing additional 5N aluminum straps on the 40K shield in order to improve the gradient on the 40 K stage.

In most cases, the thermal path follows the mechanical structure. However, there are exceptions. For example, 6061 aluminum is used for the mechanical structure of the 4 K cold plate to meet the optical alignment requirements, and supplemented by

the softer but more conductive 1100 aluminum or sometimes 5N aluminum to meet the thermal requirements. In another case, flexible thermal straps connect the coolers and cryogenic stages to transfer heat while allowing for the differential contraction between the two. An example of such combination is shown in Figure 2.18.

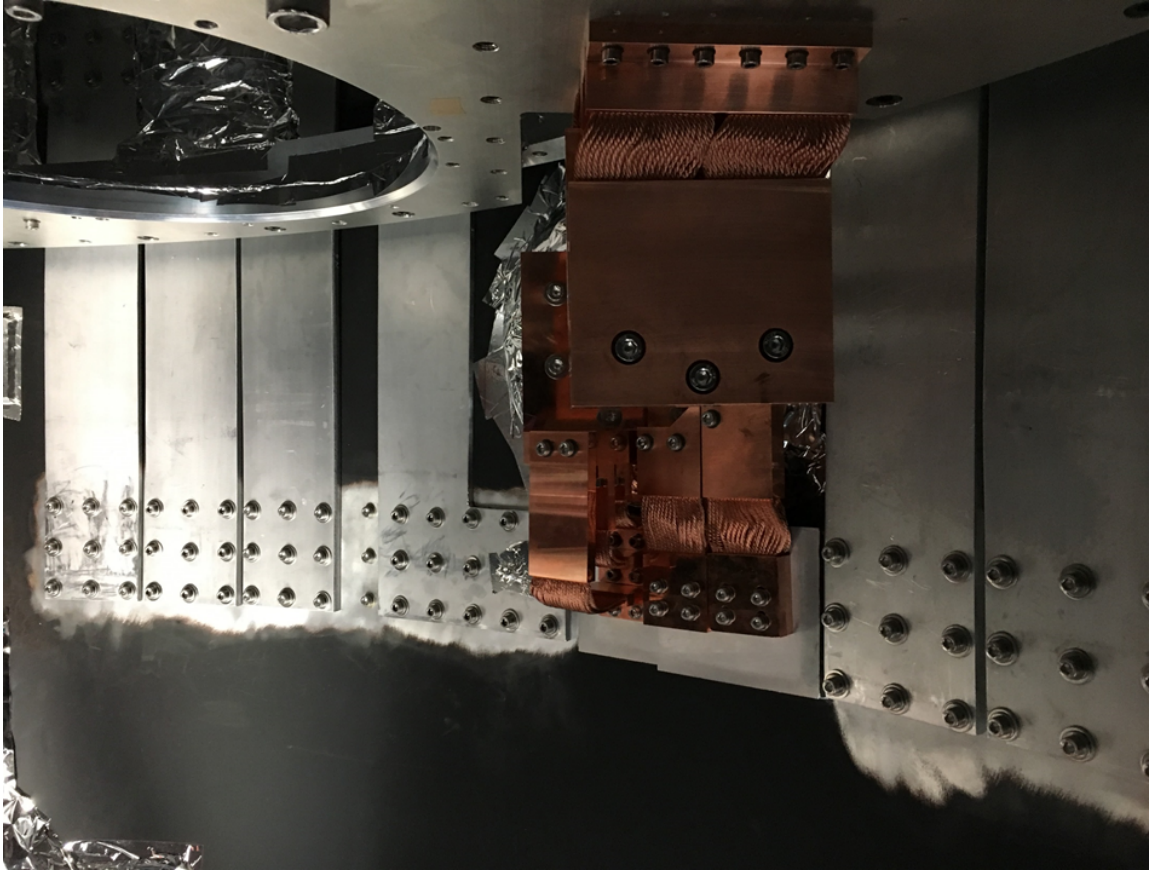


Figure 2.18: A picture showcasing the 40 K and 4 K copper braid straps, and the 5N aluminum installed on the 40 K shield.

Finally, it is important to minimize temperature gradient during cooldown. Based on the mass of the cold structure, bringing the system from 300 K to the target temperature requires removing 350 million Joules of energy from the system. Gradients are important because the pulse tube cooling efficiency is a very steep function of the cold head temperature. The PT420 second stage (4 K cold head) can remove up to

225 W when it is at 300 K, but only 2 W when it is cooled to 4 K. Therefore, the most efficient use of the pulse tube during cooling is achieved when thermal gradients are minimized across the cryostat, while pulse tube cold head temperature is maximized. A large temperature gradient between the cold head and stage means the pulse tube temperature is well below the rest of the stage, and thus the pulse tube can remove less power than it would if the entire system was at the same temperature. For example, if the thermal strap between the PT420 second stage and the body of the cryostat is not conductive enough, even 50 W of heat flow would correspond to a 100 K gradient. In this situation, the pulse tube would be much colder than the 4 K plate, and thus removing power much slower than what it could do if it were at a higher temperature. A model of the material properties as a function of temperature is included in the design to ensure sufficient thermal conduction throughout the relevant parts of the LATR during cooldown. The cooldown predictions are shown in Section 2.3.3, and the measured cooldown times are presented in Section 3.2.

## 2.3.2 Thermal Modeling

### Thermal Conduction Calculation

Thermal modeling included a careful accounting of all sources of loading at each stage. To compute the thermal loading from supports, we first compiled a library of materials and their thermal conductivities at cryogenic temperatures. We obtained measurements from the National Institute for Standards and Technology (NIST) cryogenic material properties database [61; 53] and from Adam Woodcraft's low temperature material database [83]. The total conductive load for a support is the

integrated thermal conductivity between the temperatures on the high and low ends. The conductivity of the cables were computed in the same way, with the conductivity of the coax cables provided by Coax Co.<sup>13</sup>

The thermal conduction due to radiation on surfaces covered in MLI was computed using the Lockheed equation [71]:

$$q_{\text{tot}} = \frac{C_c N^{2.56} T_m}{n} (T_h - T_c) + \frac{C_r \epsilon_0}{n} (T_h^{4.67} - T_c^{4.67}), \quad (2.1)$$

which accounts for both the conductive loading through the layers of the blanket (first term), and the radiative loading between layers of the MLI blanket (second term). In Equation 2.1,  $q_{\text{tot}}$  is the total thermal load on the MLI in unit of  $mW/m^2$ ,  $C_c = 8.95 \times 10^{-5}$  is a numerical constant defining the MLI conductive heat transfer,  $N$  is the MLI layer density in layers per centimeter,  $T_m$  is the mean MLI temperature, taken to be  $T_m = \frac{T_h + T_c}{2}$ ,  $n$  is the number of MLI layers,  $T_h$  is the hot-side temperature in Kelvin,  $T_c$  is the cold-side temperature in Kelvin,  $C_r = 5.39 \times 10^{-7}$  is a numerical constant defining the MLI radiative heat transfer, and  $\epsilon_0 = 0.031$  is the MLI emissivity [47].

## Thermal Optical Simulation

To calculate the thermal loading due to the optical elements inside the LATR, we created a custom Python package to model the thermal performance of all filter elements in a predefined radiative environment. The code estimates the total power emitted and absorbed at each temperature stage by performing a radiative transfer

---

<sup>13</sup>Coax Co., Ltd., <http://www.coax.co.jp/en/>

Stage (K)	Support (W)	Radiative (W)	Optical (W)	Readout Components (W)	Total (W)	Available Power (W)
80	3.2	6.6	51	0.026	61	180
40	9.5	25	0.026	21	56	110
4	0.31	0.20	0.36	1.5	2.4	4.0
1	$2.0 \times 10^{-3}$	$5.5 \times 10^{-6}$	$0.38 \times 10^{-3}$	$0.44 \times 10^{-3}$	$2.8 \times 10^{-3}$	$25 \times 10^{-3}$
0.1	$44 \times 10^{-6}$	$0.41 \times 10^{-6}$	$4.1 \times 10^{-6}$	$18 \times 10^{-6}$	$67 \times 10^{-6}$	$500 \times 10^{-6}$

Table 2.3: Loading estimates for each temperature stage of the LATR split by source. The provided load estimates are for 13 optics tubes. The cooling power at 80 K is supplied by two PT90 coolers, the power at 40 K and 4 K is supplied by two PT420 coolers, the power at 1 K by the DR still stage, and the 100 mK by the DR mixing chamber stage.

simulation using numerical ray optics. The circularly symmetrized geometry (shown in Figure. 2.19 for our current design) and the spectral properties of the optics tube walls and filters are used as inputs to this model. An additional output of this simulation is a set of radial temperature profiles for all filter elements (computed using temperature-dependent thermal conductivities of the filter materials). The resultant thermal loads for each stage are shown in Tab. 2.4, while the optimized filter stack and corresponding center temperatures are shown in Tab. 2.5.



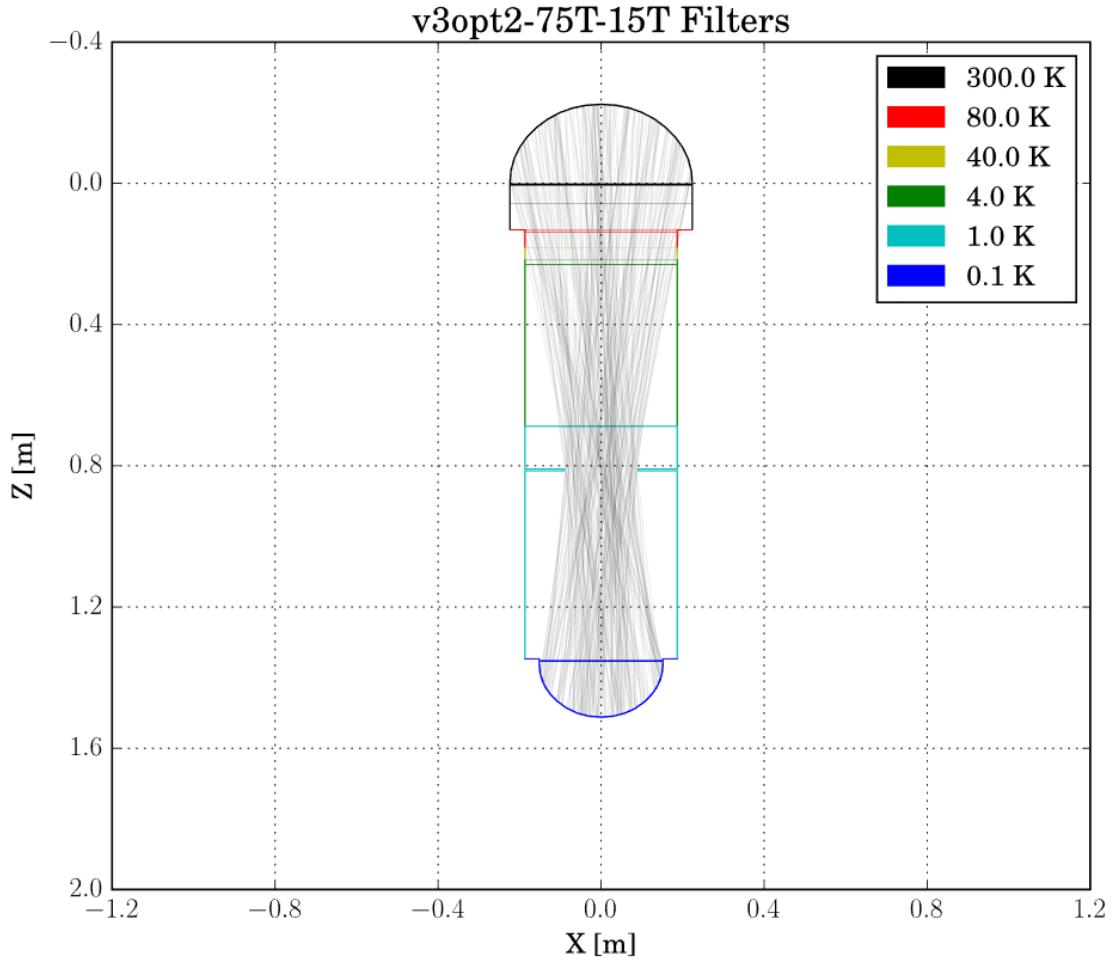


Figure 2.19: Geometry of the LATR optics tube showing all filter elements and walls at each stage. The lines shown in the graph do not represent the actual ray trace; they merely highlight the location of the Lyot stop.

Temperature Stage	300 K	80 K	40 K	4 K	1 K	100 mK
Optical Load (per optics tube)	-3.93 W	3.90 W	2.0 mW	27.6 mW	29 $\mu$ W	312 nW

Table 2.4: Table of thermal loading from the optical chain at each temperature stage. The negative loading at 300 K represents the total power that enters the window.

Power dissipation from electrical components such as the detector readout low noise amplifiers (LNAs) and TES biasing was also included in the thermal model. The LNA power dissipation was computed by multiplying the LNA drain current by

Temperature Stage	300 K	80 K	80 K	40 K	4 K	4 K	1 K	100 mK
Filter	IRB	IRB	AF	IRB	IRB	LPE	LPE	LPE
Filter Temperature	297 K	252 K	81 K	74 K	62 K	12 K	1.1 K	105 mK

Table 2.5: Table of optimized filter stack and center temperatures. “IRB” stands for IR blocking filter, “AF” stands for alumina filter, and “LPE” stands for low pass edge filter.

its drain voltage, using the nominal current and voltage from the specification sheet provided by Low Noise Factory (LNF)<sup>14</sup>.

### Temperature Gradient Analysis

We used the COMSOL<sup>15</sup> software suite to estimate thermal gradients across our 80 K, 40 K, 4 K, 1 K, and 100 mK stages. Our simulations used the computer aided design (CAD) model of the relevant thermal stage, with some simplifications that only minimally impact the accuracy of the simulations – for example, suppressing screw holes. Using the material library we developed for the thermal model we applied a material to each part, specifying its thermal conductivity as a function of temperature. Thermal loads were distributed throughout the model. To include the effect of the relevant cryocooler, a measured load curve of that cryocooler as a temperature dependant negative heat flux is applied to the cold head of the cryocooler. These simulations allowed us to identify which areas were cryogenically critical, leading us to make those areas thicker and more conductive. The simulations showed that to reduce the gradients throughout the stages, the radiation shields play a crucial role in conducting the cooling power besides shielding radiation. As a result of this for the 40 K stage that relies heavily on the shield to cool the filter plate, we used Al1100

<sup>14</sup>Low Noise Factory AB, <https://www.lownoisefactory.com/>

<sup>15</sup>COMSOL, Inc., <https://www.comsol.com>

whose thermal conductivity is significantly higher than Al6061. A summary of our predicted gradients and the LATR performance during validation tests can be found in Section 3.2.

During the lab testing phase, we performed additional simulations in conjunction with our cryogenic validation. For these simulations, we would mimic a given validation test setup, including whichever components were installed and using the measured cryocooler load-curves. We would then compare the gradients observed in the simulations to those observed in our validation testing. One major difficulty in the thermal validation of our cryostat at all temperature stages was that we were only able to put a limited number of thermometers on each stage, making it difficult for us to identify the source of un-accounted-for loading. This combined with the very long turn around time of our cryostat meant that we risked spending upwards of a month tracking down heat leaks. Given a proposed load, we would add that load in the simulation and compare the resulting temperature gradients to those observed. While the result of the simulation is not precise, missing among other things contact resistance, it is accurate enough to provide a sanity check. An example simulation is shown in Figure 2.20.

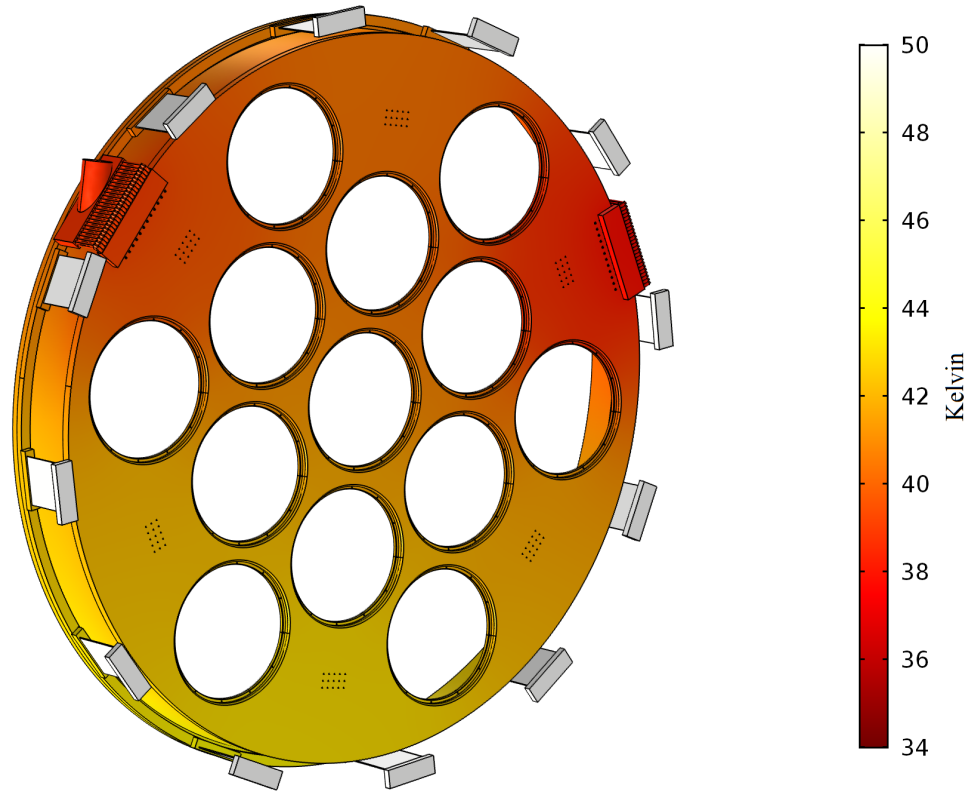


Figure 2.20: A thermal simulation of the 80 K stage. This simulation uses the individually-calibrated PT90 load curves. It was performed to emulate a dark thermal validation run with the windows closed, hence there is no optical load applied. The conductive load through the G10 tabs was included, as is radiative heating from the 300 K stage. The color map shows the distribution of the thermal gradient with the lowest temperature around the two PT90 thermal straps and the highest temperature at the bottom of the plate. This is one example of the thermal simulations we conducted for all the temperature stages. The simulation as shown indicated that the 80 K stage would have  $\sim 10$  K gradient if the total loading meets the estimations. The temperature gradient and loading at the 80 K stage measured during cryogenic validation test is discussed in Section 3.2.

### 2.3.3 Cooldown Calculation and Heat Switches

With a cryostat the size of the LATR, the main challenge for a relatively fast cooldown is distributing the available cooling power and minimizing the gradients

during the cooldown. At room temperature, the PT420s each provide up to 450 W of cooling power for the first stage and 225 W for the second stage. If all of the cryogenic material in the LATR were isothermal to the pulse tube heads, the cooldown time would be 5.3 days. However, gradients across the temperature stages reduce the pulse tube heads temperatures, and hence their cooling power, so that a realistic simulation is required to estimate the true cooldown time.

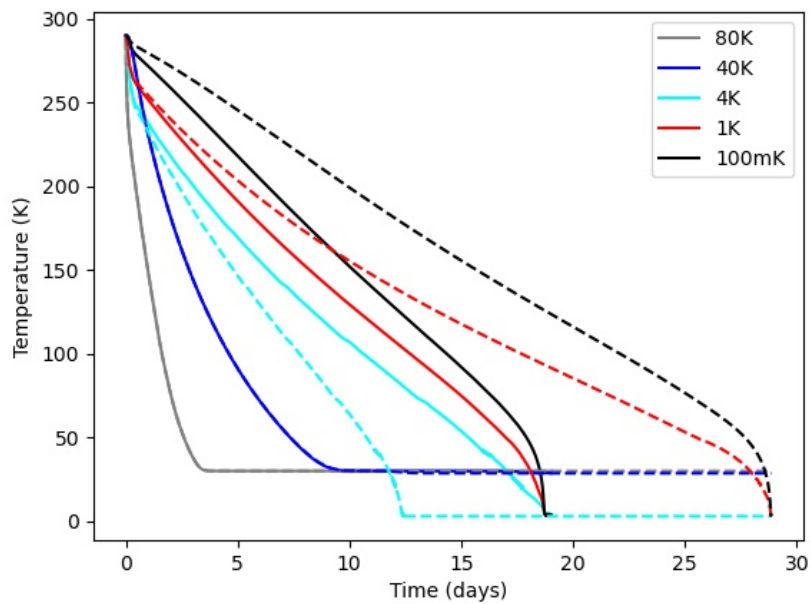


Figure 2.21: Simulated cooldown curve for a fully populated LATR with 13 optics tubes, showing each temperature stage. The solid lines show the result with mechanical heat switches connecting the 4 K stage with the 1 K and 100 mK stages while the dashed lines show the result without heat switches. The heat switches significantly reduce expected cooling time.

We developed a code based on a finite difference method as described in Coppi et al. [17]. The results for the LATR with 13 optics tubes are presented in Figure 2.21. The warmer stages – 80 K, 40 K and the 4 K – cool relatively quickly, in less than 19 days. However, initial simulations showed that it could take up to 28 days for

the coldest stages – 1 K stage and 100 mK stage – to reach 4 K. After reaching 4 K, mixture condensation, the process in which the DR reaches its base temperature of 100 mK only takes a few hours. A detailed cooldown time measurement with 1 optics tube and 3 filter sets is presented in Section 3.2.

To reduce cooldown time, we installed a nitrogen heat pipe and two mechanical heat switches. We studied multiple options for accelerating the cooldown process, such as using an external cooler to force cold gas circulation in an internal vacuum chamber [8], liquid nitrogen flow through a plumbing system [52], nitrogen heat pipes connecting 4 K stage to the colder stages [25], and the use of mechanical heat switches from 4 K stage to the colder stages. The first two options were discarded due to mechanical design complications and the risk of developing large temperature gradients in the cryostat that would induce thermal stresses on critical components such as lenses and filters. Moreover, as stated above, the LATR *has* sufficient cooling power, but requires optimization of its distribution. We chose to apply the remaining two options because they are relatively easy to implement from a mechanical design point of view. Nitrogen heat pipes are intrinsically passive elements with high thermal conductivity between 63 K and 110 K and close to zero outside this range. A nitrogen heat pipe was custom installed on the DR by Bluefors (shown in Figure 2.22). Mechanical heat switches have very high thermal conductivity when closed and zero when open, but require some activation mechanism. Mechanical heat switches manufactured by Entropy<sup>16</sup> were chosen for the LATR. These heat switches have a nominal conductance of 0.5 W/K at 4 K when closed. Figure 2.23 shows a photo of the heat switches installed on the 4 K plate. One switch connects the 4K and 1K

---

<sup>16</sup>Entropy GmbH, <http://www.entropy-cryogenics.com/>

stages while the other connects the 4K and 100 mK stages. With these heat switches, a fully-equipped LATR (with 13 optics tubes) would cool in around 18 days according to our simulations. For contingency, there is enough space on the 4 K plate to include another set of mechanical heat switch assembly, but it does not appear necessary for the 7 optics tube configuration. The actual cooldown times with one optics tube and seven optics tube are discussed in Section 3.2.2.

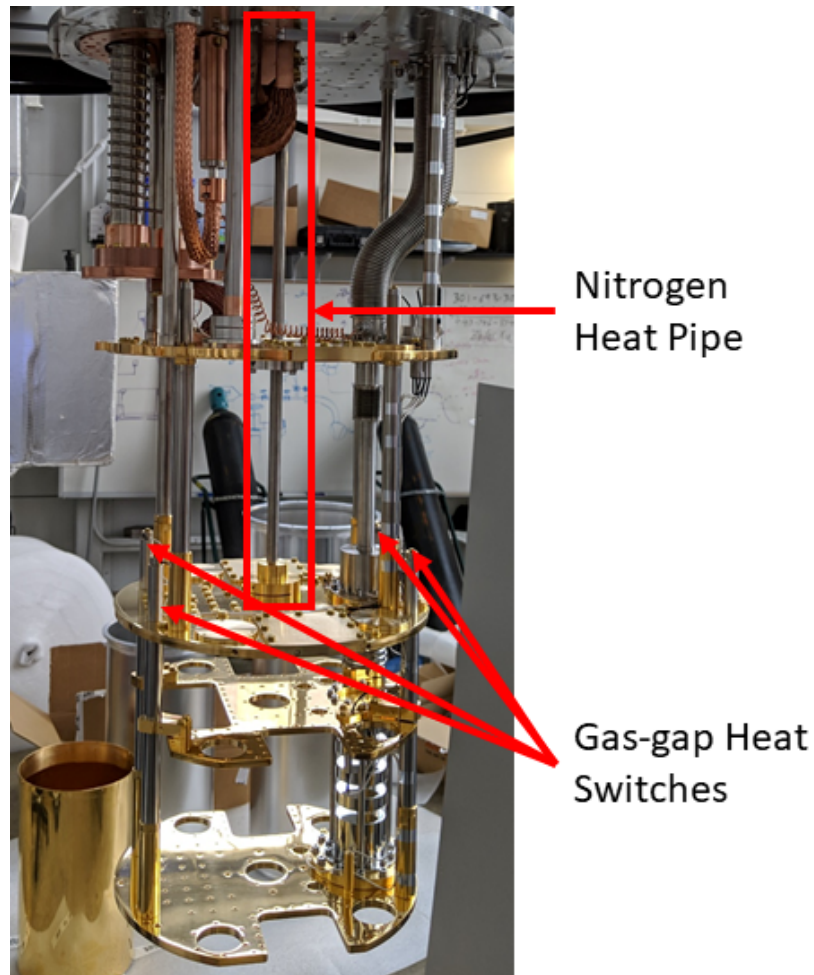


Figure 2.22: A picture showing the heat pipe custom installed in the LATR DR. The Heat pipe starts from 40 K stage, go through 4 K stage, and arrive at 1 K stage to help reduce the temperature gradient during cooldown. Also shown are four gas-gap heat switches custom installed between 1 K and 100 mK stages.

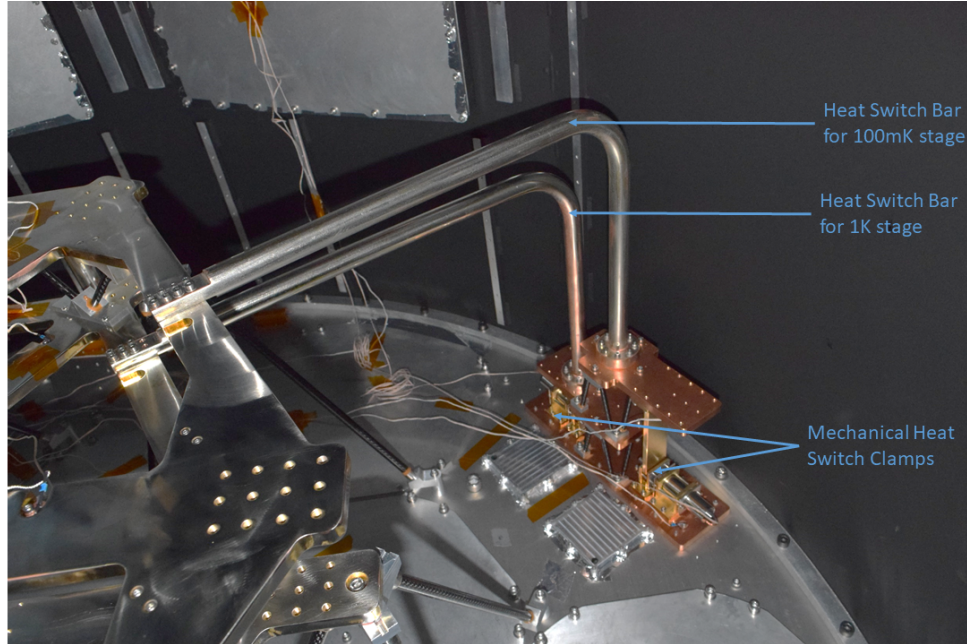


Figure 2.23: A picture showing the heat switch assembly. The mechanical motor and clamps are bolted to the 4 K plate. On top of the clamp structure, two OFHC bars are bolted to 1 K and 100 mK thermal BUSES.

## 2.4 Readout Interface Design

The LATR needs to read out  $> 62,000$  detectors,  $> 120$  thermometers, 12 heaters, and two heat switches, which all require cables running from the room temperature to cryogenic temperatures. The design requires them to be routed across different temperature stages in an efficient and organized manner. There are five ports on the side of the LATR, penetrating through the 300 K, 40 K, and 4 K stages. Four of the ports are used for detector readout cables while the fifth is used for housekeeping cables (thermometers, heaters, and heat switches).



### 2.4.1 Cold Detector Readout Interface

In the LATR, 13 optics tubes require 156 coaxial cables and 2,400 DC wires to be routed without introducing unacceptable thermal loading. To address this, the SO developed the modularized universal readout harness (URH) [85] for both the LATR and the SAT [9]. One URH contains 48 coaxial cables penetrating three temperature stages from 300 K to 4 K. A small portion of the coax cables can be seen in Figure 2.24. In addition, each URH carries 600 DC cryogenic wires to bias detectors and amplifiers, and convey flux ramps. The LATR requires four URHs to operate and read out all the detectors in 13 optics tubes.

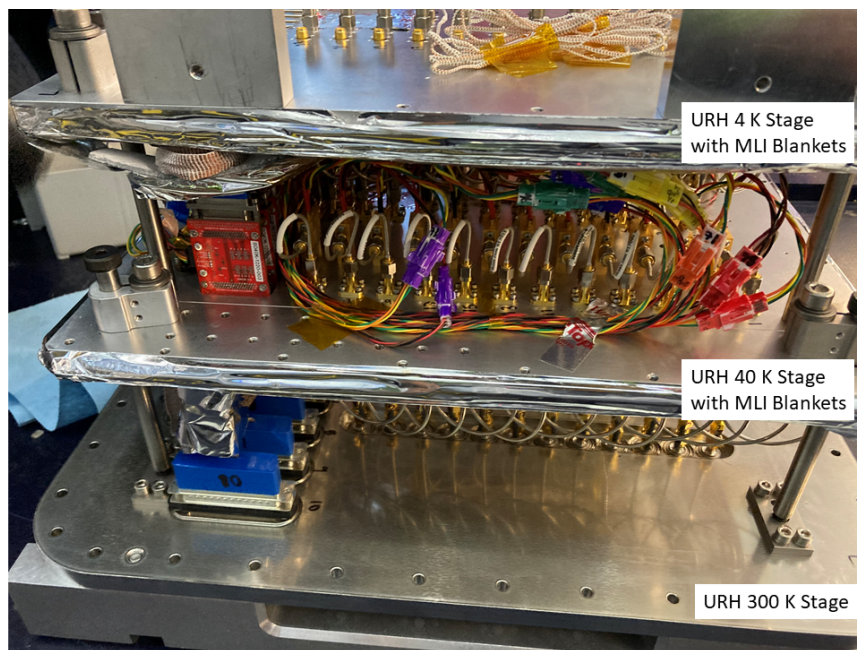


Figure 2.24: This picture shows the URH with the coax cables installed. The MLI blankets at 40 K and 4 K stage are also shown in the image.

Given the complexity of the cable harness and the number of cables bridging different temperature stages, uncontrolled thermal loading is a major concern. MLI blankets were tailored with minimal openings for all the cables on 40 K and 4 K

plates. Since simulations on the thermal performance of the MLI sheets with many penetrations is unreliable, the URH thermal simulation only includes the thermal conductivity from the cables. The simulated thermal loading is 3 W (from conductive load) at the 40 K stage and 0.3 W at the 4 K stage. Measurement in another cryostat shows loading at the 40 K stage is  $\sim 7$  W while the loading at the 4 K stage is  $\sim 0.15$  W. This result demonstrates the success of the MLI design at the 40 K stage, implying only  $\sim 4$  W of radiative load. Meanwhile, the measured 4 K stage thermal loading is only half of the value predicted by simulations.

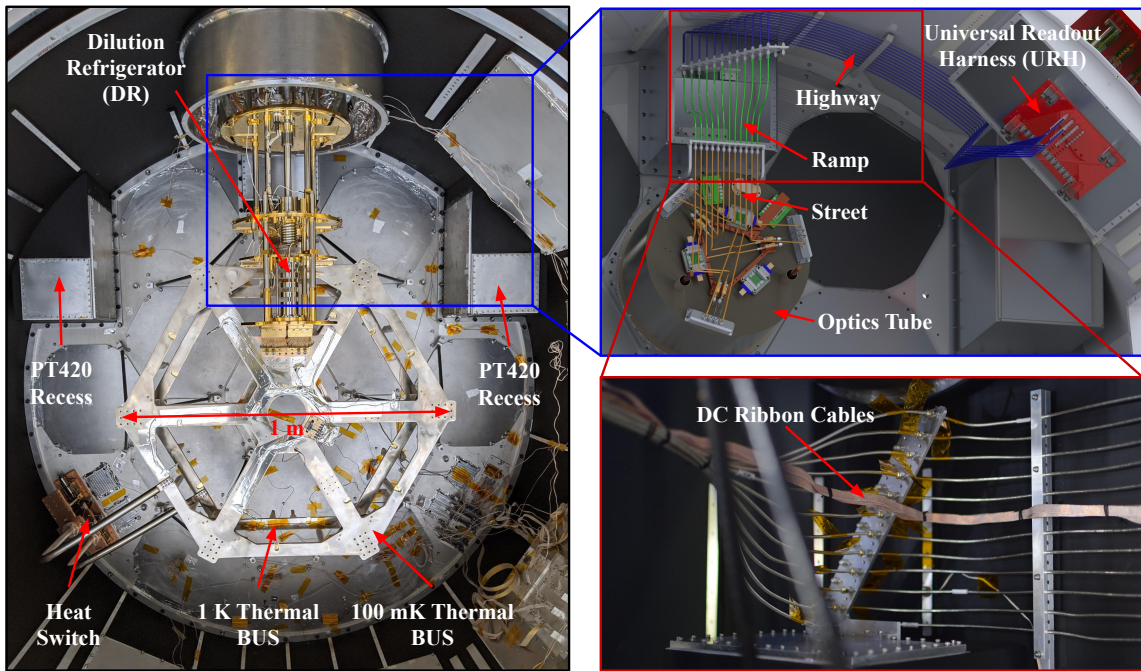


Figure 2.25: 4 K cavity and coaxial cables. The photo on the left shows the overview of the 4 K cavity, with the 1 K/100 mK Thermal BUS, DR, and heat switches installed on the 4 K plate. The major components are labeled along with 1 m scale. A zoom-in on the top right shows the design of the coaxial highway and street system for one optics tube. Other isothermal 4 K coaxial cable runs and the DR have been hidden for clarity. The highway is in blue, the ramp in green, and the street in orange. Note the relatively short, simple runs of the ramps. The connection to the URH as installed is not as angular as in this rendering. The bottom right photo shows another zoom-in of the installed 4 K isothermal coaxial cables in the LATR.

All the coaxial cables and the DC wires need to leave the cryostat through the four URHs. Care was taken in the routing of the coaxial cables to satisfy space constraints while minimizing the obstruction of the 4 K working space by the coax. Additionally, we wanted to reduce the amount of coax that would need to be removed/installed for an optics tube removal/installation, as well as reduce the complexity of those segments to minimize the amount of time spent removing and installing coax. Therefore, instead of directly routing individual cables for the shortest run, we ran the majority of the cables along the inside of the 4 K shell, minimizing the interference with the optics tubes. Analogous to a road system, our isothermal 4 K coax are designed in three parts: highways, ramps, and streets (Figure 2.25). The highways run along the inside of the 4 K shell from the URH to a set of permanently installed bulkheads, each located along the interior of the shell as close as possible to its corresponding optics tube. The highways are supported along their length, and constitute most of the length of the 4 K isothermal run (up to 1.5 m). Each optics tube has an individual set of matching bulkheads on the back of the 4 K shell. The streets are permanently installed sections that run from those bulkheads to penetrations in the magnetic shielding, connecting to other cables deeper in the optics tube. This arrangement allows most of the complex routing to be permanently installed. Connecting the street bulkheads and the highway bulkheads are the ramp sections: short ( $\sim 20$  cm) pieces of hand formed coax. These are the only part of the isothermal 4 K run that are not permanently installed, and hence are the only pieces that have to be added or removed when installing or removing an optics tube. The DC cables run along the isothermal 4 K coax, and are tied down to the coaxial highways, ramps, and streets. See Figure 2.25 for an example of one optics tube's isothermal 4 K run.

## 2.4.2 Warm Detector Readout Interface

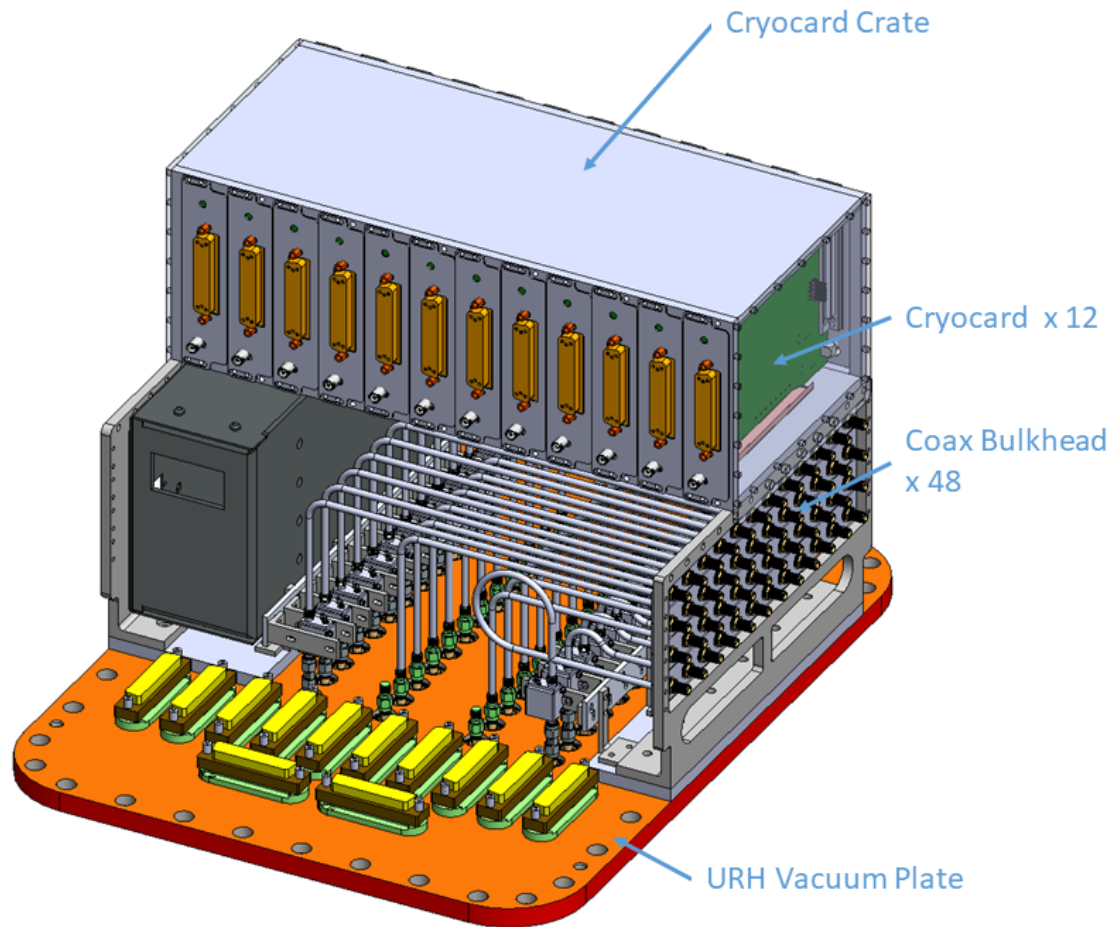


Figure 2.26: This is a rendering of the cryocard crate on top of the URH assembly. The physical crate is supported by a pair of L-brackets, and can contain up to 12 cryocards.

In order to route the warm coax cable in an organized manner, we design a crate assembly to collect all the coax cables in one place. The assembly has an adjustable support for the amplifiers installed on the URH plate, and acts as a weight relieve suspension to protect the vacuum seal coax connectors in case anyone accidentally bumps into the cables. It also provides housing for the cryocards that are part of

the SMuRF readout systems (see [41] for more details on the SMuRF system). The design confines the components within the foot print of the URH vacuum plate, so that they will not interfere with other components on the cryostat.

### 2.4.3 Housekeeping Readout Interface

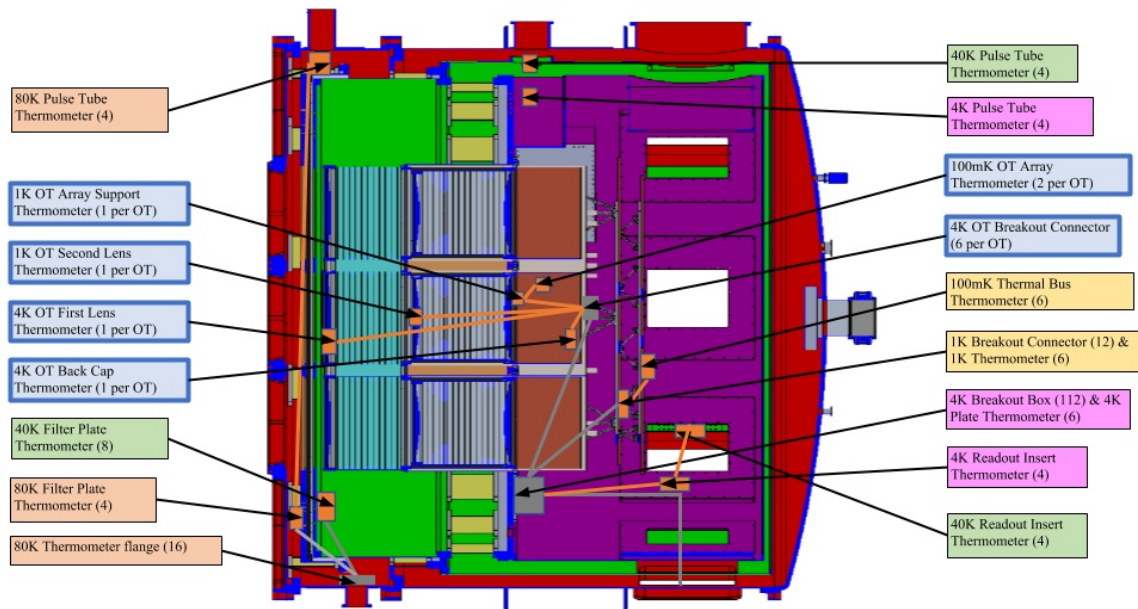


Figure 2.27: Thermometer plan for LATR. In total, 128 thermometers were planned for LATR, capable of supporting full 13 optics tube during normal operation. However, during cryogenic validation testing, we often wish we can support more thermometers than planned to measure temperature gradient for excess loading diagnoses.

The LATR's temperatures are monitored with 128 thermometers, distributed across the 80 K, 40 K, 4 K, 1 K and, 100 mK stages. The schematic distribution for the thermometers is shown in Figure 2.27. At the 80 K, 40 K and 4 K stages, we installed DT-670 silicon diodes, manufactured by Lake Shore Cryotronics.<sup>17</sup> For the 1 K and

<sup>17</sup>Lake Shore Cryotronics, <https://www.lakeshore.com/>

100 mK stages, we use ruthenium oxide (ROX) sensors<sup>18</sup>, also from Lake Shore. The diodes and ROXs were potted in custom-built copper bobbins with Stycast 2850 FT, along with heat sinking wires and a micro connector. One example of such bobbin is shown in Figure 2.28. All thermometers are read out via a four-wire measurement, with cables manufactured by Tekdata Interconnections.<sup>19</sup> The cables are routed via cryogenic breakout boards that were developed for the SO. The thermometers purchased from Lake Shore were calibrated in-house in a dedicated Bluefors DR against pre-calibrated reference sensors.

To carry the signal to the exterior of the LATR, we designed an assembly based on the URH design, called the housekeeping harness. Outside of the LATR, we employ Lake Shore measurement modules to do thermometry data acquisition. For 100 mK thermometers, we utilize two Lake Shore 372 AC Resistance Bridges, each coupled to a 16-channel scanner<sup>20</sup>. All other thermometers on higher temperature stages are read out with Lake Shore 240 Series Input Modules. All the thermometry data is read out and stored using the Observatory Control System (OCS) software developed for the SO [48]. For normal operations where the thermometers are multiplexed, they are read out in 30 second intervals. For laboratory testing where a faster readout rate is desired, a single thermometer can be read out at  $>1$  Hz. The housekeeping harness is also used to monitor and control other systems including the heat switches, low-power heaters for testing, and high-power heaters to facilitate warming up the system.

---

<sup>18</sup>Model # RX-102A-AA

<sup>19</sup>Tekdata Interconnections, Ltd., <https://www.tekdata-interconnect.com/>

<sup>20</sup>Model 3726

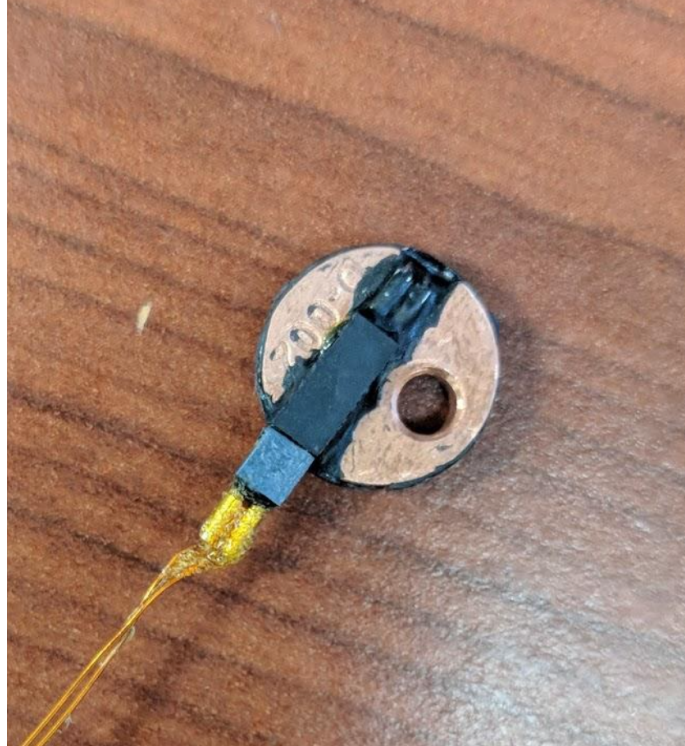


Figure 2.28: Thermometer assembly. Shown in the figure is a diode thermometer. The Lake Shore DT-670-SD temperature sensor was inserted and epoxied within the brown copper bobbin. The heat-sunk wires were wrapped around the bobbin and black epoxied around before it came out to the connector which was epoxied on the bobbin. Next to the epoxied connector, there is a M3 clearance hole for bolting the thermometer down. The ruthenium oxide sensors share the same design except the bobbin is slightly thicker to accommodate the RX-102A-AA sensor size.

## 2.5 Telescope Interface Design

### 2.5.1 LATR Co-rotator

According to the LAT optics design [22], the LATR must co-rotate with the telescope elevation structure as the telescope points from  $0^\circ$  to  $90^\circ$  in elevation (Figure 2.1). The co-rotator, as shown in Figure 2.29, consists of a pair of co-rotator rails that are bolted to the front and back flange of the LATR, and a cradle that supports and rotates the rails. The design creates a stable support structure for the

LATR while allowing adjustments in the co-rotator cradle bases for accurate on-axis alignment. The co-rotation makes sure that the LATR sees the same area of the telescope mirrors at different elevations. We plan to test the co-rotator structure with a dummy LATR mass before deployment.

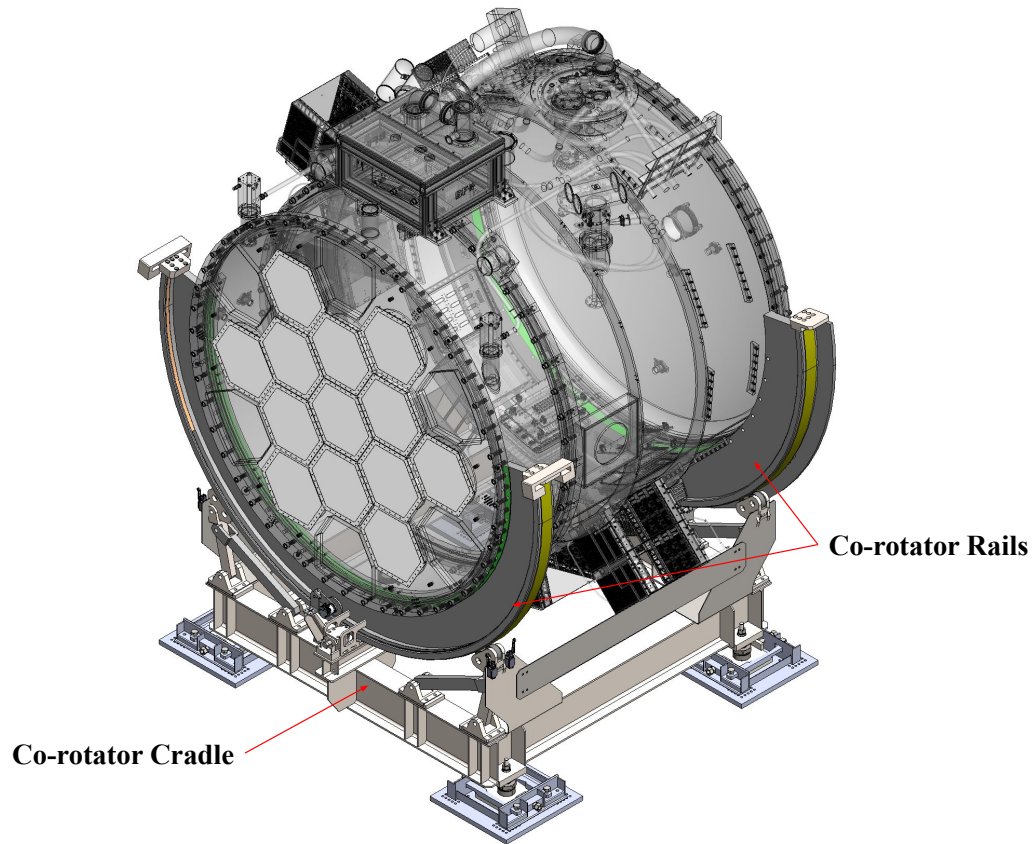


Figure 2.29: The LATR co-rotator. The co-rotator rails are bolted to the front and back flange of the cryostat. The four feet of the co-rotator cradle allows for fine adjustment when aligning the cryostat with the secondary mirror. In this rendering, the cryostat is transparent to showcase the co-rotator parts.

The pulse tube cooler hoses, along with all the electronic cables, converge at the cable hub on top of the cryostat (Figure 2.2), before going through the cable wrap. The cable wrap attaches to the cryostat, and bends in a controlled manner as the cryostat co-rotates, safely guiding the motion of the hoses and wires.



## 2.5.2 LATR Lifter

The original plan for lifting the LATR into the LAT is by using four individual of straps. However, due to space limitation on the LAT, the crane hook is limited to be only  $\sim 2$  m above the optical axis of the cryostat. Given the diameter of the cryostat at 2.4 m, the hook will only be  $\sim 0.8$  m off the cryostat shell. With cryostat at 2.6 m long, using simple lifting straps is no longer realistic since their angle would be too steep. Therefore, a spreader-bar type structure is designed and manufactured by Engineered Lifting Technologies<sup>21</sup> for LATR. To assist with the lifting operation, we also developed a four-point support structure that stands on the LATR cart platform and is capable of supporting the weight of the LATR temporarily while the lifter is being installed or adjusted. The adjustable steel lifting shores are made by Ellis Manufacturing<sup>22</sup>. Both the lifter and the support are shown in Figure 2.30.

The lifter has a 6,800 kg capacity, is proof load tested to a minimum of 125% of working load limit, and is rated for service class one (20,000 to 100,000 cycles). The estimated weight of the cryostat with 13 optics tube installed is  $\sim 5,500$  kg, and the cart assembly is estimated to be  $\sim 1,200$  kg. The combined weight, 6,700 kg is still below the safety rating. This means that even if the crane operator accidentally lift the cryostat while it is still attached to the cart, the lifter is still within operating capacity. On the other hand, the LAT receiver cabin crane is only certified to 6,000 kg. Thus the lifting procedure will likely to be limited by the crane capacity.

---

<sup>21</sup>Engineered Lifting Technologies, Inc., <https://www.eltlift.com/>

<sup>22</sup>Ellis Manufacturing CO., <https://ellismanufacturing.com/>

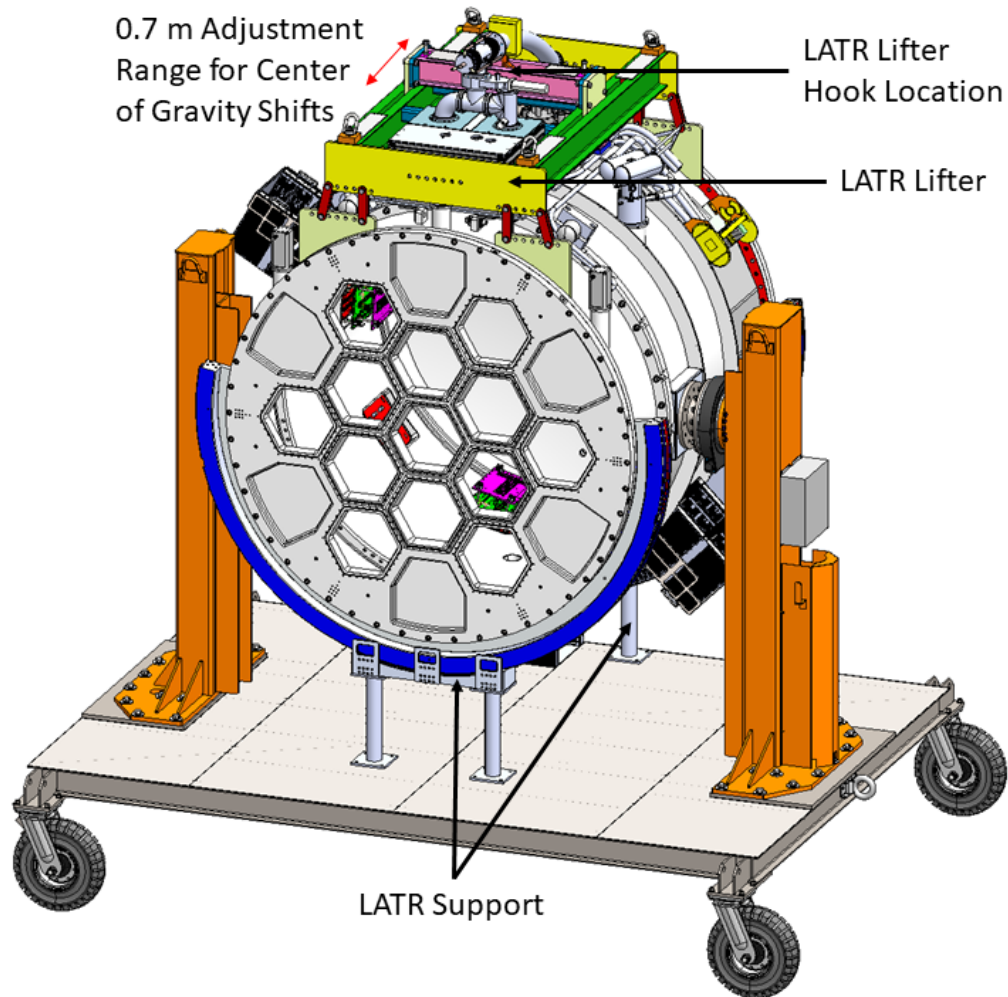


Figure 2.30: This rendering shows the LATR lifter and the support structure. The support structure is bolted to the LATR cart platform and is designed to support the weight of the LATR temporarily. The lifter is bolted to the cryostat via eight sets of adjustable links, which allows the lifter to stay on top of the cryostat without hitting any components on the top. The center beam is designed to have  $\sim 0.7$  m adjustment range along the cryostat optical axis. This range can accommodate center of gravity shifts with different configurations.

## Chapter 3

# SO LATR Validation Testing

During the assembly of the LATR, we performed several rounds of metrology to guarantee the stringent alignment requirements were achieved under different loads for 300 K, 80 K, 40 K, and 4 K stage. We also measured various components of the optics tube with respect to the 4 K flange to validate their alignment.

The cryogenic properties of the LATR were systematically tested in multiple configurations, including dark tests, optical tests, and tests with optics tubes installed. We tilted the entire cryostat to test its performance at different orientations as well as to determine the thermal time constant of the system.

After the cryostat and first optics tube were successfully integrated and tested for the mechanical and cryogenic performance, the RF chain for reading out the detectors was connected (and looped back at the 100 mK stage).

## 3.1 Mechanical Test

### 3.1.1 Cryostat Mechanical Validation

Before installing any internal components, the empty cryostat was pumped down to high vacuum multiple times and leak checked to  $5 \times 10^{-8}$  mBar· l/s at the factory. After transporting the cryostat to the lab, it was pumped down and stayed at high vacuum for months, proving that it is leak tight and is capable of withstanding vacuum pressure.

Axis	Deviation from Origin (Simulated)	Deviation from Origin (Measured)
X-axis	0 mm	$0.22 \pm 0.05$ mm
Y-axis	0 mm	$0.19 \pm 0.05$ mm
Z-axis	18.1 mm	$17.2 \pm 0.03$ mm

Table 3.1: This table highlights the expected and measured position of the LATR’s front plate under vacuum. The expected position of the front plate under vacuum is provided by the simulation performed in [63] and shown in Figure 2.6. The nominal origin, and thus center of the front plate, is assumed to be (0,0,0) in a 3D coordinate system. All deviation values are absolute values of the measured deviations of the center of the front plate from the origin.

To ensure these tight tolerances were met, we used the FARO Vantage Laser Tracker<sup>1</sup> to measure the locations of all relevant surfaces both internal to, and external to, the cryostat at room temperature. A picture during such measurement is shown in Figure 3.1. The FARO Vantage Laser Tracker has an accuracy of  $16 \mu\text{m}$  and a single point repeatability of  $8 \mu\text{m}$  at 1.6 m.

We measured the LATR’s front plate while under vacuum to ensure that the deformation of the plate was within the expected regime. Simulations of the deformation of the front plate can be found in Table 3.1 along with the measurement results. From

---

<sup>1</sup>FARO, <https://www.faro.com/>

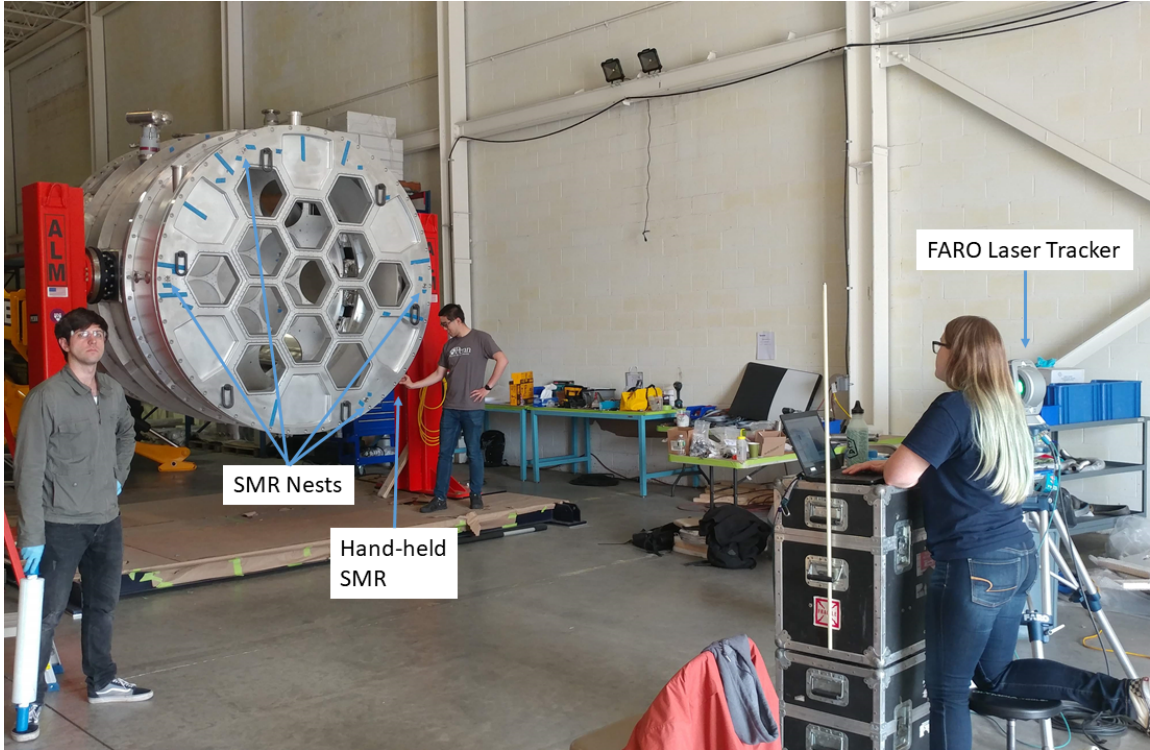


Figure 3.1: This picture shows the FARO measurement in progress. The four spherically mounted retroreflector (SMR) nests provide reference points on the front plate that we can go back to between measurements. They also establish a reference frame if we need to move the laser tracker during measurement. The hand-held SMR allows us to measure surfaces and planes approximated by a point cloud taken by the laser tracker.

these results, we can see that the measured deformation along the Z-axis, or bowing, was within 1 mm of the simulated result (slightly smaller than expected), solidifying our confidence in robustness of the cryostat’s design.

Comprehensive simulations were performed to set the required tolerance for the alignment of the LATR optical components [22]. The location of the LATR is referenced to the telescope-receiver interface: the co-rotator. Utilizing a reference plane that is external to the receiver shell ensures that the optical components within the LATR will be aligned with the primary and secondary mirrors in the

LAT. The positions of optical components within the LATR—including the lenses, filters, and detectors—must adhere to tight tolerance requirements, both statically and dynamically (i.e. during co-rotation).

Optimization of Strehl ratios using optical simulations [22] lead to tight physical constraints being placed on the locations of our optics tubes and cryogenic lenses. The position of the optics tubes must be maintained within  $\pm 3$  mm along the LATR’s optical axis and  $\pm 3$  mm perpendicular to the LATR’s optical axis. In addition, the optics tubes must not exceed  $\pm 0.8^\circ$  in tilt with respect to each other. These constraints need to be met when the cryostat is initially deployed with a small number of optics tubes and also when it is fully loaded with 13 optics tubes. The requirement must also be maintained when the LATR is rotated.

The Vantage Laser Tracker was also used to verify the overall dimensions of the cryostat, the 3D locations of each of the four temperature stages, and the precise locations each optics tube will inhabit when installed. Due to the nature of the cryostat and the support provided by the 4 K stage, it was important for us to measure the location of the 4 K stage both with and without the load of 13 optics tubes. Upon measuring the various temperature stages with no load on the 4 K stage, we were able to conclude that the positions of our optics tubes would be well within our required tolerances. A detailed list of the measured position of the 4 K plate without optics tubes can be found in Table 3.2.

We were also able to perform measurements of the 4 K stage with 13 optics tube mass dummies installed, as shown in Figure 3.2. These mass dummies accurately reproduced both the total mass and the location of the center of mass for each optics tube. Once all 13 mass dummies were installed, the metrology process was repeated.

Axis	Tolerance	Deviation from Origin (no load)	Deviation from Origin (13 optics tube load)
X-axis	3 mm	$0.49 \pm 0.03$ mm	$0.31 \pm 0.02$ mm
Y-axis	3 mm	$2.04 \pm 0.03$ mm	$2.24 \pm 0.02$ mm
Z-axis	3 mm	$2.03 \pm 0.03$ mm	$2.43 \pm 0.02$ mm

Table 3.2: This table shows the position of the 4 K plate under two configurations: no load and with load. No load measurements refer to those performed with no optics tube mass dummies installed. Loaded measurements refer to those performed with 13 optics tube mass dummies installed. Under both conditions, the plate is within the required tolerances provided by [22]. The nominal origin, and thus center of the 4 K plate, is assumed to be (0,0,0) in a 3D coordinate system. Looking at the cryostat from a viewpoint in front of it, Z-axis is the optical axis, Y-axis is pointing towards the ground, and X-axis is pointing towards the right. All deviation values are absolute values of the measured deviations of the center of the 4 K plate from the origin.

Even with all 13 mass dummies added, the 4 K plate remained within the required positional tolerances. A detailed list of the measurements recorded for the loaded 4 K plate can be found in Table 3.2. As can be seen from the measurements, the difference between the loaded and the unloaded measurements is less than 0.5 mm, which is within specifications. The overall offset in the Y and Z axes is likely due to build-up of manufacturing tolerances. The Z-axis offset can be removed by re-focusing. The Y-axis offset could be removed by shifting the 4 K cold plate, if necessary.

Since the co-rotator on the LAT is not yet available, we are unable to measure the LATR at a variety of different clocking orientations. However, the difference between the unloaded and loaded displacements provided in Table 3.2 suggest that optical alignment will be well within specification. When the LAT and LATR are assembled together at the Chilean site, metrology measurements will be performed to ensure the proper alignment of the optical components in various orientations. Given the current measurement and the circular symmetry of the LATR, we are confident that the results will hold with rotations between  $-45^\circ$  and  $+45^\circ$ .

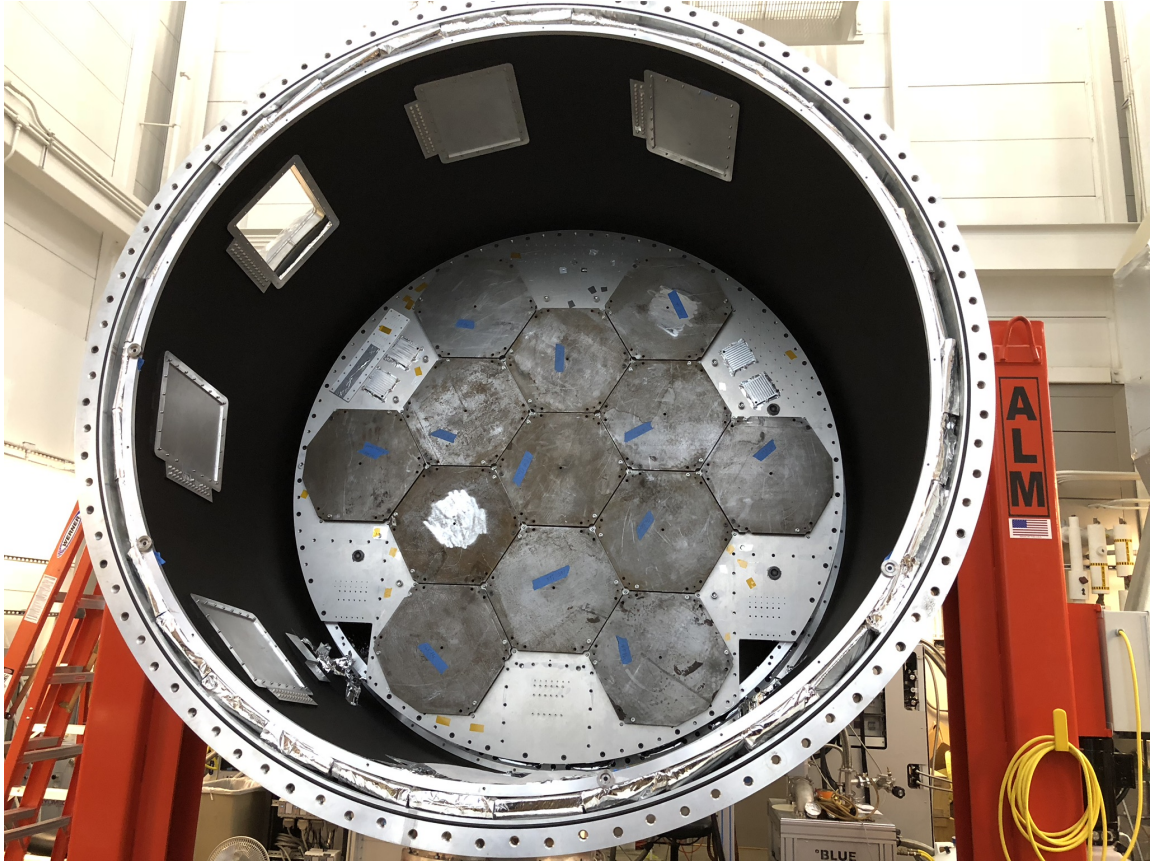


Figure 3.2: This picture shows thirteen dummy optics tube installed on the LATR 4K plate during mechanical validation of the cryostat. The dummy optics tube made of welded steel pieces represents the weight and center of mass of the actual optics tube.

Beyond the work on the LATR, the FARO Vantage Laser Tracker will also be used within the LAT to ensure the proper positioning of the mirror panels for the telescope's primary and secondary mirrors with respect to the cryostat.

### 3.1.2 Optics Tube Mechanical Validation

The optical simulations performed also provided constraints on our lens positions within the optics tube themselves. All three lenses within the optics tubes must maintain a position of  $\pm 2$  mm along the LATR's optical axis and  $\pm 2$  mm perpendicular



to the LATR's optical axis. The tilt of each lens must not exceed  $\pm 0.4^\circ$  with respect to the axis perpendicular to the optical path. The focal plane array within the optics tube must maintain a position of  $\pm 2.5$  mm along the LATR's optical axis. Further constraints placed on the beam guiding 80 K alumina wedges and the surface accuracy of the lenses can be found in [22].

Due to the size and intricate design of the optics tubes, we utilized the FARO Edge ScanArm to obtain precise cold optical component and detector array locations. The lens and optics tube metrology was performed on (warm) tubes before they were installed in the LATR to allow for easier access to hard-to-reach locations within the tubes. The FARO Edge ScanArm has an accuracy of  $34 \mu\text{m}$  and a repeatability of  $24 \mu\text{m}$  at 1.8 m. Each individual mechanical component of every optics tube is measured and recorded. Partial and full sub-assemblies of the optics tube are also measured, thus allowing us to understand the position of, parallelism between, distance between, and coaxiality of all components within each optics tube. Tight constraints on the locations of the focal plane array and lenses created a need for extensive documentation of all dimensions of optics tube components. Measurements of the positions of the optical elements and their deviations from designed locations can be found in Table 3.3. From these measurements, we have deduced that all of the lenses, the Lyot stop, and the focal plane in the first optics tube are located within the required tolerances.

Optical Element	Z-axis Tolerance	Deviation from Design
Lens 1	2.0 mm	$0.47 \pm 0.02$ mm
Lens 2	2.0 mm	$0.19 \pm 0.02$ mm
Lens 3	2.0 mm	$0.50 \pm 0.02$ mm
Lyot Stop	2.0 mm	$0.22 \pm 0.02$ mm
Detector Arrays	2.5 mm	$0.53 \pm 0.02$ mm

Table 3.3: This table reports the positions of the optical elements within a LATR optics tube. The z-axis travels along the central axis of the cylindrical optics tube. The listed tolerances are provided by [22]. All deviation values are absolute values of the measured deviations of central plane of each element, perpendicular to the central axis, with respect to the designed central plane for each element.

## 3.2 Cryogenic Test

### 3.2.1 Cooler Calibration

In order to know the total thermal loading on each stage precisely, we calibrated all four pulse tube coolers individually in a smaller and well-understood cryostat, measuring their specific cooling power at different temperatures. The cooling capacity map is shown in Figure 3.3 and Figure 3.4. The information enabled us to accurately deduce the thermal loading on each stage by closely monitoring the pulse tube cold head temperatures.

### PTC#1 Capacity Map

Red values mean load on the 4K stage and Blue on the 40K stage

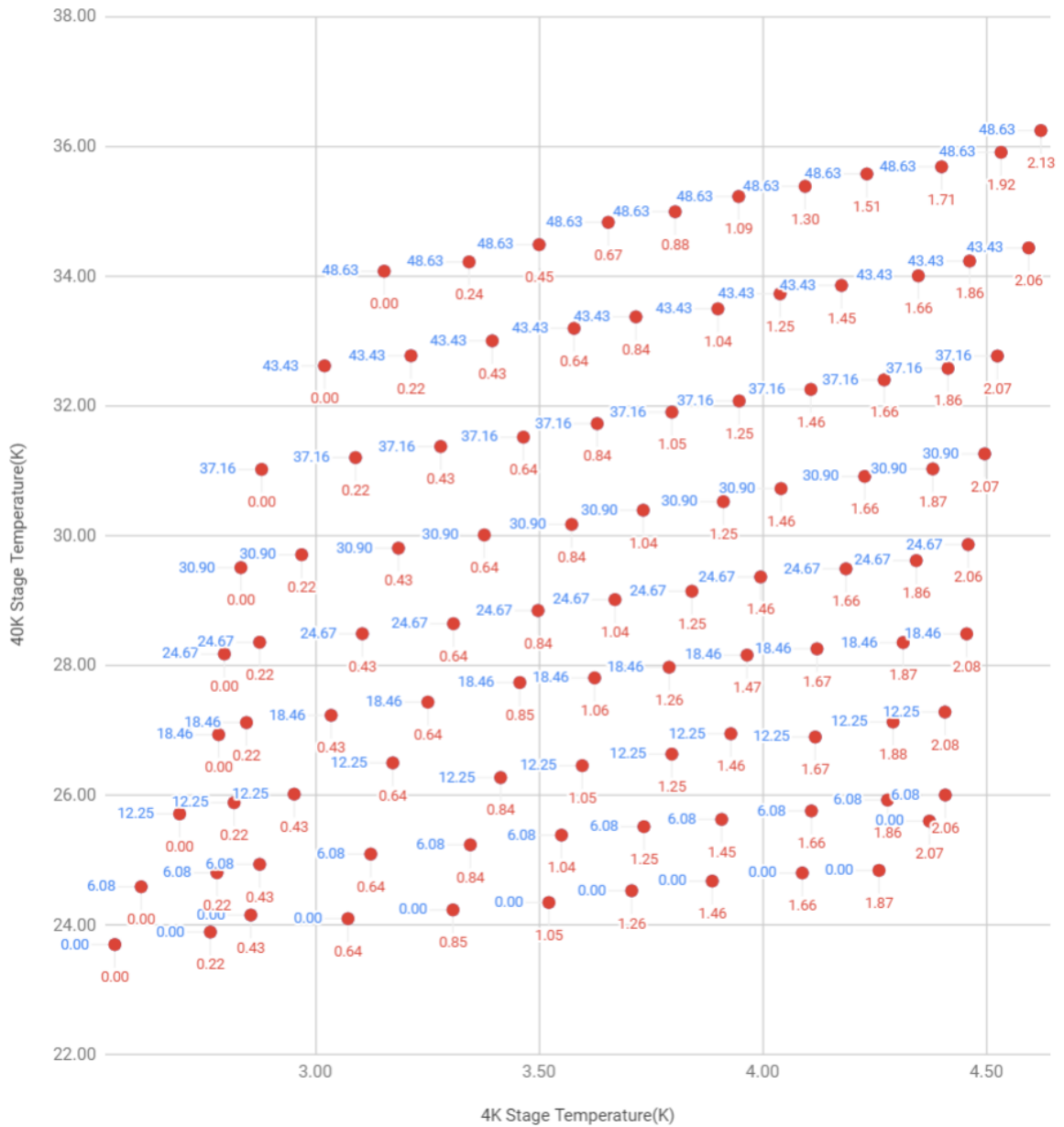


Figure 3.3: This graph shows the cooling capacity of the PT420-1 as a function of the 40 K and 4 K stage temperature. The blue number is the 40 K stage power, and the red number is the 4 K stage power. Plot credits: Zhilei Xu and Gabriele Coppi.

### PTC#2 Capacity Map

Red values mean load on the 4K stage and Blue on the 40K stage

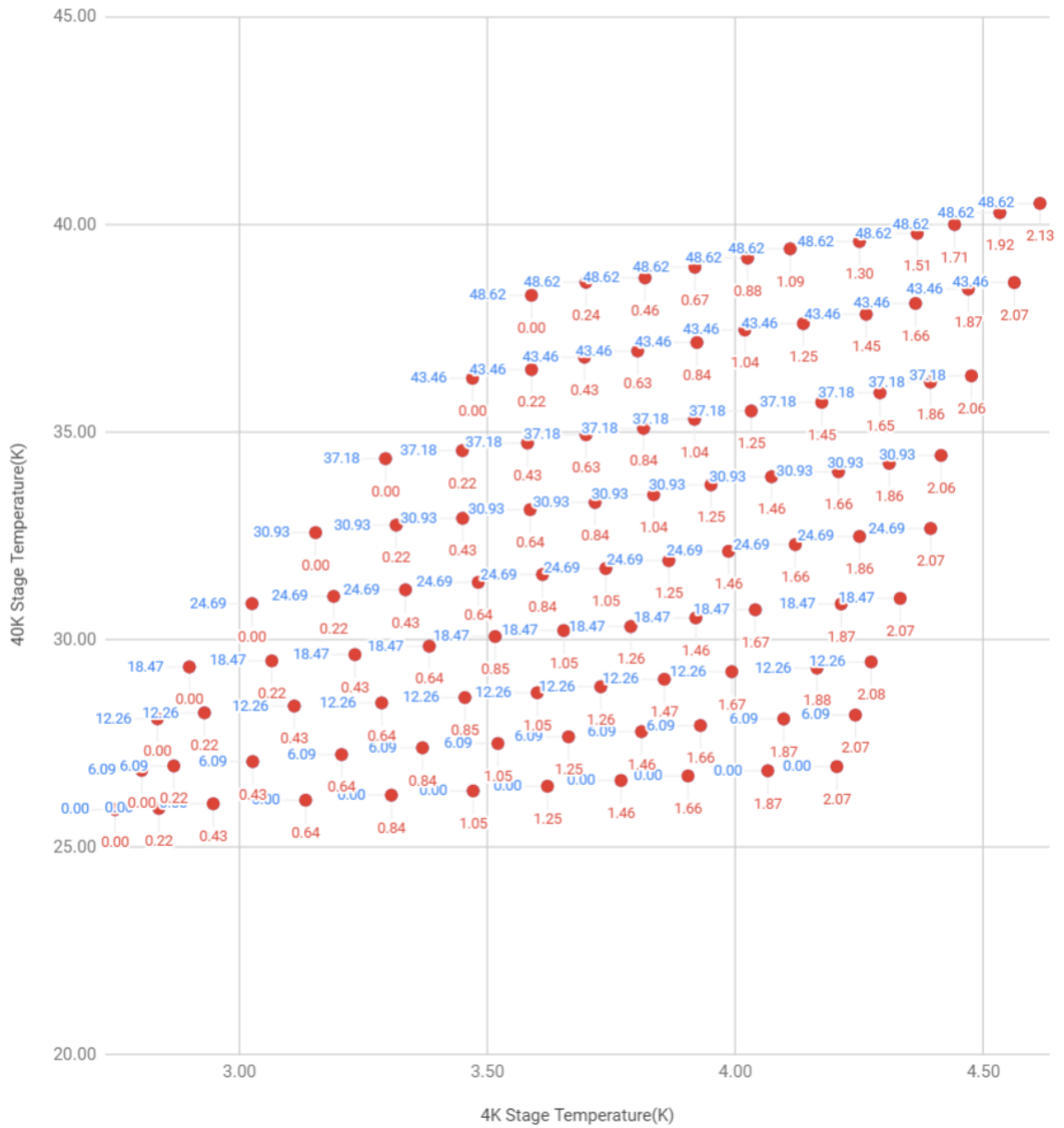


Figure 3.4: This graph shows the cooling capacity of the PT420-2 as a function of the 40 K and 4 K stage temperature. The blue number is the 40 K stage power, and the red number is the 4 K stage power. Plot credits: Zhilei Xu and Gabriele Coppi.

Similar to the pulse tube coolers, the DR performance is also calibrated separately.

However, its performance depends on 40 K, 4 K, 1 K and 100 mK stage temperature, and all of them would be different in LATR from in a much smaller cryostat. As a result, we found it more useful to calibrate the performance of the DR inside the LATR, with its 40 K stage and 4 K stage attached to the LATR, and the 1 K and 100 mK thermal BUS installed. This way, the cooling capacity only depends on the additional loading on the 1 K stage and 100 mK stage from the optics tubes. With this setup, we measured the lowest mixing chamber temperature to be 29 mK, when 15 mW was applied to the still stage, pushing its temperature up to 1.1 K. All the subsequent capacity calibrations started off from this baseline. Note that since the load curve was taken, numerous changes have been made to the 1 K and 100 mK stages, including additional vibration support from 4 K to 1 K, supports from 1 K to 100 mK, newly polished 100 mK thermal BUS with MLI tape applied, among other factors. These factors could affect the baseline measurements, and thus introduce additional errors to the calibration curve.

### 3.2.2 Cooldown and Pump Down Time

The cooldown time for each temperature stage changes with the configuration of the LATR. Intuitively, the more thermal mass we add and the more thermal loading we introduce, the longer the cooldown process will take. Currently, the most comprehensive test we have performed is the configuration with seven windows (and the corresponding filters at 300 K, 80 K, and 40 K) and seven optics tubes, representing the full nominal SO load-out.

During the cooldown, temperatures of different stages as a function of time were recorded. Figure 3.5 shows the cooldown curve from representative thermometers on

all temperature stages. As shown in the plot, it takes about 3 days to cool down with no optics tube, about 4 days to cool down with one optics tube, about 5 days to cool down with three optics tubes, and about 8 days to cool down with seven optics tubes. This is on-par with the cooldown time calculation discussed in Section 2.3.3, where thirteen optics tube were estimated to take less than 19 days to cool down.

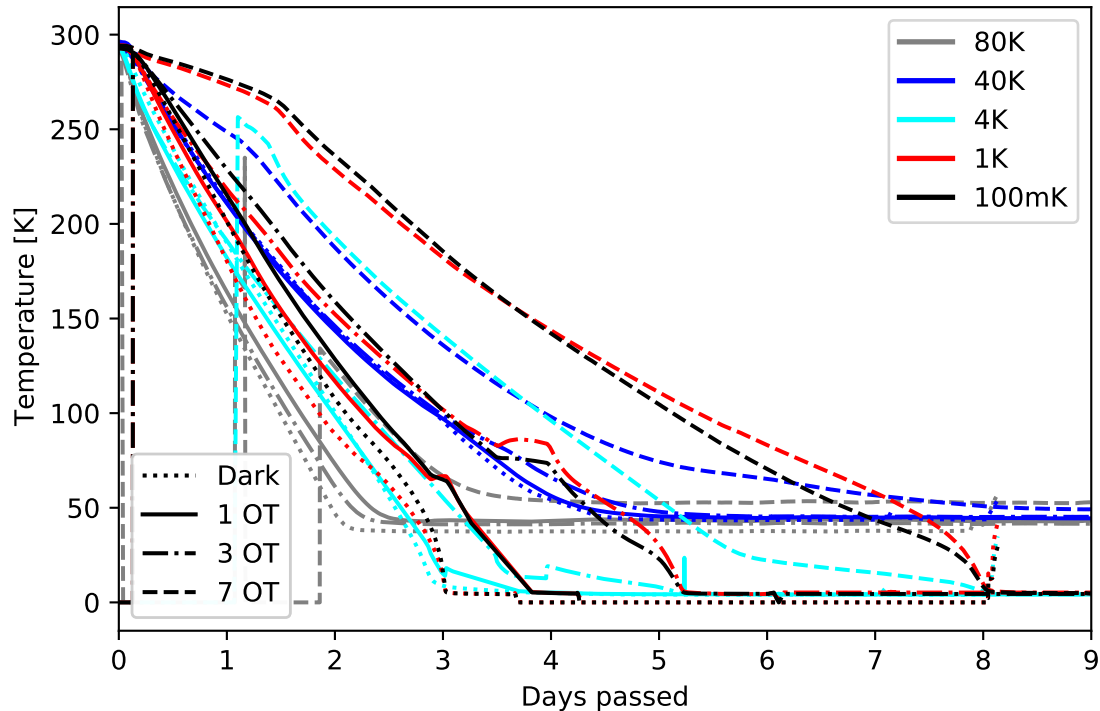


Figure 3.5: Cooldown curves at each temperature stage from a test run including seven optics tubes and seven optical windows (and filters). Although multiple thermometers are installed on each temperature stage, we only show one representative thermometer per stage. Dark cooldown is represented by dotted lines, one optics tube cooldown is shown as solid lines, three optics tube cooldown is shown as dotted-dash lines, and seven optics tube cooldown is shown as dashed lines. In the seven-tube configuration, the bulk of the cold stages at or above 4K reached their base temperatures within 8 days. The 1 K and 100 mK stages reached base temperatures within hours of the dilution refrigerator being turned on.

To evacuate the LATR, we initially pump with two Edwards<sup>2</sup> XDS35i roughing

<sup>2</sup>Edwards Vacuum, <https://www.edwardsvacuum.com/>

Temperature Stage	Cooldown Time	Plate/BUS Temperature	Thermal Gradient
80 K	4 days	59 K	$\pm 3$ K
40 K	8 days	52 K	$\pm 2$ K
4 K	8 days	5.2 K	$\pm 1.2$ K
1 K	8 days	1.0 K	$\pm 0.1$ K
100 mK	8 days	70 mK	$\pm 5$ mK

Table 3.4: Cooldown time measured in the three windows configuration with one optics tube installed. This is not to be confused with the simulated 13 optics tubes cooldown, which will take much longer due to added cold mass.

pumps through two KF40 flanges, one at the front of the cryostat and one at the back. This process takes about 1.5 to 2.5 days, depending on the humidity. We then reach high vacuum using an Edwards nEXT400 turbo pump bolted directly to an ISO 100 flange at the back of the LATR. Reaching high vacuum from rough vacuum takes about 4 hours, so that the whole process takes 2 to 3 days.

After the cryostat reached high vacuum, we turned on all five pulse tube coolers at the same time. In the seven tube configuration, the 80 K stage was able to reach its base temperature within 4 days and the 4 K stage was able to reach its base temperature within 8 days, as shown in Table 3.4. After the 4 K stage reached its base temperature, the DR began operating, cooling the 1 K and 100 mK stages to base temperatures within several hours. The 40 K stage, specifically the 40 K filter plate, reached base temperature in slightly longer than 8 days because it is the farthest from the PT420 cold heads (Figure 2.3). The observed cooldown times of the various stages with a 4K cold mass were expected and reflected the simulated performance. Also shown in Table 3.4 is the base temperature for each stage—measured either on the plate or on the BUS—along with the corresponding thermal gradient. The result shows that the passive and active heat switches worked as intended, and that the

overall cooldown strategy is sufficient.

### 3.2.3 Cryogenic Performance Validation

#### 80 K Stage

The cryogenic validation of the LATR proceeded in incremental steps, starting with the simplest configuration and gradually adding components. We first conducted 4 K dark tests, with two PT420s and two PT90s. Following completion of this test, we installed the Bluefors DR with the associated thermal straps that coupled the DR to the cryostat 4 K shell and the 1 K/100 mK thermal BUS. From the base temperatures in the dark tests, we backed out the loading on each stage using the cryogenic cooler load curves we calibrated during the preparation. These two rounds of dark tests provide a baseline loading without external radiation.

After the dark tests, we installed 300 K windows made out of 1/4" ultra high molecular weight polyethylene sheets. Behind each window, a double-sided infrared radiation (DSIR) filter at 300 K was installed on the back of the front plate to reflect out-of-band radiative power. Another DSIR filter was installed on the 80 K stage, followed by an AR coated alumina filter [58] also at 80 K. An example of the 80 K DSIR filter being installed is shown in Figure 3.6. The alumina filter absorbs the residual infrared radiation and conducts the heat away efficiently. It is machined to a wedge shape as an active optical component to bend the incoming light rays to be parallel to the cryostat central axis. After the alumina filter, another DSIR, at 40 K, reflects the residual infrared radiation before it enters the 40 K cavity. The 40 K cavity then houses the front part of the 13 optics tubes, including the filters and



lenses at 4 K and below (Figure 2.3). Prior to installing optics tubes, metal blanks with MLI were installed on the 4 K plate to block the radiation from the 40 K cavity.



Figure 3.6: In this picture, the cryostat is rotated to face downwards by 45 degrees to provide easy access to the front of the 80 K filter plate. Anna Kofman and Tanay Bhandarkar are installing the 80 K filters onto the 80 K filter plate. This installation has to be performed very carefully to avoid damaging the thin film filter.

We cryogenically tested the LATR with two windows installed (‘2-window’ configuration) and subsequently with three windows installed (‘3-window’ configuration). The ‘3-window’ configuration also had one optics tube and one URH installed. Given the overall progress of the project, initially we only fabricated three sets of the filters to give us enough fidelity to extrapolate the performance with all 13 windows installed.

Between the 80 K, 40 K, and 4 K stages, the 80 K is the most sensitive to radiation

Test Configuration	Filter Plate Temperature	Measured Loading	Predicted Loading
Dark	37 – 39 K	22 W	10.1 W
2-window	40 – 43 K	35 W	17.9 W
3-window	44 – 47 K	42 W	21.8 W
7-window	56 – 62 K	88 W	37.3 W
13-window*	82 – 92 K*	144 W*	60.6 W

Table 3.5: Base temperature and thermal loading for the 80 K stage under different configurations. The temperature range is measured from six thermometers evenly distributed on the 80 K filter plate. The starred values are extrapolated from measured results. The predicted load is derived from our thermal model in Table 2.3. The difference between the predicted loading and the measured loading is explained in the text.

loading because of the absorptive 80 K alumina filter. Measurements of the 80 K stage thermal loading under different configurations are summarized in Table 3.5. The baseline loading from the dark test is  $\sim 22$  W with each window adding another 7–9 W radiation loading on the 80 K stage. If we project the results to 13 windows, the anticipated loading will be  $\sim 144$  W. Given the load curve of the PT90s and thermal strap conductance, we calculate that the 80 K stage will stay at around 82 K $\sim$ 92 K. Because the 80 K filter plate is made of thermally-conductive aluminum 1100 series, the temperature gradient across the 2.1 m diameter plate measured  $\sim 6$  K with seven windows installed. Receiving slightly less than twice the loading with 13 optics tubes, the gradient may increase to  $\sim 10$  K, the same as the simulated value (Figure 2.20).

While the observed loading in Table 3.5 meets the LATR’s requirements, it is higher than the models predicted. In the dark configuration, this is likely due to two factors. The first factor is the imperfections of MLI. Considering the size of the 2.1 m diameter 80 K filter plate and the complicated geometry of the G-10 tabs, it is unsurprising to observe extra loading due to imperfect shielding of all the surfaces.

In addition, there is a second factor that MLI applied on the G-10 tabs also conducts heat from 300 K to 80 K. In the simulation, this effect was not included. Nevertheless, evidence from the 40 K stage MLI connection between the DR and 40 K shield suggests that the conductivity of the MLI is not negligible. In the window tests, we measured  $\sim 9$  W per filter set instead of the predicted  $\sim 3$  W. It is likely a result of higher-than-expected IR transmission of the 300 K DSIR filters and cross talk between windows. The simulation only calculates optical loading assuming each optics chain is an enclosed cylinder. In reality, each 80 K filter would not only see 300 K emission from the window on its optical path, but also radiation from the neighboring window. Another factor that should be considered is that all the measurements were performed when both of the pulse tube coolers were operating at  $< 50$  K, much lower than their nominal 80 K operation temperature. This is near the lower limit of the temperature the pulse tube coolers can reach, where only a sparsely-sampled calibration curve is available. This adds  $\mathcal{O}(1$  W)-level uncertainties in the measurements.

### **40 K and 4 K Stages**

During the dark test, the 40 K filter plate stayed at 44–47 K (measured at six locations on the plate) with an estimated loading of  $33 \pm 1$  W; the 4 K plate stayed at 3.5–5.2 K (measured at five locations on the plate) with an estimated loading of  $0.8 \pm 0.1$  W (Table 3.6). Estimating the thermal loading, especially on the 4 K stage, is challenging at these very low power levels where the calibration of the pulse tubes is less certain and thus results in a  $\sim 1$  W loading uncertainty on the 40 K stage and  $\sim 0.1$  W on the 4 K stage. To achieve a more accurate measurement, we installed seven heaters (evenly distributed) on the 4 K plate to add additional power

Test Configuration	Plate Temperature	Power	Predicted Loading
<b>40 K Filter Plate</b>			
Dark	44 – 47 K	$33_{-1}^{+1}$ W	35.3 W
2-window	44 – 47 K	< 33 W	35.3 W
3-window + 1-optics tube + 1-URH	46 – 49 K	< 34 W	38.8 W
7-window + 7-optics tube + 2-URH	50 – 55 K	< 51 W	42.4 W
<b>4 K Plate</b>			
Dark	3.5 – 5.2 K	$0.8_{-0.1}^{+0.1}$ W	0.42 W
2-window	3.6 – 5.0 K	$0.8_{-0.1}^{+0.2}$ W	0.47 W
3-window + 1-optics tube + 1-URH	3.8 – 5.2 K	$1.3_{-0.2}^{+0.2}$ W	0.75 W
7-window + 7-optics tube + 2-URH	4.0 – 6.4 K	$1.3_{-0.2}^{+0.2}$ W	1.05 W

Table 3.6: Base temperature and loading for the 40 K filter plate and the 4 K plate under different configurations, based on measurements at multiple locations. In the ‘dark’ configuration, the two calibrated PT420s cooled the 40 K and 4 K stages; starting from the ‘2-window’ configuration, the PT420 on the DR was thermally connected to the main cryostat in 40 K/4 K stages. We estimated contribution from the DR PT420 by comparing its temperatures in different configurations to the ones measured in its stand-alone cryostat. We used the average of the two calibrated PT420s and estimated the power given the temperature change on the 4 K stage. However, the DR PT420 40 K temperature decreased after it was installed in the main cryostat (being cooled by the other two PT420s), thus we report the number from the other two PT420s as upper limits. In the ‘3-window’ configuration, one optics tube and one URH were also installed in addition to three windows. In the ‘7-window’ configuration, seven optics tubes and two URHs were installed, representing the full initial deployment configuration.

and monitored the temperatures on the stage. From the data, we calculated the thermal conductance of the thermal straps connecting the pulse tube 4 K cold heads to the cryostat 4 K plate and then backed out what the thermal loading would be without additional loading from the heaters. This independent measurement gives results consistent with the those from the PT420 load curves.

After the DR was installed (starting from the ‘2-window’ configuration in Table 3.6), estimating thermal loading on the 40 K and 4 K stage became more difficult because the PT420 on the DR also contributed to the cooling of the 40 K and 4 K stages. We did not calibrate the PT420 in the DR since it is deeply integrated in the DR system. Furthermore, the conductivity of the thermal links between the DR 40 K/4 K stages and the main cryostat 40 K/4 K stages are hard to quantify. The DR and the cryostat 40 K stages are connected by aluminum coated mylar tape that is intended only for sealing the gaps between them to stop the light leak. The DR and the cryostat 4 K stages are connected by  $5 \times 10$ -stacked high-purity (99.999%) aluminum tabs. The aluminum tabs bridge the  $\sim 6$  mm gap, and have dimensions of  $0.5 \times 50 \times 75$  mm. We measured the 40 K and 4 K stage temperatures of the DR PT420 and compared to the values previously measured in its designated cryostat as a no-extra-load reference. The DR PT420 4 K temperature did not change in the ‘2-window’ configuration and rose by  $\sim 0.2$  K in the ‘3-window’ configuration, mainly because of the addition of the optics tube and the URH. Using the average of the calibrated load curves from the two PT420s, we estimated the additional cooling power due to the DR PT420, and thus the total loading from the observed temperature change. The thermal loading measurements are reported in Table 3.6.

Interestingly, the DR PT420 40 K temperature stage decreased after installation in

the LATR. This means that the main cryostat 40 K stage cools to a lower temperature than the DR 40 K stage so that it is ‘lending’ cooling power to the DR 40 K stage when thermally connected. Therefore, we report the 40 K thermal loading from the two calibrated PT420s as upper limits in Table 3.6.

The temperature gradient across the 2.06-m diameter 40 K filter plate is  $\leq 4$  K with three windows. From the ‘dark’ to the ‘3-window’ configuration, we did not measure significant changes on the 40 K filter plate in terms of thermal loading and thermal gradient. Based on that observation, the simulation is validated – showing the 40 K filter plate will not change significantly with a fully-equipped LATR, largely because only reflective filters are installed on this stage. Additionally, the 40 K stage of the URH measured  $\sim 50$  K, 4 K higher than the 40 K filter plate average. It is the warmest part of the 40 K stage since it is both far away from the pulse tube cold heads (Figure 2.25) and the source of significant thermal loading ( $\sim 7$  W for 4 URHs for the fully loaded configuration). The measured temperatures and the small thermal gradient proved that the pulse tube cooling power is efficiently distributed around the 2-m-long 40 K stage to maintain the entire stage below 50 K.

The thermal gradient across the 4 K plate is around 1.7 K in the ‘dark’ configuration, reduced to 1.4 K after the addition of the DR, and increased to 2.4 K with seven optics tube installed. The difference between the measured and predicted loading may come from the decreased fidelity of the simulation at the low-power limit. The addition of windows did not significantly change the loading on the 4 K which is consistent with the simulation. In the ‘3-window’ configuration, the temperature on the 4 K shell is  $\sim 5$  K, including the 4 K part of the URH. In the ‘7-window’ configuration, the temperature on the 4 K shell increased to 6 K–8 K. The second URH that is on

the opposite side of the pulse tubes is the hottest among all components, sitting at  $\sim 8.4$  K, while the rest of the components on the 4 K shell are all below 6.7 K. This measurement validates that the entire 4 K stage is efficiently cooled with seven windows, seven optics tube, and two URHs installed, and we see no evidence that the full complement of optics tubes will introduce unacceptable loading.

### **1 K and 100 mK Stage**

Enclosed within the 4 K cavity during dark test, the 100 mK thermal BUS cooled to  $< 50$  mK with the 1 K thermal BUS maintained at  $\sim 1$  K. Since we do not have 13 optics tubes during these tests, heaters were installed on both the 100 mK and 1 K thermal BUS to simulate thermal loads. With these two heaters, we were able to map out the load curve on the two stages which later informed our understanding of loading from the installed optics tubes. We also applied the anticipated loading from 13 optics tubes on the two stages, and the 100 mK thermal BUS reached  $\sim 100$  mK with  $\sim 10$  mK thermal gradient across its diameter, meeting the requirement.

Thermal loading on the 100 mK stage was increased by  $< 4 \mu\text{W}$  after installing one optics tube in the center position. With the amount of added power so small compared to the rest of the 100 mK structure, it is hard to obtain a more accurate loading value from a single optics tube. With the addition of active readout components and optical loading during operation, the total expected loading from one optics tube is  $\lesssim 5 \mu\text{W}$  [85; 39]. However, after installing the seven optics tube in the cryostat (shown in Figure 3.7), the total loading from the optics tube increased to  $\sim 50 \mu\text{W}$ . This could be potentially due to added DC cables installed in the seven-tube configuration that was not included in the one-tube setup. In the seven optics tube configuration, DR

mixing chamber temperature is 43.9 mK, thermal BUS temperature is  $\sim 70$  mK, and the optics tube focal plane temperature is 66 mK–75 mK. This proves that the DR cooling power and the thermal BUS system is more than sufficient for distributing power for seven optics tubes, the full initial deployment setup. At the mean time, the largest gradient across the focal plane module in different optics tubes meets the requirement at  $\lesssim 10$  mK.



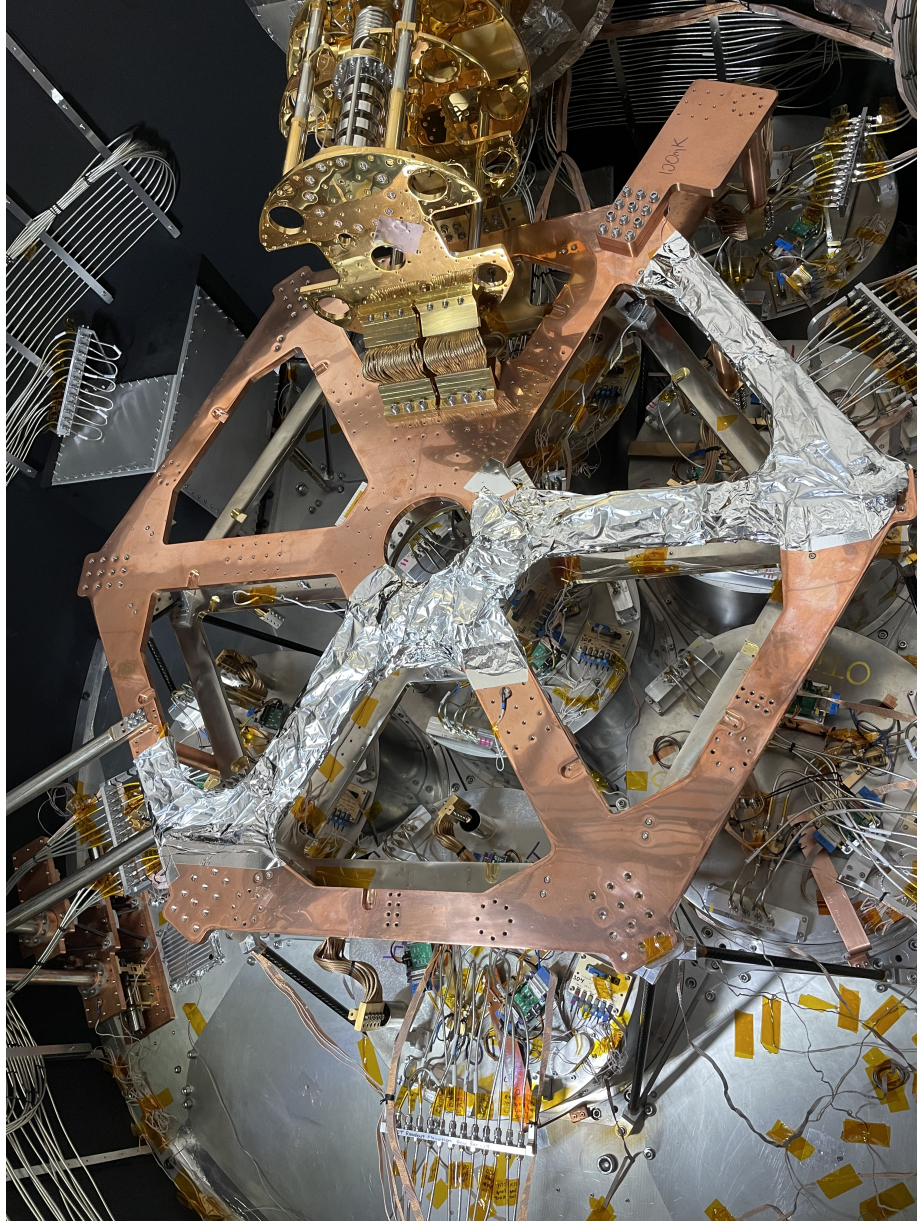


Figure 3.7: This picture shows the cryostat with seven optics tubes installed, representing the complete initial deployment configuration.

Extrapolating from this number, the estimated extra loading from thirteen optics tubes will be  $\sim 92 \mu\text{W}$ . With the additional  $25 \mu\text{W}$  parasitic loading, the total estimated loading on the 100 mK stage is  $117 \mu\text{W}$ . Based on the DR loading curve that we took in the dark configuration, this will raise the DR temperature to  $\sim 51 \text{ mK}$ . If we

linearly extrapolate the BUS to DR strap temperature gradient based on the power ratio, the hottest optics tube focal plane will reach  $\sim 105$  mK amongst the thirteen installed. Although this is more than enough for us to bias all the detectors, as 105 mK is well below the transition temperature, we would like to have more margin by pushing the focal plane temperature below 100 mK. Thus, we are investigating building additional heat straps between the thermal BUS and the DR in order to reduce the gradient by more than 10 mK in the 13 optics tube configuration.

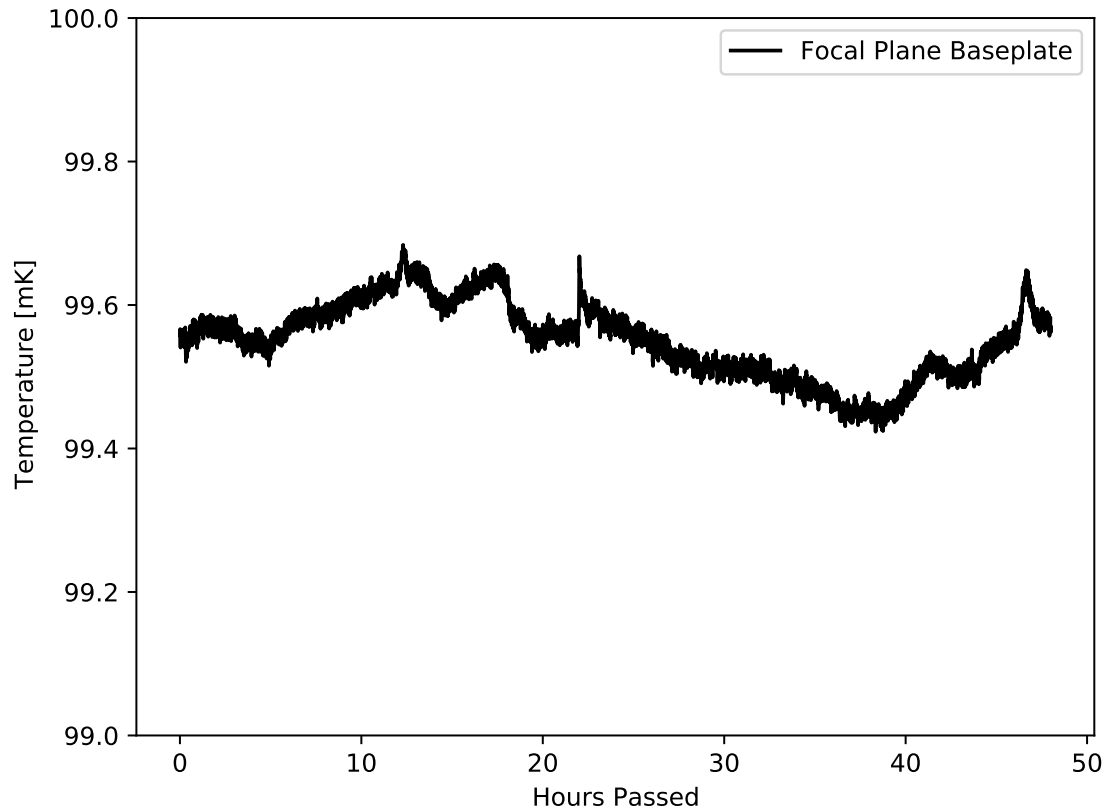


Figure 3.8: The temperature of an optics tube 100 mK stage over 48 hours. On this timescale, the optics tube focal plane stage temperature varies by  $\lesssim 0.3$  mK. At this level, bath temperature fluctuations will not meaningfully detract from overall detector stability.

After ensuring that the LATR would be able to thermally support 13 optics tubes,

we moved onto testing the thermal performance of the optics tubes themselves. In order to maintain the required thermal environment for the detector arrays, we needed to ensure that optics tube 100 mK stage had both long-term temperature stability and a negligible thermal gradient across the stage. Long-term temperature stability is important to detector performance, as bath temperature drifts can impact detector data quality. Consistent thermal bath temperature between adjacent detector arrays is also important to ensure the best quality of detector data. In Figure 3.8, we show how the temperature of one optics tube 100 mK stage changes over the course of 48 hours. Similar to the thermal tests described thus far, the optics tube was dark – with the 4K and 1K stages blanked-off. Constant power was applied to a heater near the DR to raise the temperature of the optics tube 100 mK stage to the fiducial operating temperature of  $\sim 100$  mK. As can be seen in Figure 3.8, the cold plate temperature varied by  $\lesssim 0.25$  mK over the (representative) 48 hour period. At this level, bath temperature fluctuations will have negligible impact on detector stability. The thermal gradient across the optics tube 100 mK stage was measured to be  $\lesssim 1$  mK at base temperature. A gradient this small means that adjacent detector arrays within a single optics tube will have negligible differences in bath temperature, preventing degradation of the detector data quality. Thus, these validation tests show that we have met the design requirements.

# Chapter 4

## Future Work

### 4.1 LATR Potential Upgrade

#### 4.1.1 Additional Cooling Power Consideration

Both the simulation and the cryogenic validation confirm that the LATR would perform to specification with 13 optics tubes installed, still, we include extra margin during the design phase to allow for future cooling capacity upgrade. As a result, LATR can accommodate an additional PT90 and an additional PT420 cooler if the need arises. Their respective vacuum shell locations are shown in Figure 4.1.

Inside the vacuum shell under the spare PT90 port, there is a bolt pattern on the 80 K filter plate to accommodate the heat strap for the additional pulse tube. If lower 80 K filter plate temperature is desired for a fully loaded cryostat, it is very straight forward to design the heat strap connecting the additional PT90 to the 80 K filter plate. Moreover, the design of the lifting mechanism (shown in Figure 2.30) and the turbo rack mount (shown in Figure 2.2) takes this upgrade into consideration,

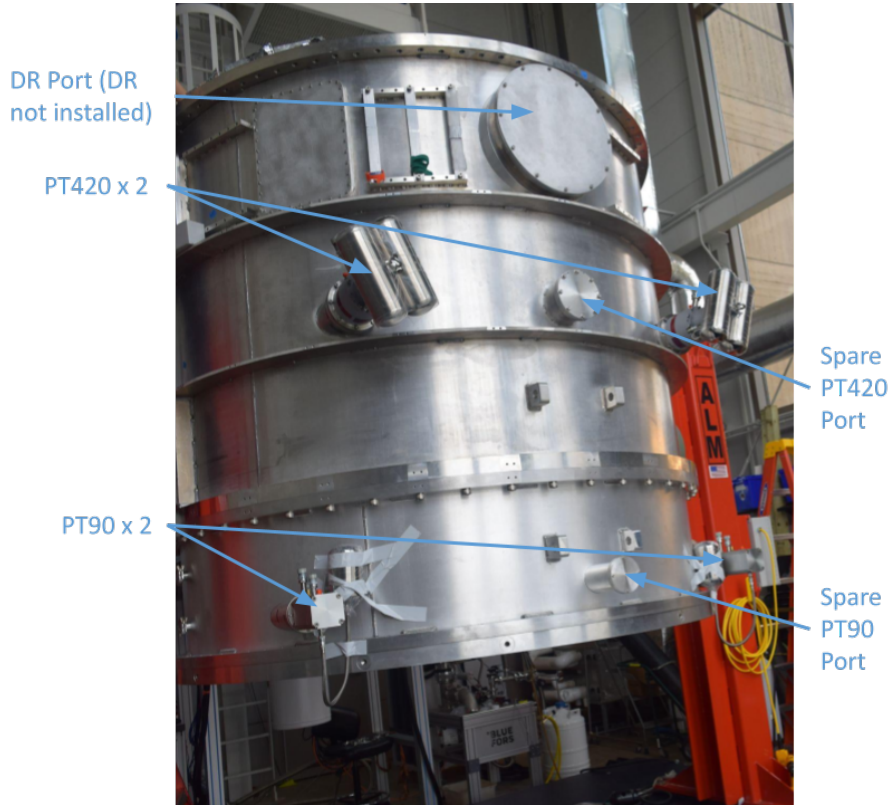


Figure 4.1: This picture shows two PT420 and two PT90 installed. If needed for future upgrade, the LATR has two spare ports for one additional PT420 and one additional PT90.

and avoids interference with the pulse tube body. Thus no major alteration to the cryostat warm component is required.

The spare PT420, on the other hand, would take a lot more careful planning to be implemented. Similar to the PT90, the spare PT420 also has corresponding bolt patterns on 40 K shield, 4 K shield, and 4 K plate to receive it. Although harder than the PT90 where there is only a single stage, design for the additional PT420 thermal strap can borrow heavily from the existing PT420 straps. However, the lifting mechanism (shown in Figure 2.30) as manufactured would interfere with the spare PT420, even with the remote-motor configuration. The location of the spare PT-420

tube is very close to the crane hook location, as it is near the center of gravity of the cryostat. As such, the PT420 cannot be installed if the lifting mechanism is used as is. One potential method of making room for the spare PT420 is to measure the actual receiver cabin crane height on the LAT, increase the link length between the lifter and the cryostat according to the measurement, and then check if the additional space is enough for the remote-motor mounted PT420. This way, the warm component alteration can be kept to a minimum. Naturally, other consideration including LAT electrical and water cooling capacity needs to be examined before this addition can take place. But those considerations are beyond the scope of this thesis.

#### **4.1.2 Additional Thermal Strap Consideration**

During cryogenic validation testing, we installed additional heat straps on the 40 K shield. If needed, other action can be taken to improve the temperature gradient at the 40 K stage, 4 K stage, 1 K stage, and 100 K stage.

If the gradient on the 40 K stage becomes a concern with a fully loaded cryostat, the easiest solution would be to replace the 5N aluminum straps with thicker straps, so as to increase their conductivity. If these improvements are insufficient, the 40 K heat straps installed on the PT420 40 K stage contain additional bolt pattern to allow for additional attachment to the LATR 40 K shell. The 4 K plate, as shown in Figure 2.11, is designed with two cutouts, such that one can also add additional aluminum bars directly between the 40 K heat straps and the 40 K filter plate. Accordingly, there are also bolt patterns on the 40 K plate that can accommodate this addition. Due to the MLI installed on the 40 K shield, it is preferred that the 40 K shield not to be taken out and replaced. But as a last resort to address unforeseen loading issue, or to

resolve a catastrophic failure during transportation, 40 K shield can be redesigned to have twice the thickness as designed, and halves the temperature gradient between the PT connection and the 40 K filter plate.

If the gradient on the 4 K stage needs to be reduced, there are bolt patterns on the 4 K shield near the URH attachment plate where additional straps can be added to reduce the temperature gradient between the URH and the 4 K shield. Additional straps can also be installed across different URHs. It would be hard to improve the PT420 4 K strap connection to the cryostat 4 K plate due to tight space constraint. But it is possible to increase the conductivity between DR 4 K strap to the cryostat 4 K shield to help reduce its gradient.

To reduce the gradient on 1 K and 100 mK stages, three approaches can be considered. The first one would be improving the existing thermal strap between the DR and the 1 K or 100 mK BUS. To achieve this, one can either design new straps, or reinforce existing one with copper shim stock. The second method is to improve the conductivity of the thermal BUS, by either building a more conductive BUS, or reinforcing existing BUS with copper blocks. The third method is to improve mechanical insulation, by installing thermal insulators between 4 K and 1 K stage, or between the 1 K and 100 K stage on the BUS, in the optics tubes, or in the cables. Depending on the heat source, one can add insulating spacers on the BUS or in the optics tubes to reduce the conductive load between stages, replace the existing insulating structure with less conductive ones, or add additional mechanical break in the cables to have better heat sink at the intermediate stages.

# Chapter 5

## Conclusion

Simons Observatory Large Aperture Telescope and its receiver were designed and built based on a series of science goals outlined in the Simons Observatory forecast paper [79]. A few of the major science goals are discussed in detail in Chapter 1 as an illustration of the measurements that the Large Aperture Telescope Receiver (LATR) will be capable of performing. Throughout the thesis, we presented the detailed design, construction, and integration of the LATR, as well as various mechanical and cryogenic tests conducted in the cryostat. The results presented here proved that we have met or exceeded the numerous requirements that were imposed on this instrument, and have reached the goals that were set five years ago.

For the next step the LATR is scheduled to be transported to and deployed in Chile in 2022. It will first undergo a series of telescope integration effort to verify its performance and to check that all the interfaces work properly. After finishing integration, it will see the first light. Following the start of observation, a series of analysis effort will ensue, producing the science results that were promised in the



proposals, and hopefully making many more unexpected discoveries along the way. I will be looking forward to that day with great anticipation and excitement.

# Appendix A: List of Acronyms

ABS	Atacama B-mode Survey.
ACT	Atacama Cosmology Telescope.
AR	Anti-reflection.
BAO	Baryon Acoustic Oscillation.
BICEP	Background Imaging of Cosmic Extragalactic Polarization.
BUS	Back-up Structure.
CAD	Computer Aided Design.
CLASS	Cosmology Large Angular Scale Surveyor.
CMB	Cosmic Microwave Background.
COBE	Cosmic Background Explorer.
CuNi	CuproNickel.
DC	Direct Current.
DESI	Dark Energy Spectroscopic Instrument.

DR	Dilution Refrigerator.
DSIR	Double-sided Infrared.
FEA	Finite Element Analysis.
FoS	Factor of Safety.
FOV	Field of View.
GM	Gifford-McMahon.
IR	Infrared Radiation.
ISW	Integrated Sachs-Wolfe.
LAT	Large Aperture Telescope.
LATR	Large Aperture Telescope Receiver.
LF	Low-frequency.
LNA	Low Noise Amplifiers.
LNF	Low Noise Factory.
LPE	Low-pass Edge.
MF	Mid-frequency.
MLI	Multi-layer Insulation.
NbTi	Niobium Titanium.

OCS     Observatory Control System.

OFHC    Oxygen-Free High-purity Copper.

PT       Pulse Tube.

RF       Radio Frequency.

ROX     Ruthenium Oxide.

SAT      Small Aperture Telescope.

SO       Simons Observatory.

SPT      South Pole Telescope.

SZ       Sunyaev-Zel'dovich.

TES      Transition Edge Sensor.

UFM      Universal Focal-plane Module.

UHF      Ultra-high-frequency.

URH      Universal Readout Harness.

WMAP    Wilkinson Microwave Anisotropy Probe.

# Bibliography

- [1] K. Abazajian, G. Addison, P. Adshead, Z. Ahmed, S. W. Allen, D. Alonso, M. Alvarez, A. Anderson, K. S. Arnold, C. Baccigalupi, K. Bailey, D. Barkats, D. Barron, P. S. Barry, J. G. Bartlett, R. B. Thakur, N. Battaglia, E. Baxter, R. Bean, C. Bebek, A. N. Bender, B. A. Benson, E. Berger, S. Bhimani, C. A. Bischoff, L. Bleem, S. Bocquet, K. Boddy, M. Bonato, J. R. Bond, J. Borrill, F. R. Bouchet, M. L. Brown, S. Bryan, B. Burkhart, V. Buza, K. Byrum, E. Calabrese, V. Calafut, R. Caldwell, J. E. Carlstrom, J. Carron, T. Cecil, A. Challinor, C. L. Chang, Y. Chinone, H.-M. S. Cho, A. Cooray, T. M. Crawford, A. Crites, A. Cukierman, F.-Y. Cyr-Racine, T. de Haan, G. de Zotti, J. Delabrouille, M. Demarteau, M. Devlin, E. D. Valentino, M. Dobbs, S. Duff, A. Duivenvoorden, C. Dvorkin, W. Edwards, J. Eimer, J. Errard, T. Essinger-Hileman, G. Fabbian, C. Feng, S. Ferraro, J. P. Filippini, R. Flauger, B. Flaugher, A. A. Fraisse, A. Frolov, N. Galitzki, S. Galli, K. Ganga, M. Gerbino, M. Gilchriese, V. Gluscevic, D. Green, D. Grin, E. Grohs, R. Gualtieri, V. Guarino, J. E. Gudmundsson, S. Habib, G. Haller, M. Halpern, N. W. Halverson, S. Hanany, K. Harrington, M. Hasegawa, M. Hasselfield, M. Hazumi, K. Heitmann, S. Henderson, J. W. Henning, J. C. Hill, R. Hlozek, G. Holder, W. Holzzapfel, J. Hubmayr, K. M.

Huffenberger, M. Huffer, H. Hui, K. Irwin, B. R. Johnson, D. Johnstone, W. C. Jones, K. Karkare, N. Katayama, J. Kerby, S. Kernovsky, R. Keskitalo, T. Kisner, L. Knox, A. Kosowsky, J. Kovac, E. D. Kovetz, S. Kuhlmann, C. lin Kuo, N. Kurita, A. Kusaka, A. Lahteenmaki, C. R. Lawrence, A. T. Lee, A. Lewis, D. Li, E. Linder, M. Loverde, A. Lowitz, M. S. Madhavacheril, A. Mantz, F. Matsuda, P. Mauskopf, J. McMahon, M. McQuinn, P. D. Meerburg, J.-B. Melin, J. Meyers, M. Millea, J. Mohr, L. Moncelsi, T. Mroczkowski, S. Mukherjee, M. Münchmeyer, D. Nagai, J. Nagy, T. Namikawa, F. Nati, T. Natoli, M. Negrello, L. Newburgh, M. D. Niemack, H. Nishino, M. Nordby, V. Novosad, P. O'Connor, G. Obied, S. Padin, S. Pandey, B. Partridge, E. Pierpaoli, L. Pogosian, C. Pryke, G. Puglisi, B. Racine, S. Raghunathan, A. Rahlin, S. Rajagopalan, M. Raveri, M. Reichanadter, C. L. Reichardt, M. Remazeilles, G. Rocha, N. A. Roe, A. Roy, J. Ruhl, M. Salatino, B. Saliwanchik, E. Schaan, A. Schillaci, M. M. Schmittfull, D. Scott, N. Sehgal, S. Shandera, C. Sheehy, B. D. Sherwin, E. Shirokoff, S. M. Simon, A. Slosar, R. Somerville, D. Spergel, S. T. Staggs, A. Stark, R. Stompor, K. T. Story, C. Stoughton, A. Suzuki, O. Tajima, G. P. Teply, K. Thompson, P. Timbie, M. Tomasi, J. I. Treu, M. Tristram, G. Tucker, C. Umiltà, A. van Engelen, J. D. Vieira, A. G. Vieregg, M. Vogelsberger, G. Wang, S. Watson, M. White, N. Whitehorn, E. J. Wollack, W. L. K. Wu, Z. Xu, S. Yasini, J. Yeck, K. W. Yoon, E. Young, and A. Zonca. Cmb-s4 science case, reference design, and project plan, 2019.

- [2] K. N. Abazajian, P. Adshead, Z. Ahmed, S. W. Allen, D. Alonso, K. S. Arnold, C. Baccigalupi, J. G. Bartlett, N. Battaglia, B. A. Benson, C. A. Bischoff,

J. Borrill, V. Buza, E. Calabrese, R. Caldwell, J. E. Carlstrom, C. L. Chang, T. M. Crawford, F.-Y. Cyr-Racine, F. De Bernardis, T. de Haan, S. di Serego Alighieri, J. Dunkley, C. Dvorkin, J. Errard, G. Fabbian, S. Feeney, S. Ferraro, J. P. Filippini, R. Flauger, G. M. Fuller, V. Gluscevic, D. Green, D. Grin, E. Grohs, J. W. Henning, J. C. Hill, R. Hlozek, G. Holder, W. Holzappel, W. Hu, K. M. Huffenberger, R. Keskitalo, L. Knox, A. Kosowsky, J. Kovac, E. D. Kovetz, C.-L. Kuo, A. Kusaka, M. Le Jeune, A. T. Lee, M. Lilley, M. Loverde, M. S. Madhavacheril, A. Mantz, D. J. E. Marsh, J. McMahon, P. D. Meerburg, J. Meyers, A. D. Miller, J. B. Munoz, H. N. Nguyen, M. D. Niemack, M. Peloso, J. Peloton, L. Pogosian, C. Pryke, M. Raveri, C. L. Reichardt, G. Rocha, A. Rotti, E. Schaan, M. M. Schmittfull, D. Scott, N. Sehgal, S. Shandera, B. D. Sherwin, T. L. Smith, L. Sorbo, G. D. Starkman, K. T. Story, A. van Engelen, J. D. Vieira, S. Watson, N. Whitehorn, and W. L. Kimmy Wu. CMB-S4 Science Book, First Edition. *arXiv*, art. arXiv:1610.02743, Oct. 2016.

[3] P. Ade, R. Aikin, D. Barkats, S. Benton, C. Bischoff, J. Bock, J. Brevik, I. Buder, E. Bullock, C. Dowell, and et al. Detection of b-mode polarization at degree angular scales by bicep2. *PhRvL*, 112(24):241101, Jun 2014. ISSN 1079-7114. doi: 10.1103/physrevlett.112.241101. URL <http://dx.doi.org/10.1103/PhysRevLett.112.241101>.

[4] P. Ade, Y. Akiba, A. Anthony, K. Arnold, M. Atlas, D. Barron, D. Boettger, J. Borrill, S. Chapman, Y. Chinone, and et al. Measurement of the cosmic microwave background polarization lensing power spectrum with the polarbear experiment. *Physical Review Letters*, 113(2):021301, Jul 2014. ISSN 1079-

7114. doi: 10.1103/physrevlett.113.021301. URL <http://dx.doi.org/10.1103/PhysRevLett.113.021301>.

- [5] P. Ade, Z. Ahmed, M. Amiri, A. Anderson, J. Austermann, J. Avva, D. Barkats, R. B. Thakur, J. Beall, A. Bender, and et al. A demonstration of improved constraints on primordial gravitational waves with delensing. *PhRvD*, 103(2): 022004, Jan 2021. ISSN 2470-0029. doi: 10.1103/physrevd.103.022004. URL <http://dx.doi.org/10.1103/PhysRevD.103.022004>.
- [6] P. A. R. Ade, G. Pisano, C. Tucker, and S. Weaver. A review of metal mesh filters. In *SPIE*, volume 6275 of *Society of Photo-Optical Instrumentation Engineers (SPIE) Conference Series*, page 62750U, June 2006. doi: 10.1117/12.673162.
- [7] S. Aiola, E. Calabrese, L. Maurin, S. Naess, B. L. Schmitt, M. H. Abitbol, G. E. Addison, P. A. R. Ade, D. Alonso, M. Amiri, S. Amodeo, E. Angile, J. E. Austermann, T. Baildon, N. Battaglia, J. A. Beall, R. Bean, D. T. Becker, J. R. Bond, S. M. Bruno, V. Calafut, L. E. Campusano, F. Carrero, G. E. Chesmore, H. mei Cho, S. K. Choi, S. E. Clark, N. F. Cothard, D. Crichton, K. T. Crowley, O. Darwish, R. Datta, E. V. Denison, M. J. Devlin, C. J. Duell, S. M. Duff, A. J. Duivenvoorden, J. Dunkley, R. Dünner, T. Essinger-Hileman, M. Fankhanel, S. Ferraro, A. E. Fox, B. Fuzia, P. A. Gallardo, V. Gluscevic, J. E. Golec, E. Grace, M. Gralla, Y. Guan, K. Hall, M. Halpern, D. Han, P. Hargrave, M. Hasselfield, J. M. Helton, S. Henderson, B. Hensley, J. C. Hill, G. C. Hilton, M. Hilton, A. D. Hincks, R. Hlozek, S.-P. P. Ho, J. Hubmayr, K. M. Huffman, J. P. Hughes, L. Infante, K. Irwin, R. Jackson, J. Klein, K. Knowles, B. Koopman, A. Kosowsky, V. Lakey, D. Li, Y. Li, Z. Li, M. Lokken, T. Louis, M. Lungu, A. MacInnis,



M. Madhavacheril, F. Maldonado, M. Mallaby-Kay, D. Marsden, J. McMahon, F. Menanteau, K. Moodley, T. Morton, T. Namikawa, F. Nati, L. Newburgh, J. P. Nibarger, A. Nicola, M. D. Niemack, M. R. Nolta, J. Orłowski-Sherer, L. A. Page, C. G. Pappas, B. Partridge, P. Phakathi, G. Pisano, H. Prince, R. Puddu, F. J. Qu, J. Rivera, N. Robertson, F. Rojas, M. Salatino, E. Schaan, A. Schillaci, N. Sehgal, B. D. Sherwin, C. Sierra, J. Sievers, C. Sifon, P. Sikhosana, S. Simon, D. N. Spergel, S. T. Staggs, J. Stevens, E. Storer, D. D. Sunder, E. R. Switzer, B. Thorne, R. Thornton, H. Trac, J. Treu, C. Tucker, L. R. Vale, A. V. Engelen, J. V. Lanen, E. M. Vavagiakis, K. Wagoner, Y. Wang, J. T. Ward, E. J. Wollack, Z. Xu, F. Zago, and N. Zhu. The atacama cosmology telescope: DR4 maps and cosmological parameters. *Journal of Cosmology and Astroparticle Physics*, 2020(12):047–047, dec 2020. doi: 10.1088/1475-7516/2020/12/047. URL <https://doi.org/10.1088/1475-7516/2020/12/047>.

- [8] C. Alduino, F. Alessandria, M. Balata, D. Biare, M. Biassoni, C. Bucci, A. Caminata, L. Canonica, L. Cappelli, G. Ceruti, A. Chiarini, N. Chott, M. Clemenza, S. Copello, A. Corsi, O. Cremonesi, A. D’Addabbo, S. Dell’Oro, L. D. Paolo, M. D. Vacri, A. Drobizhev, M. Faverzani, E. Ferri, M. Franceschi, R. Gaigher, L. Gladstone, P. Gorla, M. Guetti, L. Ioannucci, Y. Kolomensky, C. Ligi, L. Marini, T. Napolitano, S. Nisi, A. Nucciotti, I. Nutini, T. O’Donnell, D. Orlandi, J. Ouellet, C. Pagliarone, L. Pattavina, A. Pelosi, M. Perego, E. Previtali, B. Romualdi, A. Rotilio, C. Rusconi, D. Santone, V. Singh, M. Sisti, L. Taffarello, E. Tatananni, F. Terranova, S. Wagaarachchi, J. Wallig, and C. Zarra. The cuore cryostat: An infrastructure for rare

- event searches at millikelvin temperatures. *Cryo*, 102:9 – 21, 2019. ISSN 0011-2275. doi: <https://doi.org/10.1016/j.cryogenics.2019.06.011>. URL <http://www.sciencedirect.com/science/article/pii/S0011227519301031>.
- [9] A. M. Ali, S. Adachi, K. Arnold, P. Ashton, A. Bazarko, Y. Chinone, G. Coppi, L. Corbett, K. D. Crowley, K. T. Crowley, M. Devlin, S. Dicker, S. Duff, C. Ellis, N. Galitzki, N. Goeckner-Wald, K. Harrington, E. Healy, C. A. Hill, S.-P. P. Ho, J. Hubmayr, B. Keating, K. Kiuchi, A. Kusaka, A. T. Lee, M. Ludlam, A. Mangu, F. Matsuda, H. McCarrick, F. Nati, M. D. Niemack, H. Nishino, J. Orłowski-Scherer, M. Sathyanarayana Rao, C. Raum, Y. Sakurai, M. Salatino, T. Sasse, J. Seibert, C. Sierra, M. Silva-Feaver, J. Spisak, S. M. Simon, S. Staggs, O. Tajima, G. Teply, T. Tsan, E. Wollack, B. Westbrook, Z. Xu, M. Zannoni, and N. Zhu. Small Aperture Telescopes for the Simons Observatory. *JLTP*, 200(5):461 – 471, Apr. 2020. doi: 10.1007/s10909-020-02430-5.
- [10] E. J. Baxter, C. H. Blake, and B. Jain. Probing oort clouds around milky way stars with cmb surveys. *The Astronomical Journal*, 156(5):243, Nov 2018. ISSN 1538-3881. doi: 10.3847/1538-3881/aae64e. URL <http://dx.doi.org/10.3847/1538-3881/aae64e>.
- [11] C. L. Bennett, D. Larson, J. L. Weiland, N. Jarosik, G. Hinshaw, N. Odegard, K. M. Smith, R. S. Hill, B. Gold, M. Halpern, E. Komatsu, M. R. Nolte, L. Page, D. N. Spergel, E. Wollack, J. Dunkley, A. Kogut, M. Limon, S. S. Meyer, G. S. Tucker, and E. L. Wright. NINE-YEAR WILKINSON MICROWAVE ANISOTROPY PROBE ( WMAP ) OBSERVATIONS: FINAL MAPS AND

RESULTS. *ApJS*, 208(2):20, sep 2013. doi: 10.1088/0067-0049/208/2/20. URL <https://doi.org/10.1088/0067-0049/208/2/20>.

- [12] C. Blake, E. Baxter, and B. Jain. Probing Oort clouds around Milky Way stars with CMB surveys. In *2019AAS 233*, volume 233 of *American Astronomical Society Meeting Abstracts*, page 302.06, Jan. 2019.
- [13] J. E. Carlstrom, P. A. R. Ade, K. A. Aird, B. A. Benson, L. E. Bleem, S. Busetti, C. L. Chang, E. Chauvin, H.-M. Cho, T. M. Crawford, A. T. Crites, M. A. Dobbs, N. W. Halverson, S. Heimsath, W. L. Holzapfel, J. D. Hrubes, M. Joy, R. Keisler, T. M. Lanting, A. T. Lee, E. M. Leitch, J. Leong, W. Lu, M. Lueker, D. Luong-Van, J. J. McMahon, J. Mehl, S. S. Meyer, J. J. Mohr, T. E. Montroy, S. Padin, T. Plagge, C. Pryke, J. E. Ruhl, K. K. Schaffer, D. Schwan, E. Shirokoff, H. G. Spieler, Z. Staniszewski, A. A. Stark, C. Tucker, K. Vanderlinde, J. D. Vieira, and R. Williamson. The 10 meter south pole telescope. *PASP*, 123(903):568–581, may 2011. doi: 10.1086/659879. URL <https://doi.org/10.1086/659879>.
- [14] Željko Ivezić, S. M. Kahn, J. A. Tyson, B. Abel, E. Acosta, R. Allsman, D. Alonso, Y. AlSayyad, S. F. Anderson, J. Andrew, J. R. P. Angel, G. Z. Angeli, R. Ansari, P. Antilogus, C. Araujo, R. Armstrong, K. T. Arndt, P. Astier, É. Aubourg, N. Auza, T. S. Axelrod, D. J. Bard, J. D. Barr, A. Barrau, J. G. Bartlett, A. E. Bauer, B. J. Bauman, S. Baumont, E. Bechtol, K. Bechtol, A. C. Becker, J. Becla, C. Beldica, S. Bellavia, F. B. Bianco, R. Biswas, G. Blanc, J. Blazek, R. D. Blandford, J. S. Bloom, J. Bogart, T. W. Bond, M. T. Booth, A. W. Borgland, K. Borne, J. F. Bosch, D. Boutigny, C. A. Brackett, A. Bradshaw, W. N. Brandt, M. E. Brown, J. S. Bullock, P. Burchat, D. L. Burke, G. Cagnoli, D. Cal-

abrese, S. Callahan, A. L. Callen, J. L. Carlin, E. L. Carlson, S. Chandrasekharan, G. Charles-Emerson, S. Chesley, E. C. Cheu, H.-F. Chiang, J. Chiang, C. Chirino, D. Chow, D. R. Ciardi, C. F. Claver, J. Cohen-Tanugi, J. J. Cockrum, R. Coles, A. J. Connolly, K. H. Cook, A. Cooray, K. R. Covey, C. Cribbs, W. Cui, R. Cutri, P. N. Daly, S. F. Daniel, F. Daruich, G. Daubard, G. Daues, W. Dawson, F. Delgado, A. Dellapenna, R. de Peyster, M. de Val-Borro, S. W. Digel, P. Doherty, R. Dubois, G. P. Dubois-Felsmann, J. Durech, F. Economou, T. Eifler, M. Eracleous, B. L. Emmons, A. F. Neto, H. Ferguson, E. Figueroa, M. Fisher-Levine, W. Focke, M. D. Foss, J. Frank, M. D. Freemon, E. Gangler, E. Gawiser, J. C. Geary, P. Gee, M. Geha, C. J. B. Gessner, R. R. Gibson, D. K. Gilmore, T. Glanzman, W. Glick, T. Goldina, D. A. Goldstein, I. Goodenow, M. L. Graham, W. J. Gressler, P. Gris, L. P. Guy, A. Guyonnet, G. Haller, R. Harris, P. A. Hascall, J. Haupt, F. Hernandez, S. Herrmann, E. Hileman, J. Hoblitt, J. A. Hodgson, C. Hogan, J. D. Howard, D. Huang, M. E. Huffer, P. Ingraham, W. R. Innes, S. H. Jacoby, B. Jain, F. Jammes, J. Jee, T. Jenness, G. Jernigan, D. Jevremović, K. Johns, A. S. Johnson, M. W. G. Johnson, R. L. Jones, C. Juramy-Gilles, M. Jurić, J. S. Kalirai, N. J. Kallivayalil, B. Kalmbach, J. P. Kantor, P. Karst, M. M. Kasliwal, H. Kelly, R. Kessler, V. Kinnison, D. Kirkby, L. Knox, I. V. Kotov, V. L. Krabbendam, K. S. Krughoff, P. Kubánek, J. Kuczewski, S. Kulkarni, J. Ku, N. R. Kurita, C. S. Lage, R. Lambert, T. Lange, J. B. Langton, L. L. Guillou, D. Levine, M. Liang, K.-T. Lim, C. J. Lintott, K. E. Long, M. Lopez, P. J. Lotz, R. H. Lupton, N. B. Lust, L. A. MacArthur, A. Mahabal, R. Mandelbaum, T. W. Markiewicz, D. S. Marsh, P. J. Marshall, S. Marshall, M. May, R. McKercher, M. McQueen, J. Meyers, M. Migliore, M. Miller, D. J. Mills,

C. Miraval, J. Moeyens, F. E. Moolekamp, D. G. Monet, M. Moniez, S. Monke-  
witz, C. Montgomery, C. B. Morrison, F. Mueller, G. P. Muller, F. M. Arancibia,  
D. R. Neill, S. P. Newbry, J.-Y. Nief, A. Nomerotski, M. Nordby, P. O'Connor,  
J. Oliver, S. S. Olivier, K. Olsen, W. O'Mullane, S. Ortiz, S. Osier, R. E. Owen,  
R. Pain, P. E. Palecek, J. K. Parejko, J. B. Parsons, N. M. Pease, J. M. Peterson,  
J. R. Peterson, D. L. Petravick, M. E. L. Petrick, C. E. Petry, F. Pierfederici,  
S. Pietrowicz, R. Pike, P. A. Pinto, R. Plante, S. Plate, J. P. Plutchak, P. A.  
Price, M. Prouza, V. Radeka, J. Rajagopal, A. P. Rasmussen, N. Regnault, K. A.  
Reil, D. J. Reiss, M. A. Reuter, S. T. Ridgway, V. J. Riot, S. Ritz, S. Robin-  
son, W. Roby, A. Roodman, W. Rosing, C. Roucelle, M. R. Rumore, S. Russo,  
A. Saha, B. Sassolas, T. L. Schalk, P. Schellart, R. H. Schindler, S. Schmidt, D. P.  
Schneider, M. D. Schneider, W. Schoening, G. Schumacher, M. E. Schwamb,  
J. Sebag, B. Selvy, G. H. Sembroski, L. G. Seppala, A. Serio, E. Serrano, R. A.  
Shaw, I. Shipsey, J. Sick, N. Silvestri, C. T. Slater, J. A. Smith, R. C. Smith,  
S. Sobhani, C. Soldahl, L. Storrie-Lombardi, E. Stover, M. A. Strauss, R. A.  
Street, C. W. Stubbs, I. S. Sullivan, D. Sweeney, J. D. Swinbank, A. Szalay,  
P. Takacs, S. A. Tether, J. J. Thaler, J. G. Thayer, S. Thomas, A. J. Thornton,  
V. Thukral, J. Tice, D. E. Trilling, M. Turri, R. V. Berg, D. V. Berk, K. Vet-  
ter, F. Virieux, T. Vucina, W. Wahl, L. Walkowicz, B. Walsh, C. W. Walter,  
D. L. Wang, S.-Y. Wang, M. Warner, O. Wiecha, B. Willman, S. E. Winters,  
D. Wittman, S. C. Wolff, W. M. Wood-Vasey, X. Wu, B. Xin, P. Yoachim, and  
H. Zhan. LSST: From science drivers to reference design and anticipated data  
products. *ApJ*, 873(2):111, mar 2019. doi: 10.3847/1538-4357/ab042c. URL  
<https://doi.org/10.3847/1538-4357/ab042c>.

- [15] S. K. Choi, M. Hasselfield, S.-P. P. Ho, B. Koopman, M. Lungu, M. H. Abitbol, G. E. Addison, P. A. R. Ade, S. Aiola, D. Alonso, M. Amiri, S. Amodeo, E. Angile, J. E. Austermann, T. Baidon, N. Battaglia, J. A. Beall, R. Bean, D. T. Becker, J. R. Bond, S. M. Bruno, E. Calabrese, V. Calafut, L. E. Campusano, F. Carrero, G. E. Chesmore, H. mei Cho, S. E. Clark, N. F. Cothard, D. Crichton, K. T. Crowley, O. Darwish, R. Datta, E. V. Denison, M. J. Devlin, C. J. Duell, S. M. Duff, A. J. Duivenvoorden, J. Dunkley, R. Dünner, T. Essinger-Hileman, M. Fankhanel, S. Ferraro, A. E. Fox, B. Fuzia, P. A. Gallardo, V. Gluscevic, J. E. Golec, E. Grace, M. Gralla, Y. Guan, K. Hall, M. Halpern, D. Han, P. Hargrave, S. Henderson, B. Hensley, J. C. Hill, G. C. Hilton, M. Hilton, A. D. Hincks, R. Hlozek, J. Hubmayr, K. M. Huffenberger, J. P. Hughes, L. Infante, K. Irwin, R. Jackson, J. Klein, K. Knowles, A. Kosowsky, V. Lakey, D. Li, Y. Li, Z. Li, M. Lokken, T. Louis, A. MacInnis, M. Madhavacheril, F. Maldonado, M. Mallaby-Kay, D. Marsden, L. Maurin, J. McMahon, F. Menanteau, K. Moodley, T. Morton, S. Naess, T. Namikawa, F. Nati, L. Newburgh, J. P. Nibarger, A. Nicola, M. D. Niemack, M. R. Nolta, J. Orłowski-Sherer, L. A. Page, C. G. Pappas, B. Partridge, P. Phakathi, H. Prince, R. Puddu, F. J. Qu, J. Rivera, N. Robertson, F. Rojas, M. Salatino, E. Schaan, A. Schillaci, B. L. Schmitt, N. Sehgal, B. D. Sherwin, C. Sierra, J. Sievers, C. Sifon, P. Sikhosana, S. Simon, D. N. Spergel, S. T. Staggs, J. Stevens, E. Storer, D. D. Sunder, E. R. Switzer, B. Thorne, R. Thornton, H. Trac, J. Treu, C. Tucker, L. R. Vale, A. V. Engelen, J. V. Lanen, E. M. Vavagiakis, K. Wagoner, Y. Wang, J. T. Ward, E. J. Wollack, Z. Xu, F. Zago, and N. Zhu. The atacama cosmology telescope: a measurement of the cosmic microwave background power spectra at 98 and 150 GHz. *JCAP*, 2020(12):

- 045–045, dec 2020. doi: 10.1088/1475-7516/2020/12/045. URL <https://doi.org/10.1088/1475-7516/2020/12/045>.
- [16] J. J. Condon and A. M. Matthews.  $\lambda$ cdm cosmology for astronomers. *PASP*, 130(989):073001, Jun 2018. ISSN 1538-3873. doi: 10.1088/1538-3873/aac1b2. URL <http://dx.doi.org/10.1088/1538-3873/aac1b2>.
- [17] G. Coppi, Z. Xu, A. Ali, N. Galitzki, P. A. Gallardo, A. J. May, J. L. Orlowski-Scherer, N. Zhu, M. J. Devlin, S. Dicker, B. Keating, M. Limon, M. Lungu, J. McMahon, M. D. Niemack, L. Piccirillo, G. Puglisi, M. Salatino, S. M. Simon, G. Teply, R. Thornton, and E. M. Vavagiakis. Cooldown strategies and transient thermal simulations for the Simons Observatory. In J. Zmuidzinas and J.-R. Gao, editors, *2018SPIE10708*, volume 10708, pages 246 – 258. International Society for Optics and Photonics, SPIE, 2018. doi: 10.1117/12.2312679. URL <https://doi.org/10.1117/12.2312679>.
- [18] K. P. Coughlin, J. J. McMahon, K. T. Crowley, B. J. Koopman, K. H. Miller, S. M. Simon, and E. J. Wollack. Pushing the limits of broadband and high-frequency metamaterial silicon antireflection coatings. *JLTP*, 193(5-6):876–885, May 2018. ISSN 1573-7357. doi: 10.1007/s10909-018-1955-7. URL <http://dx.doi.org/10.1007/s10909-018-1955-7>.
- [19] R. Datta, C. D. Munson, M. D. Niemack, J. J. McMahon, J. Britton, E. J. Wollack, J. Beall, M. J. Devlin, J. Fowler, P. Gallardo, J. Hubmayr, K. Irwin, L. Newburgh, J. P. Nibarger, L. Page, M. A. Quijada, B. L. Schmitt, S. T. Staggs, R. Thornton, and L. Zhang. Large-aperture wide-bandwidth antireflection-coated

silicon lenses for millimeter wavelengths. *Appl. Opt.*, 52:8747, Dec. 2013. doi: 10.1364/AO.52.008747.

- [20] R. Datta, S. Aiola, S. K. Choi, M. Devlin, J. Dunkley, R. Dünner, P. A. Gallardo, M. Gralla, M. Halpern, M. Hasselfield, M. Hilton, A. D. Hincks, S.-P. P. Ho, J. Hubmayr, K. M. Huffenberger, J. P. Hughes, A. Kosowsky, C. H. López-Caraballo, T. Louis, M. Lungu, T. Marriage, L. Maurin, J. McMahon, K. Moodley, S. K. Naess, F. Nati, M. D. Niemack, L. A. Page, B. Partridge, H. Prince, S. T. Staggs, E. R. Switzer, E. J. Wollack, and G. Farren. The Atacama Cosmology Telescope: two-season ACTPol extragalactic point sources and their polarization properties. *Monthly Notices of the Royal Astronomical Society*, 486(4):5239–5262, 11 2018. ISSN 0035-8711. doi: 10.1093/mnras/sty2934. URL <https://doi.org/10.1093/mnras/sty2934>.
- [21] DESI Collaboration, A. Aghamousa, J. Aguilar, S. Ahlen, S. Alam, L. E. Allen, C. A. Prieto, J. Annis, S. Bailey, C. Balland, O. Ballester, C. Baltay, L. Beaufore, C. Bebek, T. C. Beers, E. F. Bell, J. L. Bernal, R. Besuner, F. Beutler, C. Blake, H. Bleuler, M. Blomqvist, R. Blum, A. S. Bolton, C. Briceno, D. Brooks, J. R. Brownstein, E. Buckley-Geer, A. Burden, E. Burtin, N. G. Busca, R. N. Cahn, Y.-C. Cai, L. Cardiel-Sas, R. G. Carlberg, P.-H. Carton, R. Casas, F. J. Castander, J. L. Cervantes-Cota, T. M. Claybaugh, M. Close, C. T. Coker, S. Cole, J. Comparat, A. P. Cooper, M. C. Cousinou, M. Crocce, J.-G. Cuby, D. P. Cunningham, T. M. Davis, K. S. Dawson, A. de la Macorra, J. D. Vicente, T. Delubac, M. Derwent, A. Dey, G. Dhungana, Z. Ding, P. Doel, Y. T. Duan, A. Ealet, J. Edelstein, S. Eftekharzadeh, D. J. Eisenstein, A. Elliott, S. Escoffier,



M. Evatt, P. Fagrelus, X. Fan, K. Fanning, A. Farahi, J. Farihi, G. Favole, Y. Feng, E. Fernandez, J. R. Findlay, D. P. Finkbeiner, M. J. Fitzpatrick, B. Flaughner, S. Flender, A. Font-Ribera, J. E. Forero-Romero, P. Fosalba, C. S. Frenk, M. Fumagalli, B. T. Gaensicke, G. Gallo, J. Garcia-Bellido, E. Gaztanaga, N. P. G. Fusillo, T. Gerard, I. Gershkovich, T. Giannantonio, D. Gillet, G. G. de Rivera, V. Gonzalez-Perez, S. Gott, O. Graur, G. Gutierrez, J. Guy, S. Habib, H. Heetderks, I. Heetderks, K. Heitmann, W. A. Hellwing, D. A. Herrera, S. Ho, S. Holland, K. Honscheid, E. Huff, T. A. Hutchinson, D. Huterer, H. S. Hwang, J. M. I. Laguna, Y. Ishikawa, D. Jacobs, N. Jeffrey, P. Jelinsky, E. Jennings, L. Jiang, J. Jimenez, J. Johnson, R. Joyce, E. Jullo, S. Juneau, S. Kama, A. Karcher, S. Karkar, R. Kehoe, N. Kennamer, S. Kent, M. Kilbinger, A. G. Kim, D. Kirkby, T. Kisner, E. Kitanidis, J.-P. Kneib, S. Kopusov, E. Kovacs, K. Koyama, A. Kremin, R. Kron, L. Kronig, A. Kueter-Young, C. G. Lacey, R. Lafever, O. Lahav, A. Lambert, M. Lampton, M. Landriau, D. Lang, T. R. Lauer, J.-M. L. Goff, L. L. Guillou, A. L. V. Suu, J. H. Lee, S.-J. Lee, D. Leitner, M. Lesser, M. E. Levi, B. L'Huillier, B. Li, M. Liang, H. Lin, E. Linder, S. R. Loebman, Z. Lukić, J. Ma, N. MacCrann, C. Magneville, L. Makarem, M. Manera, C. J. Manser, R. Marshall, P. Martini, R. Massey, T. Matheson, J. McCauley, P. McDonald, I. D. McGreer, A. Meisner, N. Metcalfe, T. N. Miller, R. Miquel, J. Moustakas, A. Myers, M. Naik, J. A. Newman, R. C. Nichol, A. Nicola, L. N. da Costa, J. Nie, G. Niz, P. Norberg, B. Nord, D. Norman, P. Nugent, T. O'Brien, M. Oh, K. A. G. Olsen, C. Padilla, H. Padmanabhan, N. Padmanabhan, N. Palanque-Delabrouille, A. Palmese, D. Pappalardo, I. Pâris, C. Park, A. Patej, J. A. Peacock, H. V. Peiris, X. Peng, W. J. Percival, S. Perru-

chot, M. M. Pieri, R. Pogge, J. E. Pollack, C. Poppett, F. Prada, A. Prakash, R. G. Probst, D. Rabinowitz, A. Raichoor, C. H. Ree, A. Refregier, X. Regal, B. Reid, K. Reil, M. Rezaie, C. M. Rockosi, N. Roe, S. Ronayette, A. Roodman, A. J. Ross, N. P. Ross, G. Rossi, E. Rozo, V. Ruhlmann-Kleider, E. S. Rykoff, C. Sabiu, L. Samushia, E. Sanchez, J. Sanchez, D. J. Schlegel, M. Schneider, M. Schubnell, A. Secroun, U. Seljak, H.-J. Seo, S. Serrano, A. Shafieloo, H. Shan, R. Sharples, M. J. Sholl, W. V. Shourt, J. H. Silber, D. R. Silva, M. M. Sirk, A. Slosar, A. Smith, G. F. Smoot, D. Som, Y.-S. Song, D. Sprayberry, R. Staten, A. Stefanik, G. Tarle, S. S. Tie, J. L. Tinker, R. Tojeiro, F. Valdes, O. Valenzuela, M. Valluri, M. Vargas-Magana, L. Verde, A. R. Walker, J. Wang, Y. Wang, B. A. Weaver, C. Weaverdyck, R. H. Wechsler, D. H. Weinberg, M. White, Q. Yang, C. Yeche, T. Zhang, G.-B. Zhao, Y. Zheng, X. Zhou, Z. Zhou, Y. Zhu, H. Zou, and Y. Zu. The desi experiment part i: Science, targeting, and survey design, 2016.

- [22] S. R. Dicker, P. A. Gallardo, J. E. Gudmundsson, P. D. Mauskopf, A. Ali, P. C. Ashton, G. Coppi, M. J. Devlin, N. Galitzki, S. P. Ho, C. A. Hill, J. Hubmayr, B. Keating, A. T. Lee, M. Limon, F. Matsuda, J. McMahon, M. D. Niemack, J. L. Orlowski-Scherer, L. Piccirillo, M. Salatino, S. M. Simon, S. T. Staggs, R. Thornton, J. N. Ullom, E. M. Vavagiakis, E. J. Wollack, Z. Xu, and N. Zhu. Cold optical design for the large aperture Simons' Observatory telescope. In H. K. Marshall and J. Spyromilio, editors, *2018SPIE10700*, volume 10700, pages 1064 – 1076. International Society for Optics and Photonics, SPIE, 2018. doi: 10.1117/12.2313444. URL <https://doi.org/10.1117/12.2313444>.

- [23] B. Dober, Z. Ahmed, K. Arnold, D. T. Becker, D. A. Bennett, J. A. Connors, A. Cukierman, J. M. D’Ewart, S. M. Duff, J. E. Dusatko, J. C. Frisch, J. D. Gard, S. W. Henderson, R. Herbst, G. C. Hilton, J. Hubmayr, Y. Li, J. A. B. Mates, H. McCarrick, C. D. Reintsema, M. Silva-Feaver, L. Ruckman, J. N. Ullom, L. R. Vale, D. D. Van Winkle, J. Vasquez, Y. Wang, E. Young, C. Yu, and K. Zheng. A microwave SQUID multiplexer optimized for bolometric applications. *ApPhL*, 118(6):062601, Feb. 2021. doi: 10.1063/5.0033416.
- [24] S. Dodelson and F. Schmidt. *Modern Cosmology*. Elsevier Inc., 2021.
- [25] L. Duband, T. Prouve, J. Bock, L. Moncelsi, and A. Schillaci. Sub-kelvin cooling for the bicep array project. In *Proceedings of the 20th International Cryocooler Conference*, pages 347 – 356. International Cryocooler Conference, 2018.
- [26] S. M. Duff, J. Austermann, J. A. Beall, D. Becker, R. Datta, P. A. Gallardo, S. W. Henderson, G. C. Hilton, S. P. Ho, J. Hubmayr, B. J. Koopman, D. Li, J. McMahon, F. Nati, M. D. Niemack, C. G. Pappas, M. Salatino, B. L. Schmitt, S. M. Simon, S. T. Staggs, J. R. Stevens, J. Van Lanen, E. M. Vavagiakis, J. T. Ward, and E. J. Wollack. Advanced actpol multichroic polarimeter array fabrication process for 150 mm wafers. *JLTP*, 184(3):634–641, Aug 2016. ISSN 1573-7357. doi: 10.1007/s10909-016-1576-y. URL <https://doi.org/10.1007/s10909-016-1576-y>.
- [27] D. J. Fixsen. THE TEMPERATURE OF THE COSMIC MICROWAVE BACKGROUND. *The Astrophysical Journal*, 707(2):916–920, nov 2009. doi:

10.1088/0004-637x/707/2/916. URL <https://doi.org/10.1088/0004-637x/707/2/916>.

- [28] J. Froustey, C. Pitrou, and M. C. Volpe. Neutrino decoupling including flavour oscillations and primordial nucleosynthesis. *Journal of Cosmology and Astroparticle Physics*, 2020(12):015–015, dec 2020. doi: 10.1088/1475-7516/2020/12/015. URL <https://doi.org/10.1088/1475-7516/2020/12/015>.
- [29] Y. Fukuda, T. Hayakawa, E. Ichihara, K. Inoue, K. Ishihara, H. Ishino, Y. Itow, T. Kajita, J. Kameda, S. Kasuga, K. Kobayashi, Y. Kobayashi, Y. Koshio, M. Miura, M. Nakahata, S. Nakayama, A. Okada, K. Okumura, N. Sakurai, M. Shiozawa, Y. Suzuki, Y. Takeuchi, Y. Totsuka, S. Yamada, M. Earl, A. Habig, E. Kearns, M. D. Messier, K. Scholberg, J. L. Stone, L. R. Sulak, C. W. Walter, M. Goldhaber, T. Barszczak, D. Casper, W. Gajewski, P. G. Halverson, J. Hsu, W. R. Kropp, L. R. Price, F. Reines, M. Smy, H. W. Sobel, M. R. Vagins, K. S. Ganezer, W. E. Keig, R. W. Ellsworth, S. Tasaka, J. W. Flanagan, A. Kibayashi, J. G. Learned, S. Matsuno, V. J. Stenger, D. Takemori, T. Ishii, J. Kanzaki, T. Kobayashi, S. Mine, K. Nakamura, K. Nishikawa, Y. Oyama, A. Sakai, M. Sakuda, O. Sasaki, S. Echigo, M. Kohama, A. T. Suzuki, T. J. Haines, E. Blaufuss, B. K. Kim, R. Sanford, R. Svoboda, M. L. Chen, Z. Conner, J. A. Goodman, G. W. Sullivan, J. Hill, C. K. Jung, K. Martens, C. Mauger, C. McGrew, E. Sharkey, B. Viren, C. Yanagisawa, W. Doki, K. Miyano, H. Okazawa, C. Saji, M. Takahata, Y. Nagashima, M. Takita, T. Yamaguchi, M. Yoshida, S. B. Kim, M. Etoh, K. Fujita, A. Hasegawa, T. Hasegawa, S. Hatakeyama, T. Iwamoto, M. Koga, T. Maruyama, H. Ogawa, J. Shirai, A. Suzuki, F. Tsushima, M. Koshihara,

M. Nemoto, K. Nishijima, T. Futagami, Y. Hayato, Y. Kanaya, K. Kaneyuki, Y. Watanabe, D. Kielczewska, R. A. Doyle, J. S. George, A. L. Stachyra, L. L. Wai, R. J. Wilkes, and K. K. Young. Evidence for oscillation of atmospheric neutrinos. *Phys. Rev. Lett.*, 81:1562–1567, Aug 1998. doi: 10.1103/PhysRevLett.81.1562. URL <https://link.aps.org/doi/10.1103/PhysRevLett.81.1562>.

- [30] N. Galitzki, A. Ali, K. S. Arnold, P. C. Ashton, J. E. Ausermann, C. Baccigalupi, T. Baildon, D. Barron, J. A. Beall, S. Beckman, S. M. M. Bruno, S. Bryan, P. G. Calisse, G. E. Chesmore, Y. Chinone, S. K. Choi, G. Coppi, K. D. Crowley, K. T. Crowley, A. Cukierman, M. J. Devlin, S. Dicker, B. Dober, S. M. Duff, J. Dunkley, G. Fabbian, P. A. Gallardo, M. Gerbino, N. Goeckner-Wald, J. E. Golec, J. E. Gudmundsson, E. E. Healy, S. Henderson, C. A. Hill, G. C. Hilton, S.-P. P. Ho, L. A. Howe, J. Hubmayr, O. Jeong, B. Keating, B. J. Koopman, K. Kiuchi, A. Kusaka, J. Lashner, A. T. Lee, Y. Li, M. Limon, M. Lungu, F. Matsuda, P. D. Mauskopf, A. J. May, N. McCallum, J. McMahon, F. Nati, M. D. Niemack, J. L. Orłowski-Scherer, S. C. Parshley, L. Piccirillo, M. S. Rao, C. Raum, M. Salatino, J. S. Seibert, C. Sierra, M. Silva-Feaver, S. M. Simon, S. T. Staggs, J. R. Stevens, A. Suzuki, G. Teply, R. Thornton, C. Tsai, J. N. Ullom, E. M. Vavagiakis, M. R. Vissers, B. Westbrook, E. J. Wollack, Z. Xu, and N. Zhu. The Simons Observatory: instrument overview. In J. Zmuidzinas and J.-R. Gao, editors, *2018SPIE10708*, volume 10708, pages 1 – 13. International Society for Optics and Photonics, SPIE, 2018. doi: 10.1117/12.2312985. URL <https://doi.org/10.1117/12.2312985>.

- [31] P. A. Gallardo, J. Gudmundsson, B. J. Koopman, F. T. Matsuda, S. M. Simon,

- A. Ali, S. Bryan, Y. Chinone, G. Coppi, N. Cothard, M. J. Devlin, S. Dicker, G. Fabbian, N. Galitzki, C. A. Hill, B. Keating, A. Kusaka, J. Lashner, A. T. Lee, M. Limon, P. D. Mauskopf, J. McMahon, F. Nati, M. D. Niemack, J. L. Orłowski-Scherer, S. C. Parshley, G. Puglisi, C. L. Reichardt, M. Salatino, S. Staggs, A. Suzuki, E. M. Vavagiakis, E. J. Wollack, Z. Xu, and N. Zhu. Systematic uncertainties in the Simons Observatory: optical effects and sensitivity considerations. In J. Zmuidzinas and J.-R. Gao, editors, *2018SPIE10708*, volume 10708, pages 658 – 673. International Society for Optics and Photonics, SPIE, 2018. doi: 10.1117/12.2312971. URL <https://doi.org/10.1117/12.2312971>.
- [32] J. E. Golec, J. J. McMahon, A. Ali, S. Dicker, N. Galitzki, K. Harrington, B. Westbrook, E. J. Wollack, Z. Xu, and N. Zhu. Design and fabrication of metamaterial anti-reflection coatings for the Simons Observatory. In R. Navarro and R. Geys, editors, *2021SPIE11451*, volume 11451, pages 1182 – 1189. International Society for Optics and Photonics, SPIE, 2020. doi: 10.1117/12.2561720. URL <https://doi.org/10.1117/12.2561720>.
- [33] R. Gualtieri, J. P. Filippini, P. A. R. Ade, M. Amiri, S. J. Benton, A. S. Bergman, R. Bihary, J. J. Bock, J. R. Bond, S. A. Bryan, H. C. Chiang, C. R. Contaldi, O. Doré, A. J. Duivenvoorden, H. K. Eriksen, M. Farhang, L. M. Fissel, A. A. Fraisse, K. Freese, M. Galloway, A. E. Gambrel, N. N. Gandilo, K. Ganga, R. V. Gramillano, J. E. Gudmundsson, M. Halpern, J. Hartley, M. Hasselfield, G. Hilton, W. Holmes, V. V. Hristov, Z. Huang, K. D. Irwin, W. C. Jones, C. L. Kuo, Z. D. Kermish, S. Li, P. V. Mason, K. Megerian, L. Moncelsi, T. A. Morford, J. M. Nagy, C. B. Netterfield, M. Nolta, B. Osherson, I. L. Padilla, B. Racine,

- A. S. Rahlin, C. Reintsema, J. E. Ruhl, M. C. Runyan, T. M. Ruud, J. A. Shariff, J. D. Soler, X. Song, A. Trangsrud, C. Tucker, R. S. Tucker, A. D. Turner, J. F. v. d. List, A. C. Weber, I. K. Wehus, D. V. Wiebe, and E. Y. Young. SPIDER: CMB Polarimetry from the Edge of Space. *JLTP*, 193:1112–1121, Dec. 2018. doi: 10.1007/s10909-018-2078-x.
- [34] J. Gudmundsson, P. Ade, M. Amiri, S. Benton, J. Bock, J. Bond, S. Bryan, H. Chiang, C. Contaldi, B. Crill, O. Dore, J. Filippini, A. Fraisse, A. Gambrel, N. Gandilo, M. Hasselfield, M. Halpern, G. Hilton, W. Holmes, V. Hristov, K. Irwin, W. Jones, Z. Kermish, C. MacTavish, P. Mason, K. Megerian, L. Moncelsi, T. Montroy, T. Morford, J. Nagy, C. Netterfield, A. Rahlin, C. Reintsema, J. Ruhl, M. Runyan, J. Shariff, J. Soler, A. Trangsrud, C. Tucker, R. Tucker, A. Turner, D. Wiebe, and E. Young. The thermal design, characterization, and performance of the spider long-duration balloon cryostat. *Cryo*, 72:65 – 76, 2015. ISSN 0011-2275. doi: <https://doi.org/10.1016/j.cryogenics.2015.09.002>. URL <http://www.sciencedirect.com/science/article/pii/S0011227515001095>.
- [35] J. E. Gudmundsson, P. A. Gallardo, R. Puddu, S. R. Dicker, A. E. Adler, A. M. Ali, A. Bazarko, G. E. Chesmore, G. Coppi, N. F. Cothard, and et al. The simons observatory: modeling optical systematics in the large aperture telescope. *ApOpt*, 60(4):823, Jan 2021. ISSN 2155-3165. doi: 10.1364/ao.411533. URL <http://dx.doi.org/10.1364/AO.411533>.
- [36] S. Guns, A. Foster, C. Daley, A. Rahlin, N. Whitehorn, P. A. R. Ade, Z. Ahmed, E. Anderes, A. J. Anderson, M. Archibley, and et al. Detection of galactic and

extragalactic millimeter-wavelength transient sources with spt-3g, Aug 2021. ISSN 1538-4357. URL <http://dx.doi.org/10.3847/1538-4357/ac06a3>.

- [37] A. H. Guth. Inflationary universe: A possible solution to the horizon and flatness problems. *Phys. Rev. D*, 23:347–356, Jan 1981. doi: 10.1103/PhysRevD.23.347. URL <https://link.aps.org/doi/10.1103/PhysRevD.23.347>.
- [38] K. Harrington, T. Marriage, A. Ali, J. W. Appel, C. L. Bennett, F. Boone, M. Brewer, M. Chan, D. T. Chuss, F. Colazo, S. Dahal, K. Denis, R. Dünner, J. Eimer, T. Essinger-Hileman, P. Fluxa, M. Halpern, G. Hilton, G. F. Hinshaw, J. Hubmayr, J. Iuliano, J. Karakla, J. McMahon, N. T. Miller, S. H. Moseley, G. Palma, L. Parker, M. Petroff, B. Pradenas, K. Rostem, M. Sagliocca, D. Valle, D. Watts, E. Wollack, Z. Xu, and L. Zeng. The Cosmology Large Angular Scale Surveyor. In W. S. Holland and J. Zmuidzinas, editors, *2016SPIE 9914*, volume 9914, pages 380 – 400. International Society for Optics and Photonics, SPIE, 2016. doi: 10.1117/12.2233125. URL <https://doi.org/10.1117/12.2233125>.
- [39] K. Harrington, C. Sierra, G. Chesmore, S. Sutariya, A. M. Ali, S. K. Choi, N. F. Cothard, S. Dicker, N. Galitzki, S.-P. P. Ho, A. M. Kofman, B. J. Koopman, J. Lashner, J. McMahon, M. D. Niemack, J. Orłowski-Scherer, J. Seibert, M. Silva-Feaver, E. M. Vavagiakis, Z. Xu, and N. Zhu. The integration and testing program for the Simons Observatory Large Aperture Telescope optics tubes. In J. Zmuidzinas and J.-R. Gao, editors, *Millimeter, Submillimeter, and Far-Infrared Detectors and Instrumentation for Astronomy X*, volume 11453, pages 236 – 245. International Society for Optics and Photonics, SPIE, 2020. doi: 10.1117/12.2562647. URL <https://doi.org/10.1117/12.2562647>.



- [40] S. W. Henderson, R. Allison, J. Austermann, T. Baildon, N. Battaglia, J. A. Beall, D. Becker, F. De Bernardis, J. R. Bond, E. Calabrese, and et al. Advanced actpol cryogenic detector arrays and readout. *JLTP*, 184(3-4):772–779, Mar 2016. ISSN 1573-7357. doi: 10.1007/s10909-016-1575-z. URL <http://dx.doi.org/10.1007/s10909-016-1575-z>.
- [41] S. W. Henderson, Z. Ahmed, D. Brown, S. Chaudhuri, H.-M. S. Cho, J. M. D’Ewart, B. Dober, J. E. Dusatko, S. Fatigoni, J. C. Frisch, and et al. Highly-multiplexed microwave squid readout using the slac microresonator radio frequency (smurf) electronics for future cmb and sub-millimeter surveys. *Millimeter, Submillimeter, and Far-Infrared Detectors and Instrumentation for Astronomy IX*, Jul 2018. doi: 10.1117/12.2314435. URL <http://dx.doi.org/10.1117/12.2314435>.
- [42] M. Hilton, M. Hasselfield, C. Sifón, N. Battaglia, S. Aiola, V. Bharadwaj, J. R. Bond, S. K. Choi, D. Crichton, R. Datta, and et al. The atacama cosmology telescope: The two-season actpol sunyaev–zel’dovich effect selected cluster catalog. *ApJS*, 235(1):20, Mar 2018. ISSN 1538-4365. doi: 10.3847/1538-4365/aaa6cb. URL <http://dx.doi.org/10.3847/1538-4365/aaa6cb>.
- [43] G. Hinshaw, D. Larson, E. Komatsu, D. N. Spergel, C. L. Bennett, J. Dunkley, M. R. Nolta, M. Halpern, R. S. Hill, N. Odegard, L. Page, K. M. Smith, J. L. Weiland, B. Gold, N. Jarosik, A. Kogut, M. Limon, S. S. Meyer, G. S. Tucker, E. Wollack, and E. L. Wright. NINE-YEAR WILKINSON MICROWAVE ANISOTROPY PROBE ( WMAP ) OBSERVATIONS: COSMOLOGICAL PA-

RAMETER RESULTS. *ApJS*, 208(2):19, sep 2013. doi: 10.1088/0067-0049/208/2/19. URL <https://doi.org/10.1088/0067-0049/208/2/19>.

- [44] W. Hu and N. Sugiyama. Toward understanding cmb anisotropies and their implications. *Phys. Rev. D*, 51:2599–2630, Mar 1995. doi: 10.1103/PhysRevD.51.2599. URL <https://link.aps.org/doi/10.1103/PhysRevD.51.2599>.
- [45] W. Hu and M. White. A cmb polarization primer. *NewA*, 2(4):323–344, Oct 1997. ISSN 1384-1076. doi: 10.1016/s1384-1076(97)00022-5. URL [http://dx.doi.org/10.1016/S1384-1076\(97\)00022-5](http://dx.doi.org/10.1016/S1384-1076(97)00022-5).
- [46] P. A. R. Keck Array and BICEP2 Collaborations, Ade, Z. Ahmed, R. W. Aikin, K. D. Alexander, D. Barkats, S. J. Benton, C. A. Bischoff, J. J. Bock, R. Bowens-Rubin, J. A. Brevik, I. Buder, E. Bullock, V. Buza, J. Connors, J. Cornelison, B. P. Crill, M. Crumrine, M. Dierickx, L. Duband, C. Dvorkin, J. P. Filippini, S. Fliescher, J. Grayson, G. Hall, M. Halpern, S. Harrison, S. R. Hildebrandt, G. C. Hilton, H. Hui, K. D. Irwin, J. Kang, K. S. Karkare, E. Karpel, J. P. Kaufman, B. G. Keating, S. Kefeli, S. A. Kernasovskiy, J. M. Kovac, C. L. Kuo, N. A. Larsen, K. Lau, E. M. Leitch, M. Lueker, K. G. Megerian, L. Moncelsi, T. Namikawa, C. B. Netterfield, H. T. Nguyen, R. O’Brien, R. W. Ogburn, S. Palladino, C. Pryke, B. Racine, S. Richter, A. Schillaci, R. Schwarz, C. D. Sheehy, A. Soliman, T. St. Germaine, Z. K. Staniszewski, B. Steinbach, R. V. Sudiwala, G. P. Teply, K. L. Thompson, J. E. Tolan, C. Tucker, A. D. Turner, C. Umiltà, A. G. Viereg, A. Wandui, A. C. Weber, D. V. Wiebe, J. Willmert, C. L. Wong, W. L. K. Wu, H. Yang, K. W. Yoon, and C. Zhang. Constraints on primordial gravitational waves using *planck*, *wmap*, and new *bicep2/keck* observations through the 2015

season. *PhRvL*, 121:221301, Nov 2018. doi: 10.1103/PhysRevLett.121.221301.  
URL <https://link.aps.org/doi/10.1103/PhysRevLett.121.221301>.

- [47] C. W. Keller, G. R. Cunnington, and A. P. Glassford. Thermal performance of multilayer insulations final report. Technical Report vol 22, Lockheed Missiles & Space Company, 04 1974.
- [48] B. J. Koopman, J. Lashner, L. J. Saunders, M. Hasselfield, T. Bhandarkar, S. Bhimani, S. K. Choi, C. J. Duell, N. Galitzki, K. Harrington, A. D. Hincks, S.-P. P. Ho, L. Newburgh, C. L. Reichardt, J. Seibert, J. Spisak, B. Westbrook, Z. Xu, and N. Zhu. The Simons Observatory: overview of data acquisition, control, monitoring, and computer infrastructure. In J. C. Guzman and J. Ibsen, editors, *2021SPIE11452*, volume 11452, pages 35 – 53. International Society for Optics and Photonics, SPIE, 2020. doi: 10.1117/12.2561771. URL <https://doi.org/10.1117/12.2561771>.
- [49] A. Kusaka, J. Appel, T. Essinger-Hileman, J. A. Beall, L. E. Campusano, H.-M. Cho, S. K. Choi, K. Crowley, J. W. Fowler, P. Gallardo, M. Hasselfield, G. Hilton, S.-P. P. Ho, K. Irwin, N. Jarosik, M. D. Niemack, G. W. Nixon, M. ~Nolta, L. A. P. Jr., G. A. Palma, L. Parker, S. Raghunathan, C. D. Reintsema, J. Sievers, S. M. Simon, S. T. Staggs, K. Visnjic, and K.-W. Yoon. Results from the atacama b-mode search (ABS) experiment. *JCAP*, 2018(09):005–005, sep 2018. doi: 10.1088/1475-7516/2018/09/005. URL <https://doi.org/10.1088/2F1475-7516%2F2018%2F09%2F005>.
- [50] Y. Li, K. Arnold, Z. Atkins, S. M. Bruno, N. F. Cothard, B. Dober, C. J. Duell,

- S. M. Duff, P. A. Gallardo, E. Healy, S.-P. P. Ho, J. Hubmayr, B. Keating, A. T. Lee, A. Mangu, H. McCarrick, M. D. Niemack, L. Newburgh, C. Raum, M. Salatino, T. Sasse, M. Silva-Feaver, S. M. Simon, S. Staggs, A. Suzuki, J. Ullom, E. M. Vavagiakis, M. R. Vissers, Y. Wang, B. Westbrook, E. J. Wollack, Z. Xu, K. Zheng, and N. Zhu. Assembly and integration process of the high-density detector array readout modules for the simons observatory. *JLTP*, 199(3):985–993, 2020. ISSN 1573-7357. doi: 10.1007/s10909-020-02386-6. URL <https://doi.org/10.1007/s10909-020-02386-6>.
- [51] A. Liddle. *Introduction to Modern Cosmology*. John Wiley & Sons Ltd, 2002.
- [52] J. L. Lizon and M. Accardo. LN2 continuous flow cryostats: a compact vibration free cooling system for single to multiple detector systems. In E. Atad-Ettedgui and D. Lemke, editors, *2010SPIE 7739*, volume 7739, pages 1226 – 1232. International Society for Optics and Photonics, SPIE, 2010. doi: 10.1117/12.856013. URL <https://doi.org/10.1117/12.856013>.
- [53] E. Marquardt, J. Le, and R. Radebaugh. Cryogenic material properties database. In *Cryocoolers 11*, pages 681–687. Springer, 2002.
- [54] J. A. B. Mates, K. D. Irwin, L. R. Vale, G. C. Hilton, J. Gao, and K. W. Lehnert. Flux-ramp modulation for squid multiplexing. *JLTP*, 167(5):707–712, Jun 2012. ISSN 1573-7357. doi: 10.1007/s10909-012-0518-6. URL <https://doi.org/10.1007/s10909-012-0518-6>.
- [55] J. C. Mather. Bolometers: ultimate sensitivity, optimization, and amplifier

coupling. *ApOpt*, 23(4):584–588, Feb 1984. doi: 10.1364/AO.23.000584. URL <http://ao.osa.org/abstract.cfm?URI=ao-23-4-584>.

- [56] H. McCarrick, E. Healy, Z. Ahmed, K. Arnold, Z. Atkins, J. E. Austermann, T. Bhandarkar, J. A. Beall, S. M. Bruno, S. K. Choi, J. Connors, N. F. Cothard, K. D. Crowley, S. Dicker, B. Dober, C. J. Duell, S. M. Duff, D. Dutcher, J. C. Frisch, N. Galitzki, M. B. Gralla, J. E. Gudmundsson, S. W. Henderson, G. C. Hilton, S.-P. P. Ho, Z. B. Huber, J. Hubmayr, J. Iuliano, B. R. Johnson, A. M. Kofman, A. Kusaka, J. Lashner, A. T. Lee, Y. Li, M. J. Link, T. J. Lucas, M. Lungu, J. A. B. Mates, J. J. McMahon, M. D. Niemack, J. Orłowski-Scherer, J. Seibert, M. Silva-Feaver, S. M. Simon, S. Staggs, A. Suzuki, T. Terasaki, J. N. Ullom, E. M. Vavagiakis, L. R. Vale, J. V. Lanen, M. R. Vissers, Y. Wang, E. J. Wollack, Z. Xu, E. Young, C. Yu, K. Zheng, N. Zhu, and R. Thornton. The simons observatory microwave SQUID multiplexing detector module design. *The Astrophysical Journal*, 922(1):38, nov 2021. doi: 10.3847/1538-4357/ac2232. URL <https://doi.org/10.3847/1538-4357/ac2232>.
- [57] V. Mukhanov. *Physical Foundations of Cosmology*. Cambridge University Press, 2005.
- [58] A. Nadolski, A. M. Kofman, J. D. Vieira, P. A. R. Ade, Z. Ahmed, A. J. Anderson, J. S. Avva, R. B. Thakur, A. N. Bender, B. A. Benson, J. E. Carlstrom, F. W. Carter, T. W. Cecil, C. L. Chang, J. F. Cliche, A. Cukierman, T. de Haan, J. Ding, M. A. Dobbs, D. Dutcher, W. Everett, A. Foster, J. Fu, J. Gallichio, A. Gilbert, J. C. Groh, S. T. Guns, R. Guyser, N. W. Halverson, A. H. Harke-Hosemann, N. L. Harrington, J. W. Henning, W. L. Holzapfel, N. Huang, K. D. Irwin, O. B.

- Jeong, M. Jonas, A. Jones, T. S. Khaire, M. Korman, D. L. Kubik, S. Kuhlmann, C.-L. Kuo, A. T. Lee, A. E. Lowitz, S. S. Meyer, D. Michalik, J. Montgomery, T. Natoli, H. Nguyen, G. I. Noble, V. Novosad, S. Padin, Z. Pan, J. Pearson, C. M. Posada, W. Quan, A. Rahlin, J. E. Ruhl, J. T. Sayre, E. Shirokoff, G. Smecher, J. A. Sobrin, A. A. Stark, K. T. Story, A. Suzuki, K. L. Thompson, C. Tucker, K. Vanderlinde, G. Wang, N. Whitehorn, V. Yefremenko, K. W. Yoon, and M. R. Young. Broadband anti-reflective coatings for cosmic microwave background experiments. In J. Zmuidzinas and J.-R. Gao, editors, *2018SPIE10708*, volume 10708, pages 719 – 731. International Society for Optics and Photonics, SPIE, 2018. doi: 10.1117/12.2315674. URL <https://doi.org/10.1117/12.2315674>.
- [59] S. Naess, N. Battaglia, J. Richard Bond, E. Calabrese, S. K. Choi, N. F. Cothard, M. Devlin, C. J. Duell, A. J. Duivenvoorden, J. Dunkley, and et al. The atacama cosmology telescope: Detection of millimeter-wave transient sources. *The Astrophysical Journal*, 915(1):14, Jun 2021. ISSN 1538-4357. doi: 10.3847/1538-4357/abfe6d. URL <http://dx.doi.org/10.3847/1538-4357/abfe6d>.
- [60] M. D. Niemack, P. A. R. Ade, J. Aguirre, F. Barrientos, J. A. Beall, J. R. Bond, J. Britton, H. M. Cho, S. Das, M. J. Devlin, and et al. Actpol: a polarization-sensitive receiver for the atacama cosmology telescope. *2010SPIE 7741*, Jul 2010. doi: 10.1117/12.857464. URL <http://dx.doi.org/10.1117/12.857464>.
- [61] NIST. Properties of solid materials from cryogenic- to room-temperatures. <https://trc.nist.gov/cryogenics/materials/materialproperties.htm>, 2009.
- [62] J. Orlowski-Scherer, E. Baxter, M. Devlin, B. Jain, and C. Blake. Characterizing

Extra-solar Oort Clouds with Submillimeter-wave Observations. *BAAS*, 51(3): 349, May 2019.

- [63] J. L. Orlowski-Scherer, N. Zhu, Z. Xu, A. Ali, K. S. Arnold, P. C. Ashton, G. Coppi, M. Devlin, S. Dicker, N. Galitzki, P. A. Gallardo, B. Keating, A. T. Lee, M. Limon, M. Lungu, A. May, J. McMahon, M. D. Niemack, L. Piccirillo, G. Puglisi, M. Salatino, M. Silva-Feaver, S. M. Simon, R. Thornton, and E. M. Vavagiakis. Simons Observatory large aperture receiver simulation overview. In J. Zmuidzinas and J.-R. Gao, editors, *2018SPIE10708*, volume 10708, pages 644 – 657. International Society for Optics and Photonics, SPIE, 2018. doi: 10.1117/12.2312868. URL <https://doi.org/10.1117/12.2312868>.
- [64] Z. Pan, P. A. R. Ade, Z. Ahmed, A. J. Anderson, J. E. Austermann, J. S. Avva, R. B. Thakur, A. N. Bender, B. A. Benson, J. E. Carlstrom, F. W. Carter, T. Cecil, C. L. Chang, J. F. Cliche, A. Cukierman, E. V. Denison, T. de Haan, J. Ding, M. A. Dobbs, D. Dutcher, W. Everett, A. Foster, R. N. Gannon, A. Gilbert, J. C. Groh, N. W. Halverson, A. H. Harke-Hosemann, N. L. Harrington, J. W. Henning, G. C. Hilton, W. L. Holzapfel, N. Huang, K. D. Irwin, O. B. Jeong, M. Jonas, T. Khaire, A. M. Kofman, M. Korman, D. Kubik, S. Kuhlmann, C. L. Kuo, A. T. Lee, A. E. Lowitz, S. S. Meyer, D. Michalik, J. Montgomery, A. Nadolski, T. Natoli, H. Nguyen, G. I. Noble, V. Novosad, S. Padin, J. Pearson, C. M. Posada, A. Rahlin, J. E. Ruhl, L. J. Saunders, J. T. Sayre, I. Shirley, E. Shirokoff, G. Smecher, J. A. Sobrin, A. A. Stark, K. T. Story, A. Suzuki, Q. Y. Tang, K. L. Thompson, C. Tucker, L. R. Vale, K. Vanderlinde, J. D. Vieira, G. Wang, N. Whitehorn, V. Yefremenko, K. W. Yoon, and M. R. Young. Optical

Characterization of the SPT-3G Camera. *JLTP*, 193(3-4):305–313, Nov. 2018.  
doi: 10.1007/s10909-018-1935-y.

- [65] S. C. Parshley, M. Niemack, R. Hills, S. R. Dicker, R. Dünner, J. Erler, P. A. Gallardo, J. E. Gudmundsson, T. Herter, B. J. Koopman, M. Limon, F. T. Matsuda, P. Mauskopf, D. A. Riechers, G. J. Stacey, and E. M. Vavagiakis. The optical design of the six-meter CCAT-prime and Simons Observatory telescopes. In H. K. Marshall and J. Spyromilio, editors, *2018SPIE10700*, volume 10700, pages 1292 – 1304. International Society for Optics and Photonics, SPIE, 2018. doi: 10.1117/12.2314073. URL <https://doi.org/10.1117/12.2314073>.
- [66] C. Pitrou, A. Coc, J.-P. Uzan, and E. Vangioni. Precision big bang nucleosynthesis with improved helium-4 predictions. *Physics Reports*, 754:1–66, 2018. ISSN 0370-1573. doi: <https://doi.org/10.1016/j.physrep.2018.04.005>. URL <https://www.sciencedirect.com/science/article/pii/S0370157318301054>. Precision big bang nucleosynthesis with improved Helium-4 predictions.
- [67] Planck Collaboration, Aghanim, N., Akrami, Y., Ashdown, M., Aumont, J., Baccigalupi, C., Ballardini, M., Banday, A. J., Barreiro, R. B., Bartolo, N., Basak, S., Battye, R., Benabed, K., Bernard, J.-P., Bersanelli, M., Bielewicz, P., Bock, J. J., Bond, J. R., Borrill, J., Bouchet, F. R., Boulanger, F., Bucher, M., Burigana, C., Butler, R. C., Calabrese, E., Cardoso, J.-F., Carron, J., Challinor, A., Chiang, H. C., Chluba, J., Colombo, L. P. L., Combet, C., Contreras, D., Crill, B. P., Cuttaia, F., de Bernardis, P., de Zotti, G., Delabrouille, J., Delouis, J.-M., Di Valentino, E., Diego, J. M., Doré, O., Douspis, M., Ducout, A., Dupac, X., Dusini, S., Efstathiou, G., Elsner, F., Enßlin, T. A., Eriksen, H. K., Fantaye,



Y., Farhang, M., Fergusson, J., Fernandez-Cobos, R., Finelli, F., Forastieri, F., Frailis, M., Fraisse, A. A., Franceschi, E., Frolov, A., Galeotta, S., Galli, S., Ganga, K., Génova-Santos, R. T., Gerbino, M., Ghosh, T., González-Nuevo, J., Górski, K. M., Gratton, S., Gruppuso, A., Gudmundsson, J. E., Hamann, J., Handley, W., Hansen, F. K., Herranz, D., Hildebrandt, S. R., Hivon, E., Huang, Z., Jaffe, A. H., Jones, W. C., Karakci, A., Keihänen, E., Keskitalo, R., Kiiveri, K., Kim, J., Kisner, T. S., Knox, L., Krachmalnicoff, N., Kunz, M., Kurki-Suonio, H., Lagache, G., Lamarre, J.-M., Lasenby, A., Lattanzi, M., Lawrence, C. R., Le Jeune, M., Lemos, P., Lesgourgues, J., Levrier, F., Lewis, A., Liguori, M., Lilje, P. B., Lilley, M., Lindholm, V., López-Caniego, M., Lubin, P. M., Ma, Y.-Z., Macías-Pérez, J. F., Maggio, G., Maino, D., Mandolesi, N., Mangilli, A., Marcos-Caballero, A., Maris, M., Martin, P. G., Martinelli, M., Martínez-González, E., Matarrese, S., Mauri, N., McEwen, J. D., Meinhold, P. R., Melchiorri, A., Mennella, A., Migliaccio, M., Millea, M., Mitra, S., Miville-Deschênes, M.-A., Molinari, D., Montier, L., Morgante, G., Moss, A., Natoli, P., Nørgaard-Nielsen, H. U., Pagano, L., Paoletti, D., Partridge, B., Patanchon, G., Peiris, H. V., Perrotta, F., Pettorino, V., Piacentini, F., Polastri, L., Polenta, G., Puget, J.-L., Rachen, J. P., Reinecke, M., Remazeilles, M., Renzi, A., Rocha, G., Rosset, C., Roudier, G., Rubiño-Martín, J. A., Ruiz-Granados, B., Salvati, L., Sandri, M., Savelainen, M., Scott, D., Shellard, E. P. S., Sirignano, C., Sirri, G., Spencer, L. D., Sunyaev, R., Suur-Uski, A.-S., Tauber, J. A., Tavagnacco, D., Tenti, M., Toffolatti, L., Tomasi, M., Trombetti, T., Valenziano, L., Valiviita, J., Van Tent, B., Vibert, L., Vielva, P., Villa, F., Vittorio, N., Wandelt, B. D., Wehus, I. K., White, M., White, S. D. M., Zacchei, A., and Zonca, A. Planck 2018 results - vi.

cosmological parameters. *A&A*, 641:A6, 2020. doi: 10.1051/0004-6361/201833910.  
URL <https://doi.org/10.1051/0004-6361/201833910>.

- [68] Planck Collaboration, Aghanim, N., Akrami, Y., Ashdown, M., Aumont, J., Baccigalupi, C., Ballardini, M., Banday, A. J., Barreiro, R. B., Bartolo, N., Basak, S., Benabed, K., Bernard, J.-P., Bersanelli, M., Bielewicz, P., Bock, J. J., Bond, J. R., Borrill, J., Bouchet, F. R., Boulanger, F., Bucher, M., Burigana, C., Butler, R. C., Calabrese, E., Cardoso, J.-F., Carron, J., Casaponsa, B., Challinor, A., Chiang, H. C., Colombo, L. P. L., Combet, C., Crill, B. P., Cuttaia, F., de Bernardis, P., de Rosa, A., de Zotti, G., Delabrouille, J., Delouis, J.-M., Di Valentino, E., Diego, J. M., Doré, O., Douspis, M., Ducout, A., Dupac, X., Dusini, S., Efstathiou, G., Elsner, F., Enßlin, T. A., Eriksen, H. K., Fantaye, Y., Fernandez-Cobos, R., Finelli, F., Frailis, M., Fraisse, A. A., Franceschi, E., Frolov, A., Galeotta, S., Galli, S., Ganga, K., Génova-Santos, R. T., Gerbino, M., Ghosh, T., Giraud-Héraud, Y., González-Nuevo, J., Górski, K. M., Gratton, S., Gruppuso, A., Gudmundsson, J. E., Hamann, J., Handley, W., Hansen, F. K., Herranz, D., Hivon, E., Huang, Z., Jaffe, A. H., Jones, W. C., Keihänen, E., Keskitalo, R., Kiiveri, K., Kim, J., Kisner, T. S., Krachmalnicoff, N., Kunz, M., Kurki-Suonio, H., Lagache, G., Lamarre, J.-M., Lasenby, A., Lattanzi, M., Lawrence, C. R., Le Jeune, M., Levrier, F., Lewis, A., Liguori, M., Lilje, P. B., Lilley, M., Lindholm, V., López-Caniego, M., Lubin, P. M., Ma, Y.-Z., Macías-Pérez, J. F., Maggio, G., Maino, D., Mandolesi, N., Mangilli, A., Marcos-Caballero, A., Maris, M., Martin, P. G., Martínez-González, E., Matarrese, S., Mauri, N., McEwen, J. D., Meinhold, P. R., Melchiorri, A., Mennella, A., Migliaccio, M., Millea, M.,

Miville-Deschênes, M.-A., Molinari, D., Moneti, A., Montier, L., Morgante, G., Moss, A., Natoli, P., Nørgaard-Nielsen, H. U., Pagano, L., Paoletti, D., Partridge, B., Patanchon, G., Peiris, H. V., Perrotta, F., Pettorino, V., Piacentini, F., Polenta, G., Puget, J.-L., Rachen, J. P., Reinecke, M., Remazeilles, M., Renzi, A., Rocha, G., Rosset, C., Roudier, G., Rubiño-Martín, J. A., Ruiz-Granados, B., Salvati, L., Sandri, M., Savelainen, M., Scott, D., Shellard, E. P. S., Sirignano, C., Sirri, G., Spencer, L. D., Sunyaev, R., Suur-Uski, A.-S., Tauber, J. A., Tavagnacco, D., Tenti, M., Toffolatti, L., Tomasi, M., Trombetti, T., Valiviita, J., Van Tent, B., Vielva, P., Villa, F., Vittorio, N., Wandelt, B. D., Wehus, I. K., Zacchei, A., and Zonca, A. Planck 2018 results - v. cmb power spectra and likelihoods. *A&A*, 641:A5, 2020. doi: 10.1051/0004-6361/201936386. URL <https://doi.org/10.1051/0004-6361/201936386>.

- [69] Polarbear Collaboration, S. Adachi, M. A. O. Aguilar Faúndez, K. Arnold, C. Bacigalupi, D. Barron, D. Beck, S. Beckman, F. Bianchini, D. Boettger, J. Borrill, J. Carron, S. Chapman, K. Cheung, Y. Chinone, K. Crowley, A. Cukierman, M. Dobbs, H. El Bouhargani, T. Elleflot, J. Errard, G. Fabbian, C. Feng, T. Fujino, N. Galitzki, N. Goeckner-Wald, J. Groh, G. Hall, N. Halverson, T. Hamada, M. Hasegawa, M. Hazumi, C. A. Hill, L. Howe, Y. Inoue, G. Jaehnig, O. Jeong, D. Kaneko, N. Katayama, B. Keating, R. Keskitalo, S. Kikuchi, T. Kisner, N. Krachmalnicoff, A. Kusaka, A. T. Lee, D. Leon, E. Linder, L. N. Lowry, A. Mangu, F. Matsuda, Y. Minami, M. Navaroli, H. Nishino, A. T. P. Pham, D. Poletti, G. Puglisi, C. L. Reichardt, Y. Segawa, M. Silva-Feaver, P. Siritanasak, N. Stebor, R. Stompor, A. Suzuki, O. Tajima, S. Takakura, S. Takatori,

- D. Tanabe, G. P. Teply, C. Tsai, C. Verges, B. Westbrook, and Y. Zhou. A Measurement of the Degree-scale CMB B-mode Angular Power Spectrum with POLARBEAR. *ApJ*, 897(1):55, July 2020. doi: 10.3847/1538-4357/ab8f24.
- [70] C. M. Posada, P. A. R. Ade, Z. Ahmed, K. Arnold, J. E. Austermann, A. N. Bender, L. E. Bleem, B. A. Benson, K. Byrum, J. E. Carlstrom, C. L. Chang, H. M. Cho, S. T. Ciocys, J. F. Cliche, T. M. Crawford, A. Cukierman, D. Czaplewski, J. Ding, R. Divan, T. de Haan, M. A. Dobbs, D. Dutcher, W. Everett, A. Gilbert, N. W. Halverson, N. L. Harrington, K. Hattori, J. W. Henning, G. C. Hilton, W. L. Holzapfel, J. Hubmayr, K. D. Irwin, O. Jeong, R. Keisler, D. Kubik, C. L. Kuo, A. T. Lee, E. M. Leitch, S. Lendinez, S. S. Meyer, C. S. Miller, J. Montgomery, M. Myers, A. Nadolski, T. Natoli, H. Nguyen, V. Novosad, S. Padin, Z. Pan, J. Pearson, J. E. Ruhl, B. R. Saliwanchik, G. Smecher, J. T. Sayre, E. Shirokoff, L. Stan, A. A. Stark, J. Sobrin, K. Story, A. Suzuki, K. L. Thompson, C. Tucker, K. Vanderlinde, J. D. Vieira, G. Wang, N. Whitehorn, V. Yefremenko, K. W. Yoon, and K. E. Ziegler. Fabrication of large dual-polarized multichroic TES bolometer arrays for CMB measurements with the SPT-3g camera. *SuScT*, 28(9):094002, aug 2015. doi: 10.1088/0953-2048/28/9/094002. URL <https://doi.org/10.1088/0953-2048/28/9/094002>.
- [71] R. G. Ross. Quantifying MLI thermal conduction in cryogenic applications from experimental data. *IOP Conference Series: Materials Science and Engineering*, 101:012017, dec 2015. doi: 10.1088/1757-899x/101/1/012017. URL <https://doi.org/10.1088/1757-899x/101/1/012017>.
- [72] M. Sathyanarayana Rao, M. Silva-Feaver, A. Ali, K. Arnold, P. Ashton, B. J.

Dober, C. J. Duell, S. M. Duff, N. Galitzki, E. Healy, S. Henderson, S.-P. P. Ho, J. Hoh, A. M. Kofman, A. Kusaka, A. T. Lee, A. Mangu, J. Mathewson, P. Mauskopf, H. McCarrick, J. Moore, M. D. Niemack, C. Raum, M. Salatino, T. Sasse, J. Seibert, S. M. Simon, S. Staggs, J. R. Stevens, G. Teply, R. Thornton, J. Ullom, E. M. Vavagiakis, B. Westbrook, Z. Xu, and N. Zhu. Simons Observatory Microwave SQUID Multiplexing Readout: Cryogenic RF Amplifier and Coaxial Chain Design. *JLTP*, 199(3-4):807–816, Mar. 2020. doi: 10.1007/s10909-020-02429-y.

[73] J. T. Sayre, C. L. Reichardt, J. W. Henning, P. A. R. Ade, A. J. Anderson, J. E. Austermann, J. S. Avva, J. A. Beall, A. N. Bender, B. A. Benson, F. Bianchini, L. E. Bleem, J. E. Carlstrom, C. L. Chang, P. Chaubal, H. C. Chiang, R. Citron, C. Corbett Moran, T. M. Crawford, A. T. Crites, T. de Haan, M. A. Dobbs, W. Everett, J. Gallicchio, E. M. George, A. Gilbert, N. Gupta, N. W. Halverson, N. Harrington, G. C. Hilton, G. P. Holder, W. L. Holzapfel, J. D. Hrubes, N. Huang, J. Hubmayr, K. D. Irwin, L. Knox, A. T. Lee, D. Li, A. Lowitz, J. J. McMahon, S. S. Meyer, L. M. Mocuano, J. Montgomery, A. Nadolski, T. Natoli, J. P. Nibarger, G. Noble, V. Novosad, S. Padin, S. Patil, C. Pryke, J. E. Ruhl, B. R. Saliwanchik, K. K. Schaffer, C. Sievers, G. Smecher, A. A. Stark, C. Tucker, K. Vanderlinde, T. Veach, J. D. Vieira, G. Wang, N. Whitehorn, W. L. K. Wu, V. Yefremenko, and SPTpol Collaboration. Measurements of B-mode polarization of the cosmic microwave background from 500 square degrees of SPTpol data. *Phys. Rev. D*, 101(12):122003, June 2020. doi: 10.1103/PhysRevD.101.122003.

[74] G. F. Smoot. Cobe observations and results. *1999AIPC 476*, 476(1):1–10, 1999.

doi: 10.1063/1.59326. URL <https://aip.scitation.org/doi/abs/10.1063/1.59326>.

- [75] K. T. Story, D. Hanson, P. A. R. Ade, K. A. Aird, J. E. Austermann, J. A. Beall, A. N. Bender, B. A. Benson, L. E. Bleem, J. E. Carlstrom, and et al. A measurement of the cosmic microwave background gravitational lensing potential from 100 square degrees of sptpol data. *ApJ*, 810(1):50, Aug 2015. ISSN 1538-4357. doi: 10.1088/0004-637x/810/1/50. URL <http://dx.doi.org/10.1088/0004-637X/810/1/50>.
- [76] R. A. Sunyaev and Y. B. Zeldovich. The Spectrum of Primordial Radiation, its Distortions and their Significance. *Comments on Astrophysics and Space Physics*, 2:66, Mar. 1970.
- [77] R. A. Sunyaev and Y. B. Zeldovich. The Observations of Relic Radiation as a Test of the Nature of X-Ray Radiation from the Clusters of Galaxies. *Comments on Astrophysics and Space Physics*, 4:173, Nov 1972.
- [78] A. Suzuki, P. Ade, Y. Akiba, C. Aleman, K. Arnold, C. Baccigalupi, B. Barch, D. Barron, A. Bender, D. Boettger, and et al. The polarbear-2 and the simons array experiments. *JLTP*, 184(3-4):805–810, Jan 2016. ISSN 1573-7357. doi: 10.1007/s10909-015-1425-4. URL <http://dx.doi.org/10.1007/s10909-015-1425-4>.
- [79] The Simons Observatory Collaboration, S. Aiola, A. Ali, D. Alonso, M. A. Alvarez, K. Arnold, P. Ashton, J. Austermann, H. Awan, C. Baccigalupi, T. Baildon, D. Barron, N. Battaglia, R. Battye, E. Baxter, A. Bazarko, J. A. Beall, R. Bean,

D. Beck, S. Beckman, B. Beringue, F. Bianchini, S. Boada, D. Boettger, J. R. Bond, J. Borrill, M. L. Brown, S. M. Bruno, S. Bryan, E. Calabrese, V. Calafut, P. Calisse, J. Carron, A. Challinor, G. Chesmore, Y. Chinone, J. Chluba, H.-M. S. Cho, S. Choi, G. Coppi, N. F. Cothard, K. Coughlin, D. Crichton, K. D. Crowley, K. T. Crowley, A. Cukierman, J. M. D'Ewart, R. Dünner, T. de Haan, M. Devlin, S. Dicker, J. Didier, M. Dobbs, B. Dober, C. J. Duell, S. Duff, A. Duivenvoorden, J. Dunkley, J. Dusatko, J. Errard, G. Fabbian, S. Feeney, S. Ferraro, P. Fluxà, K. Freese, J. C. Frisch, A. Frolov, G. Fuller, B. Fuzia, N. Galitzki, P. A. Gallardo, J. T. G. Gherzi, J. Gao, E. Gawiser, M. Gerbino, V. Gluscevic, N. Goeckner-Wald, J. Golec, S. Gordon, M. Gralla, D. Green, A. Grigorian, J. Groh, C. Groppi, Y. Guan, J. E. Gudmundsson, D. Han, P. Hargrave, M. Hasegawa, M. Hasselfield, M. Hattori, V. Haynes, M. Hazumi, Y. He, E. Healy, S. W. Henderson, C. Hervias-Caimapo, C. A. Hill, J. C. Hill, G. Hilton, M. Hilton, A. D. Hincks, G. Hinshaw, R. Hlo $\nu$ zek, S. Ho, S.-P. P. Ho, L. Howe, Z. Huang, J. Hubmayr, K. Huffenberger, J. P. Hughes, A. Ijjas, M. Ikape, K. Irwin, A. H. Jaffe, B. Jain, O. Jeong, D. Kaneko, E. D. Karpel, N. Katayama, B. Keating, S. S. Kernasovskiy, R. Kesitalo, T. Kisner, K. Kiuchi, J. Klein, K. Knowles, B. Koopman, A. Kosowsky, N. Krachmalnicoff, S. E. Kuenstner, C.-L. Kuo, A. Kusaka, J. Lashner, A. Lee, E. Lee, D. Leon, J. S.-Y. Leung, A. Lewis, Y. Li, Z. Li, M. Limon, E. Linder, C. Lopez-Caraballo, T. Louis, L. Lowry, M. Lungu, M. Madhavacheril, D. Mak, F. Maldonado, H. Mani, B. Mates, F. Matsuda, L. Maurin, P. Mauskopf, A. May, N. McCallum, C. McKenney, J. McMahan, P. D. Meerburg, J. Meyers, A. Miller, M. Mirmelstein, K. Moodley, M. Munchmeyer, C. Munson, S. Naess, F. Nati, M. Navaroli,

L. Newburgh, H. N. Nguyen, M. Niemack, H. Nishino, J. Orlowski-Scherer, L. Page, B. Partridge, J. Peloton, F. Perrotta, L. Piccirillo, G. Pisano, D. Poletti, R. Puddu, G. Puglisi, C. Raum, C. L. Reichardt, M. Remazeilles, Y. Rephaeli, D. Riechers, F. Rojas, A. Roy, S. Sadeh, Y. Sakurai, M. Salatino, M. S. Rao, E. Schaan, M. Schmittfull, N. Sehgal, J. Seibert, U. Seljak, B. Sherwin, M. Shimon, C. Sierra, J. Sievers, P. Sikhosana, M. Silva-Feaver, S. M. Simon, A. Sinclair, P. Siritanasak, K. Smith, S. R. Smith, D. Spergel, S. T. Staggs, G. Stein, J. R. Stevens, R. Stompor, A. Suzuki, O. Tajima, S. Takakura, G. Teply, D. B. Thomas, B. Thorne, R. Thornton, H. Trac, C. Tsai, C. Tucker, J. Ullom, S. Vagnozzi, A. van Engelen, J. V. Lanen, D. D. V. Winkle, E. M. Vavagiakis, C. Vergès, M. Vissers, K. Wagoner, S. Walker, J. Ward, B. Westbrook, N. Whitehorn, J. Williams, J. Williams, E. J. Wollack, Z. Xu, B. Yu, C. Yu, F. Zago, H. Zhang, and N. Z. and. The simons observatory: science goals and forecasts. *JCAP*, 2019(02):056–056, feb 2019. doi: 10.1088/1475-7516/2019/02/056. URL <https://doi.org/10.1088/1475-7516/2019/02/056>.

[80] R. J. Thornton, P. A. R. Ade, S. Aiola, F. E. Angilè, M. Amiri, J. A. Beall, D. T. Becker, H.-M. Cho, S. K. Choi, P. Corlies, and et al. The atacama cosmology telescope: The polarization-sensitive actpol instrument. *ApJS*, 227(2):21, Dec 2016. ISSN 1538-4365. doi: 10.3847/1538-4365/227/2/21. URL <http://dx.doi.org/10.3847/1538-4365/227/2/21>.

[81] C. E. Tucker and P. A. R. Ade. Thermal filtering for large aperture cryogenic detector arrays. In *SPIE*, volume 6275 of *Society of Photo-Optical Instrumentation Engineers (SPIE) Conference Series*, pages 62750T–1 – 62750T–9, July 2006.



doi: 10.1117/12.673159.

- [82] E. M. Vavagiakis, Z. Ahmed, A. Ali, K. Arnold, J. Austermann, S. M. Bruno, S. K. Choi, J. Connors, N. Cothard, S. Dicker, B. Dober, S. Duff, V. Fanfani, E. Healy, S. Henderson, S.-P. P. Ho, D.-T. Hoang, G. Hilton, J. Hubmayr, N. Krachmalnicoff, Y. Li, J. Mates, H. McCarrick, F. Nati, M. Niemack, M. Silva-Feaver, S. Staggs, J. Stevens, M. Vissers, J. Ullom, K. Wagoner, Z. Xu, and N. Zhu. The simons observatory: Magnetic sensitivity measurements of microwave squid multiplexers. *IEEE Transactions on Applied Superconductivity*, 31(5):1–5, 2021. doi: 10.1109/TASC.2021.3069294.
- [83] A. L. Woodcraft and A. Gray. A low temperature thermal conductivity database. In B. Young, B. Cabrera, and A. Miller, editors, *AIPC*, volume 1185 of *American Institute of Physics Conference Series*, pages 681–684, Dec. 2009. doi: 10.1063/1.3292433.
- [84] W. L. K. Wu, L. M. Mocanu, P. A. R. Ade, A. J. Anderson, J. E. Austermann, J. S. Avva, J. A. Beall, A. N. Bender, B. A. Benson, F. Bianchini, and et al. A measurement of the cosmic microwave background lensing potential and power spectrum from 500 deg<sup>2</sup> of sptpol temperature and polarization data. *ApJ*, 884(1):70, Oct 2019. ISSN 1538-4357. doi: 10.3847/1538-4357/ab4186. URL <http://dx.doi.org/10.3847/1538-4357/ab4186>.
- [85] Z. Xu, T. Bhandarkar, G. Coppi, A. Kofman, J. L. Orłowski-Scherer, N. Zhu, A. M. Ali, K. Arnold, J. E. Austermann, S. K. Choi, J. Connors, N. F. Cothard, M. Devlin, S. Dicker, B. Dober, S. M. Duff, G. Fabbian, N. Galitzki, S. Haridas,

- K. Harrington, E. Healy, S.-P. P. Ho, J. Hubmayr, J. Iuliano, J. Lashner, Y. Li, M. Limon, B. J. Koopman, H. McCarrick, J. Moore, F. Nati, M. D. Niemack, C. L. Reichardt, K. Sarmiento, J. Seibert, M. Silva-Feaver, R. F. Sonka, S. Staggs, R. J. Thornton, E. M. Vavagiakis, M. R. Vissers, S. Walker, Y. Wang, E. J. Wollack, and K. Zheng. The Simons Observatory: the Large Aperture Telescope Receiver (LATR) integration and validation results. In J. Zmuidzinas and J.-R. Gao, editors, *2021SPIE11453*, volume 11453, pages 207 – 226. International Society for Optics and Photonics, SPIE, 2020. doi: 10.1117/12.2576151. URL <https://doi.org/10.1117/12.2576151>.
- [86] Z. Xu, M. K. Brewer, P. F. Rojas, Y. Li, K. Osumi, B. Pradenas, A. Ali, J. W. Appel, C. L. Bennett, R. Bustos, M. Chan, D. T. Chuss, J. Cleary, J. D. Couto, S. Dahal, R. Datta, K. L. Denis, R. Dünner, J. R. Eimer, T. Essinger-Hileman, D. Gothe, K. Harrington, J. Iuliano, J. Karakla, T. A. Marriage, N. J. Miller, C. Núñez, I. L. Padilla, L. Parker, M. A. Petroff, R. Reeves, K. Rostem, D. A. Nunes Valle, D. J. Watts, J. L. Weiland, E. J. Wollack, and CLASS Collaboration. Two-year Cosmology Large Angular Scale Surveyor (CLASS) Observations: 40 GHz Telescope Pointing, Beam Profile, Window Function, and Polarization Performance. *ApJ*, 891(2):134, Mar. 2020. doi: 10.3847/1538-4357/ab76c2.
- [87] Z. Xu, G. E. Chesmore, S. Adachi, A. M. Ali, A. Bazarko, G. Coppi, M. Devlin, T. Devlin, S. R. Dicker, P. A. Gallardo, J. E. Golec, J. E. Gudmundsson, K. Harrington, M. Hattori, A. Kofman, K. Kiuchi, A. Kusaka, M. Limon, F. Matsuda, J. McMahon, F. Nati, M. D. Niemack, A. Suzuki, G. P. Teply, R. J. Thornton, E. J. Wollack, M. Zannoni, and N. Zhu. The simons observatory:

- metamaterial microwave absorber and its cryogenic applications. *ApOpt*, 60(4):864–874, Feb 2021. doi: 10.1364/AO.411711. URL <http://ao.osa.org/abstract.cfm?URI=ao-60-4-864>.
- [88] B. Yu, J. C. Hill, and B. D. Sherwin. Multitracer cmb delensing maps from planck and wise data. *Phys. Rev. D*, 96:123511, Dec 2017. doi: 10.1103/PhysRevD.96.123511. URL <https://link.aps.org/doi/10.1103/PhysRevD.96.123511>.
- [89] N. Zhu, T. Bhandarkar, G. Coppi, A. M. Kofman, J. L. Orlowski-Scherer, Z. Xu, S. Adachi, P. Ade, S. Aiola, J. Austermann, A. O. Bazarko, J. A. Beall, S. Bhimani, J. R. Bond, G. E. Chesmore, S. K. Choi, J. Connors, N. F. Cothard, M. Devlin, S. Dicker, B. Dober, C. J. Duell, S. M. Duff, R. Dünner, G. Fabbian, N. Galitzki, P. A. Gallardo, J. E. Golec, S. K. Haridas, K. Harrington, E. Healy, S.-P. P. Ho, Z. B. Huber, J. Hubmayr, J. Iuliano, B. R. Johnson, B. Keating, K. Kiuchi, B. J. Koopman, J. Lashner, A. T. Lee, Y. Li, M. Limon, M. Link, T. J. Lucas, H. McCarrick, J. Moore, F. Nati, L. B. Newburgh, M. D. Niemack, E. Pierpaoli, M. J. Randall, K. P. Sarmiento, L. J. Saunders, J. Seibert, C. Sierra, R. Sonka, J. Spisak, S. Sutariya, O. Tajima, G. P. Teply, R. J. Thornton, T. Tsan, C. Tucker, J. Ullom, E. M. Vavagiakis, M. R. Vissers, S. Walker, B. Westbrook, E. J. Wollack, and M. Zannoni. The simons observatory large aperture telescope receiver. *The Astrophysical Journal Supplement Series*, 256(1):23, sep 2021. doi: 10.3847/1538-4365/ac0db7. URL <https://doi.org/10.3847/1538-4365/ac0db7>.